

Copyright
by
Murat Yildirim
2015

**The Dissertation Committee for Murat Yildirim Certifies that this is the approved
version of the following dissertation:**

**Nonlinear Imaging Assisted Ultrafast Laser Microsurgery for the
Treatment of Vocal Fold Scarring**

Committee:

Adela Ben-Yakar, Supervisor

Jayathi Murthy

Matthew Hall

James Tunnell

James Kobler

**Nonlinear Imaging Assisted Ultrafast Laser Microsurgery for the
Treatment of Vocal Fold Scarring**

by

Murat Yildirim, B.S.; M.S.

Dissertation

Presented to the Faculty of the Graduate School of
The University of Texas at Austin
in Partial Fulfillment
of the Requirements
for the Degree of

Doctor of Philosophy

The University of Texas at Austin

August 2015

Dedication

This dissertation is dedicated to my father and my mother – for their inexhaustible support, patience, love, and understanding that help me get this far.

Acknowledgements

I would like to thank the many people who helped me in completing this work. Particularly, I would like to thank Dr. Adela Ben-Yakar for introducing me to the field of biomedical optics and for providing support, motivation, and inspiration throughout the course of my research. Additionally, I would like to thank my lab-mates particularly Dr. Onur Ferhanoglu for his generous help and support for performing table-top and endoscope experiments, Dr. Christopher Hoy for introducing me to the vocal fold studies, Dr. Nicholas Durr for his help in developing Monte-Carlo modeling, Dr. Navid Ghorashian and Sertan Kutal Gokce for their discussion on developing semi-automated biomaterial injection system, Kaushik Subramanian for his help on coupling ultra-short pulses to photonic bandgap fibers. The friendship made in this lab and throughout the graduate program will remain invaluable to me.

I also would like to acknowledge our collaborators, in particular: Drs. James Kobler, Steven Zeitels, and Sandeep Karajanagi at Massachusetts General Hospital for providing hamster cheek pouch samples, and PEG 30 biomaterial; Drs. Kyle Quinn, and Irene Georgakoudi at Tufts University for providing numerical modeling for collagen fiber directionality.

I also would like to acknowledge fund resource agencies such as National Science Foundation and Cancer Prevention and Research Institute of Texas that have made my research happen so far.

Nonlinear Imaging Assisted Ultrafast Laser Microsurgery for the Treatment of Vocal Fold Scarring

Murat Yildirim, Ph.D.

The University of Texas at Austin, 2015

Supervisor: Adela Ben-Yakar

Femtosecond laser pulses achieve unrivaled microsurgical precision by developing extremely high peak intensity with relatively low total pulse energy. Despite a wide range of clinical advantages and applications that have been identified in bench-top studies, clinical development of femtosecond laser microsurgery outside of ophthalmology has remained in its infancy. The lack of a means to flexibly deliver the high-intensity laser light to areas of interest and guide it with suitable precision has constituted a serious hurdle to further clinical development. In response, this dissertation has detailed my research and development of table-top systems and the fiber-coupled femtosecond laser microsurgery scalpel to treat vocal fold scarring which does not have any reliable treatment in the clinic.

This dissertation focuses on laser ablation and nonlinear imaging parameters for creation of sub-epithelial voids in vocal folds and how these parameters varied in scar tissue using animal models. We specifically investigated the differences in tissue architecture and scattering properties, and their relation to ablation thresholds and bubble lifetime. By using nonlinear imaging, we quantified tissue architecture and bubble dynamics. By developing a new method, we measured the ablation threshold below tissue surface while simultaneously extracting the extinction properties of different tissue

layers. Also, we performed in-depth analysis using numerical, analytical, and experimental techniques to understand the limitation of maximum imaging depths with third-harmonic generation microscopy in turbid tissues such as vocal folds compared to two-photon autofluorescence microscopies. Our experimental results revealed that maximum imaging depth improved significantly from 140 μm to 420 μm using THG microscopy at 1552 nm excitation wavelength as compared to TPM at 776 nm.

The second part of the dissertation explores developing a novel biomaterial-delivery method to inject and localize PEG 30 biomaterial inside sub-epithelial voids created by ultra-short laser pulses within scarred cheek pouch samples. To demonstrate the feasibility of this technique, we developed a semi-automated system to control and monitor the diffusion of the biomaterial inside scarred hamster cheek pouch samples. We observed a back-flow of the injected biomaterial along the point of injection and this condition prevented localization of the biomaterial at the desired locations without creating any void. In contrast to the biomaterial injection outcomes without any voids, the presence of sub-epithelial voids greatly reduced back-flow at the injection site and resulted in a lasting localization of the injected biomaterial at different locations of the tissue. We also performed a follow-up H&E histology and realized that the location and appearance of the biomaterial correlated well with TPAF and SHG in-situ nonlinear images.

Finally, in the third part of the dissertation, we developed a piezo-scanned fiber device for high-speed ultrafast laser microsurgery, with an overall diameter of 5 mm. While the diameter of the scalpel is now half of our latest probe, its resolution has been also improved by 10% in both lateral and axial directions. The use of a high repetition rate fiber laser, delivering 300,000 pulses per second, and utilizing a sub-frame rate Lissajous scanning approach provided high ablation speeds suitable for clinical use. As

shown by the uniform ablation of gold samples, an ablation FOV of $150\text{ }\mu\text{m} \times 150\text{ }\mu\text{m}$ could be achieved within only 50 ms. With such ablation speeds, drilling into a cheek pouch tissue was possible using pulse energies of 200 nJ (3.2 J/cm^2). With these speeds the surgeon could potentially move the surgery probe at speeds near 4 mm/s laterally in one direction while continuously removing a $150\text{ }\mu\text{m}$ wide tissue layer.

Table of Contents

List of Tables	xii
List of Figures	xiii
Chapter 1: Introduction	1
Chapter 2: Background	3
2.1: Vocal fold scarring.....	3
2.2: Ultrafast Laser Microsurgery	5
2.3: Nonlinear Optical Imaging	8
2.4: Recent Developments Towards Endoscopic Ultrafast Laser Surgery ...	10
2.5: Clinical Motivation: Medicine at the Microscale	14
Chapter 3: Parameters Affecting Ultrafast Laser Microsurgery of Sub-Epithelial Voids for Scar Treatment in Vocal Folds	18
3.1: Introduction.....	18
3.2: Methods and Materials.....	22
3.2.1: Experimental Setup.....	22
3.2.2: Ex Vivo Tissue Samples	25
3.2.2.1: Fresh Porcine Vocal Folds	25
3.2.2.2: Hamster Cheek Pouch Mucosa as a Scar Model	26
3.3: Results.....	27
3.3.1: Imaging of Tissue Architecture	27
3.3.2: Ablation Studies.....	33
3.3.2.1: Ablation versus Pulse Energy	33
3.3.2.2: Sample-to-Sample Repeatability of Tissue Ablation	36
3.3.2.3: Ablation Threshold and Tissue Scattering Properties....	38
3.3.2.4: Bubble Dynamics in Ablated Voids	43
3.4: Discussion and Conclusions	46
3.4.1: Mechanical Properties of Tissue.....	47
3.4.2: The Effect of Mechanical Properties of Tissue on Bubble Dynamics	48

3.4.3: The Effect of Mechanical Properties and Impurities on Ablation Threshold	49
Chapter 4: Tripling the Maximum Imaging Depth with Third-Harmonic Generation Microscopy	52
4.1: Introduction.....	52
4.2: Methods and Materials.....	56
4.2.1: Experimental Setup.....	56
4.2.2: Ex Vivo Tissue Preparation	59
4.3: Results.....	59
4.3.1: Extinction Properties of Tissue.....	58
4.3.2: Maximum Imaging Depth.....	61
4.3.3: Analytical and Monte-Carlo Modeling of Maximum Imaging Depths	64
4.3.4: Tissue Heating Properties during THG Imaging	67
4.4: Discussion.....	72
4.5: Conclusion	75
Chapter 5: Quantitative Differentiation of Normal and Scarred Tissues using Second Harmonic Generation Microscopy for the Treatment of Vocal Fold Scarring..	77
5.1: Introduction.....	77
5.2: Materials and Methods.....	80
5.2.1: Experimental Setup.....	80
5.2.2: Automated SHG Image Analysis Technique.....	81
5.2.3: Animal Model	83
5.2.4: Statistical Analysis.....	84
5.3: Results.....	84
5.4: Discussion.....	87
5.5: Conclusion	89
Chapter 6: Biogel Injection in Scar Tissue Enabled by Ultrafast Laser Ablation for the Treatment of Vocal Fold Scarring..	90
6.1: Introduction.....	90

6.2: Materials and Methods.....	93
6.2.1: Experimental Setup.....	93
6.2.2: Animal Model.....	96
6.3: Results.....	97
6.4: Discussion.....	102
6.5: Conclusion.....	103
Chapter 7: A 5-mm Piezo Scanning Fiber Device for High-Speed Ultrafast Laser Microsurgery.....	105
7.1: Introduction.....	105
7.2: Results.....	107
7.2.1: Device Design and Characterization.....	107
7.2.2: Study of Maximum Pulse Energy Delivery Through the Air-Core Photonic Bandgap Fiber.....	112
7.2.3: High Speed Ablation by Resonant Scanning.....	120
7.3: Discussion.....	125
7.4: Conclusions.....	127
Chapter 8: Conclusion.....	129
References.....	135
Vita	149

List of Tables

Table 3.1: Summary of tissue optical and mechanical properties and ablation thresholds	41
Table 4.1: Summary of measured optical properties at 776 and 1552 nm excitation wavelengths	61
Table 4.2: Tissue thermal relaxation times for exposure to different average powers.....	69

List of Figures

Figure 2.1: Three generations of endoscopic ultrafast laser surgery probes..	12
Figure 3.1: Schematic of the two-channel , bench-top microscope for combined nonlinear imaging and microsurgery	23
Figure 3.2: Overlaid TPAF (red) and SHG (green) images of fresh superior porcine vocal fold	28
Figure 3.3: Overlaid TPAF (red) and SHG (green) images of fresh inferior porcine vocal fold	29
Figure 3.4: Histology images of porcine vocal folds and hamster cheek pouches	30
Figure 3.5: Representative SHG images of control hamster cheek pouch samples	31
Figure 3.6: Representative SHG images of scarred hamster cheek pouch samples	32
Figure 3.7: Comparison of cross-sectional TPAF images with histological analysis of voids in an inferior porcine vocal fold.....	34
Figure 3.8: The effect of incident laser pulse energy on the subsurface ablation properties of porcine vocal folds.	35
Figure 3.9: The effect of incident laser pulse energy on the subsurface ablation properties of hamster cheek pouches.....	36
Figure 3.10: Normalized area of the initial bubbles in the ablated voids at different incident pulse energies one minute after ablation.	37

Figure 3.11: Minimum pulse energy at the surface to initiate ablation at different depths and the resultant maximum ablation depth dependence on pulse energy.....	43
Figure 3.12: Time-lapse side view TPAF images of a bubble in a sub-epithelial void that was created with 750 nJ pulse energy in inferior vocal fold.	44
Figure 3.13: Bubble lifetimes for different pulse energies for 2 different samples for each tissue.....	45
Figure 4.1: Schematic of the inverted microscope system for nonlinear imaging and ablation.	58
Figure 4.2: Representative nonlinear optical images of a fresh superior porcine vocal fold.	64
Figure 4.3: Signal to background ratio (SBR) values for both nonlinear imaging modalities.....	64
Figure 4.4: Analytical and numerical modeling of maximum imaging depth..	67
Figure 4.5: Tissue surface temperature measurement using an IR camera	71
Figure 4.6: Dynamics of tissue temperature during typical THG imaging conditions.....	72
Figure 5.1: Schematic of the upright microscope system for nonlinear imaging.	81
Figure 5.2: Representative SHG images, collagen fiber direction histograms, and collagen fiber density plots for a control and a scarred hamster cheek pouch.	85
Figure 5.3: Representative depth-resolved collagen fiber direction for a control and a scarred hamster cheek pouch.	86

Figure 5.4: Collagen fiber directional variance and fiber density for 5 different regions of 4 samples.....	86
Figure 6.1: Schematic of the upright microscope system for nonlinear imaging.	94
Figure 6.2: Experimental setup for control and monitor of biomaterial injection into a scarred cheek pouch..	95
Figure 6.3: Dispensed volume of the biomaterial with respect to the its exposure time at different air pressure values.....	99
Figure 6.4: Representative fluorescence images before and after the biomaterial injection.....	99
Figure 6.5: Representative fluorescence images after the biomaterial injection into different sizes of sub-epithelial voids.	100
Figure 6.6: Representative fluorescence and nonlinear microscopy images before and after injection of the biomaterial into a sub-epithelial void.	100
Figure 6.7: Histological follow-up of PEG 30 biomaterial into a sub-epithelial void.	101
Figure 7.1: Optical architecture and resolution of the scalpel.	109
Figure 7.2: Effect of coupling NA, coupling misalignments, and beam pointing instabilities on delivered energy thorough the 7- μ m, air-core PBF...116	
Figure 7.3: Ablation patterns at various laser exposure durations.	122
Figure 7.4: Ablation of tissue surface using the 5-mm laser scalpel.....	123
Figure 7.5: Effect of translation speed on ablation coverage.	126

Chapter 1: Introduction

The barriers to clinical acceptance of ultrafast laser surgery are lower in applications that leverage the unique ability of ultrafast lasers to create precise cuts inside bulk tissue due to the lack of competing technologies. Similarly, the barriers to clinical acceptance are also lower in applications for which there is no accepted treatment with conventional methods. For these reasons, we have been developing a technique for treating scarred vocal folds wherein focused ultrafast laser pulses create a sub-epithelial space in scarred tissue, which enables localization of injected biomaterials to restore the desired mechanical properties.

Vocal fold scarring is a common side effect of surgical treatment of laryngeal cancer and can also result from disease or prolonged mechanical stress. The presence of scar tissue in the vocal folds increases their stiffness, thus degrading or even eliminating voice function (phonation). Current treatment options are very limited. A variety of injected biomaterials have been suggested for restoring the viscoelasticity of the vocal folds. However optimal localization of the material within the scarred tissue is likely to be extremely difficult and unpredictable with injection alone because the injected material tends to follow the path of least resistance, ending up where it is least needed. To address this challenge, we have proposed a treatment in which an injection space is created through sub-epithelial ablation of a planar region in the vocal fold.

The following chapters will first review the underlying mechanisms behind both microsurgery and nonlinear microscopy with femtosecond laser pulses, as well as their clinical applications and current state of development. Next, we will explore the parameters affecting ultrafast laser microsurgery and nonlinear imaging of sub-epithelial voids. With the insight gained from these parameters, we will then cover the in-depth

improvement in maximum imaging depth utilizing longer excitation wavelength and three-photon processes such as third-harmonic generation microscopy. Then, we will demonstrate quantitative differentiation of normal and scarred hamster cheek pouch samples through determining collagen fiber direction and density by developing an automated second-harmonic generation image analysis technique. Next, we will demonstrate developing a semi-automated system for localization of a polyethylene glycol (PEG) based biomaterial stained with Rhodamine dye into the ablated sub-epithelial void of scarred cheek pouch samples. Lastly, the dissertation will summarize recent work in developing an ultrafast laser scalpel that can improve microsurgery speed with a 5-mm diameter size.

Chapter 2: Background

2.1: VOCAL FOLD SCARRING

There have been significant developments in phonosurgery, the surgical treatment of vocal fold pathology, but vocal fold scarring remains a therapeutic challenge [1]. Chronic voice impairment due to vocal fold scarring is estimated to affect ~ 4 million people in the US alone [2]. However, there is no reliable treatment for restoring proper phonation to individuals with scarred vocal folds. The use of injectable materials to restore pliability of the superficial lamina propria (LP) is a strategy that has shown promise in pre-clinical studies [3-7]. Ongoing development of such materials is a significant research focus in the field of phonosurgery. A widespread problem facing the surgical use of injectable materials is their inaccurate and ineffective placement in a superficial plane in scarred vocal folds. Vocal fold scarring, resulting from disease, mechanical stress from overuse, or post-surgical healing, reduces the mechanical compliance of the vocal fold tissue and is a major cause of voice disorders. It is estimated that ~ 4 million people in the U.S. alone suffer from chronic voice impairment due to vocal fold scarring [2]. Unfortunately, no reliable treatment currently exists for restoring proper phonation in scarred vocal folds. One treatment method that has shown promise utilizes the injection of soft biomaterials aimed at restoring the proper viscoelasticity to the tissue [1, 6, 7]. In scarred vocal fold tissue, the density of the tissue and the required injection pressure are likely to impair the proper localization of the injected material in the desired tissue layer, and reduce effectiveness of the injection treatment. To enhance the ability of surgeons to place injectables into scarred tissue with precision, we proposed a new technique to ablate sub-epithelial planar voids in vocal folds using ultra-short laser pulses.

Contemporary understanding of the microanatomy of the human vocal fold [8] reveals a layered structure that consists of epithelium as the outermost layer followed by the LP and the vocalis muscle. The LP can be subdivided into superficial, intermediate, and deep lamina sub-layers based on distribution of extracellular matrix (ECM) fibrous proteins such as collagen and elastin. Collagen and elastin fibers are largely responsible for providing the strength and elasticity of the vocal folds. The superficial lamina propria (SLP) has a thin sheet of collagen fibers that are highly aligned along the length of the vocal fold [9]. Below these fibers, the SLP mainly consists of amorphous ground substance (primarily, proteoglycans and glycosaminoglycans) with scattered elastin and collagen fibers, fibroblasts, and other elements typical of loose connective tissue [10]. During the wound healing response, scar tissue can replace the SLP along with deeper parts of the LP. The scar tissue predominantly consists of collagen and fibronectin, both of which increase the stiffness of the mucosa and can lead to severe impairment in voice production, or dysphonia [1].

According to our collaborator Dr. Zeitels and his colleagues [11, 12], injection of soft biomaterials in the sub-epithelial region of scarred vocal fold tissue is likely to be challenging due to presence of dense scar tissue. Such dense tissue requires high injection pressures and limits precision since injections tend to take a path of least resistance. We propose to overcome this challenge by creating a planar ablation void that is essentially a thin sub-epithelial plane of separation that injected substances could easily dissect into, forming a mattress-like layer similar to normal SLP regardless of scar tissue inhomogeneities [13]. The ablation plane would ideally encompass the scarred phonatory area, which could extend over an area as large as $3 \times 10 \text{ mm}^2$ in a heavily scarred vocal fold. We hypothesize that such void will reduce the required injection pressure and

improve the superficial localization of an injected biomaterial for restoration of a phonatory mucosal wave.

2.2: ULTRAFAST LASER MICROSURGERY

Almost since their inception, lasers have been put to use as versatile biological cutting tools. The invention of the laser in 1960 intrigued biologist and clinicians alike with the prospect of a surgical tool capable of creating targeted damage with diffraction-limited precision [14, 15]. Quickly thereafter, a variety of laser surgery applications were developed, ranging in scale from sub-cellular dissection of organelles [16-18] and chromosomes [19] to bulk tissue ablation of eyes [20], skin [21], and teeth [22]. Over the next fifty years, the surgical applications of lasers grew and matured, leading to an abundance of discoveries in cell biology [23] and clinical applications throughout medicine where acceptance has been particularly strong in ophthalmology [24], dermatology [25], and otolaryngology [26].

The development of clinical laser techniques has centered on continuous wave (cw) and nanosecond or longer pulsed lasers. These conventional laser surgery techniques rely predominantly on linear absorption of laser light because the laser intensities are generally too low to induce appreciable nonlinear interaction at practical average powers. Owing to the linear absorption mechanism, photodamage from these lasers is highly wavelength-dependent and thermal in nature [27]. This wavelength dependence can be exploited to create a tissue-selective effect. However, it can also result in non-deterministic cutting effects when cutting heterogeneous tissue and can limit efficacy in transparent or low-absorbing samples. Similarly, though laser heating has been used to great effect clinically for both cauterization of laser incisions and tissue welding [28], the diffusion of heat away from the laser focal volume can lead to collateral damage outside

the focal volume and may lead to scarring in biological tissues. While both wavelength-dependence and heating can be mitigated or exploited, the linear absorption of laser light throughout the laser-tissue interaction volume leads to increased damage outside the focal volume along the laser path. This lack of axial confinement ultimately limits their precision inside thicker specimens. With the development of ultrafast-pulsed laser sources in the early 1980s, which deliver pulse durations in the range of 100 fs to 10 ps, biologists and clinicians were given access to new predominantly non-thermal regimes of photodamage, which have increased surgical precision to the diffraction limit and beyond.

Focused ultrafast laser pulses are uniquely suited for creating sub-surface voids. Having short pulse durations and thus high peak intensities, ultrafast lasers ensure the use of minimal energies for high precision ablation with minimal damage to surrounding tissue. Ablation of a dielectric material, such as tissues, with ultrafast laser pulses begins with generation of free electrons through combination of multi-photon ionization and band-gap (Zener) tunneling [29, 30]. The quasi-free electrons may then act as seed electrons for avalanche ionization. During avalanche, quasi-free electrons accelerate by gaining kinetic energy from the incident laser field. Accelerated free electrons collide with bound valence electrons and ionize them through impact ionization. This exponential multiplication process repeats and cascades until the termination of the laser pulse. The final value of the free electron density determines the photo-damage mechanism, which can be photochemical, induced by thermo-elastic stress confinement, or a result of optical breakdown when a critical electron density is reached [31, 32]. In the thermo-elastic stress confinement, thermalization of the plasma occurs faster than the acoustic relaxation time [30]. The confinement of thermal stresses can overcome tensile strength of tissue and lead to its tearing. Similarly, tissue fracturing/tearing may occur in

the optical breakdown regime due to the shock wave formation as the strength of the pressure increase across the shock wave exceed tissue tensile strength [27].

In addition to mechanical effects, the mechanism for the free electron generation determines the ablation threshold that depends on the laser pulse duration, initial seed electrons, and the linear absorption of tissue. The multi-photon ionization dominates the free electron generation for pulse width < 100 fs [33]. At longer pulse durations in the range of 500 fs -10 ps, the contribution of cascade ionization to the formation of free electrons increases by at least 3-4 orders of magnitude, however, with no drastic change in the ablation threshold and the thermo-mechanical effects [34]. Lower threshold fluence can be observed in the presence of initial seed electrons in the focal volume due to impurities. However, this effect is only noticeable for pulse widths > 10 ps [35]. As for the effect of linear absorption, a 2-3 fold decrease in the ablation threshold can be observed if tissue absorption coefficient is increased by 3 orders of magnitude from 0.1 cm^{-1} to 22 cm^{-1} [36].

Ultrafast laser microsurgery has been demonstrated in a number of applications, including cell optoporation for drug delivery and transfection [33, 37, 38], subcellular dissection [39, 40], nanoaxotomy [32, 41, 42], intracerebral hemorrhage [43], and both hard and soft tissue ablation [43-45]. Recently, ULMS has begun to transition from the research laboratory to the operating room, primarily in ophthalmology where femtosecond laser systems produced by IntraLase Crop. have been employed for LASIK surgery since 2003 [46]. To fully realize the precision of ULMS in many clinical applications, however, it must be capable of being flexibly delivered to various locations of the body and must be guided and monitored by an equally precise and penetrating 3D imaging technique, such as TPAF and SHG microscopy [47-50]. Though several studies have demonstrated combined ULMS and NOI in laboratory settings, these studies were

conducted using two ultrafast lasers in a large table-top microscope which would be unsuitable for treatment of many clinical pathologies [51-53]. Successful laser microsurgery of healthy and scarred tissue samples with nonlinear imaging assistance through a single, compact fiber laser has been previously demonstrated, showing the potential for sub-surface ablation confined within the sub-layers of the LP by our group [13, 54]. For many such applications, ultrafast lasers must be flexibly delivered to the target tissue via a flexible optical fiber. Fiber optic delivery of amplified ultra-short pulses is a significant technical obstacle due to the onset of self-phase modulation (SPM), group-velocity dispersion (GVD), and material damage in traditional single core fibers, which temporally and spectrally distort the laser pulses [55, 56]. Recent developments in air-core photonic crystal fibers promise to overcome these limitations [57-59]. We have recently demonstrated photonic crystal fiber-based miniaturized probes for delivering ultrafast laser pulses for microsurgery and nonlinear imaging [60, 61].

2.3: NONLINEAR OPTICAL IMAGING

Here, nonlinear optical imaging is used to refer to the imaging techniques of multi-photon microscopy such as two- and three-photon microscopies, and multi-harmonic generation microscopy such as second- and third- harmonic generation microscopies. Two-photon microscopy is a form of laser scanning fluorescence microscopy capable of imaging within biological tissue to depths in excess of 1 mm [62, 63]. In laser scanning fluorescence microscopy, a focused laser spot is scanned in a sample to excite fluorescence and the detected emission is reconstructed to create an image of the sample. In two-photon microscopy, ultra-short laser pulses are used to excite fluorophores by near-simultaneous absorption of two photons. Because two-photon absorption uses two photons of lower energy to overcome the bandgap in a fluorophore,

wavelengths in the NIR can be used to excite many commonly used fluorophores. Just as in ULMS, the use for NIR wavelength provides two-photon microscopy with depth penetration superior to that of single-photon fluorescence techniques. Furthermore, because two-photon absorption depends quadratically on the incident light intensity, the excitation is three-dimensionally confined to the focal volume, similar to the confinement of damage in ULMS. In two-photon microscopy, this confinement provides inherent optical sectioning for high-resolution three-dimensional imaging and greatly reduces out-of-focus photobleaching and photochemical damage.

Two-photon microscopy systems can also be used to image second harmonic generation (SHG), another nonlinear two-photon interaction process [50, 64]. In SHG, two photons of a given wavelength interact with a nonlinear material to create one new photon at half the original wavelength. This process is analogous to the creation of a single fluorescent emission photon from two-photon absorption, however SHG is polarization dependent and the resulting signal is anisotropically emitted in the forward direction. Nevertheless, the backscattered SHG signal can be detected to create images of biological structures such as collagen fibers and other types of connective tissue. Images of SHG can provide information about morphology in the extracellular matrix, where there are fewer endogenous fluorophores, which makes SHG imaging a good complement to two-photon microscopy. In practice, SHG microscopy is often performed concurrently with two-photon microscopy and many systems do not distinguish between the two signals.

Both two-photon and second-harmonic microscopies can provide valuable diagnostic information when used to image biological tissue, and commercial clinical two-photon microscopies have become available from JenLab GmbH (Jena, Germany). In addition to morphological information, excitation of endogenous fluorophores

(autofluorescence) can be used to visualize other diagnostic indicators, such as the metabolic rate [65]. Specifically, two-photon microscopy can be a powerful tool for early cancer diagnostics and staging by imaging cellular autofluorescence and observing changes in morphology and signal intensity [65-69]. Furthermore, the use of molecularly-specific targeted contrast agents can provide a host of potential disease indicators that can be imaged with two-photon microscopy [70, 71]. The use of contrast agents has also been used to provide other types of functional information, such as neural activity in the brain [72, 73], as well as anatomical information, such as the vascular pathways [74-76], which enable a wide range of diagnostic applications.

2.4: RECENT DEVELOPMENTS TOWARDS ENDOSCOPIC ULTRAFAST LASER SURGERY

In nonlinear optical imaging, miniaturization efforts have focused primarily on developing two-photon microscopy devices and TPM probes have been developed since 2001 [77]. Since the mechanics of TPM systems are in most cases identical to those used in SHG and TPL microscopy, the design considerations for miniature TPM probes are approximately the same considerations that will be encountered in developing a device for SHG and TPL microscopy as well. Thus far, the primary impetus for development has been neurological research [78-82], though recently probes have been developed toward clinical examination [83-88].

Many clinical applications require flexible delivery of the surgical laser pulses to the clinical region of interest using fiber optics. While fiber optics delivery is common practice for many conventional cw and long pulse lasers, fiber propagation poses several challenges for ultra-short pulses. The first challenge is that of group velocity dispersion (GVD). GVD occurs when the velocity of light exhibits a dependence on the wavelength of the light, causing the different spectral components in a single laser pulses to travel at

different speeds. Shorter laser pulses necessarily contain greater spectral bandwidth so that, when all spectral components are in phase, interference among the spectral components leads to a short pulse in the time domain. The relatively large spectral bandwidth of ultra-short pulses makes them susceptible to GVD, which arises primarily from either material dispersion or waveguide dispersion. First-order linear dispersion can commonly be compensated for through the use of either prism pair or grating pair to introduce GVD of an opposite direction, in what is known as pulse chirping.

Through the optical Kerr effect, the speed of light can also depend on the instantaneous pulse intensity for high peak power laser pulses. In this case, the change in the local speed of light during the propagation of the pulse can create a phase shift across the pulse. This phenomenon is referred to as self-phase modulation (SPM). Because a new spectral bandwidth is being created during SPM, the onset of SPM alongside GVD can result in accelerated pulse broadening in media with normal dispersion until the peak power is no longer sufficient for SPM. In this manner, SPM can lead to nonlinear dispersion properties, particularly in conventional optical fibers where GVD is nearly always present and high peak powers arise due to spatial confinement. This nonlinearity of the dispersion makes pre-compensation with a pulse chirping system extremely difficult and thus SPM must be avoided in delivering high peak power ultra-short laser pulses through normally dispersive media for microsurgery.

In the absence of SPM, such as during propagation through air-core photonic bandgap fibers, waveguide dispersion can be compensated for and ultrafast pulses capable of initiating optical breakdown in cells and tissues can be delivered [60]. In this case, the limit to the maximum deliverable peak power becomes the damage threshold of the optical fiber during coupling. This limitation can be addressed by using fibers with a larger air core or by increasing the pulse-chirping prior to the fiber to reduce the peak

intensity during coupling while appropriately increasing the fiber length to restore the ultrafast pulse duration at the sample.

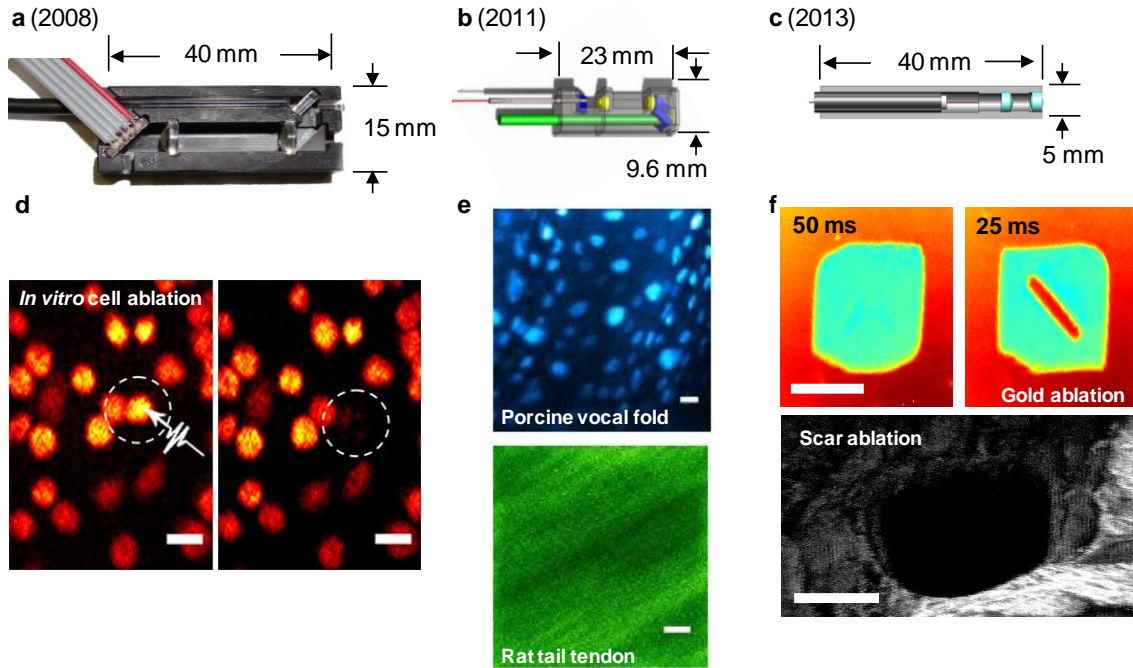


Figure 2.1. Three generations of endoscopic ultrafast laser surgery probes. Photograph of the **a** 18-mm probe [60] and schematics of the **b** 9.6-mm probe [61] and the **c** 5-mm probe [89]. **d** Two-photon image of a single layer of live breast carcinoma cells after uptake of calcein AM taken prior to irradiation with high intensity pulses (left) and the same immediately after irradiation with a single pulse at 280 nJ pulse energy (right) using the 18-mm probe. Scale bars are 20 μm . **e** (Top) A maximum intensity projection of a ~ 70 μm thick two-photon fluorescence image stack of freshly excised porcine vocal fold, stained with Hoechst 3342, showing nuclear details, acquired with the 9.6-mm probe. (Bottom) A SHG image of excised rat tail tendon, showing highly aligned collagen fibers. Scale bars are 10 μm and 5 μm , respectively. **f** Ablation of a 30-nm gold coated glass slide using the 5-mm probe, scanned for 50 ms (left) and 25 ms (right) durations in a Lissajous pattern. The entire gold within the FOV is successfully ablated at durations of 50 ms and above. Ultrafast laser drilling through an *ex vivo* 70- μm thick scarred hamster cheek pouch using 200 nJ pulse energy (bottom); an *xy* maximum intensity projection acquired using a benchtop nonlinear microscope visualizing SHG following ablation. Scale bars are 100 μm .

Our group has been developing fiber-coupled ultrafast laser surgery probes. The first probe, shown in Fig.2.1a, consisted of a 1-m air-core photonic bandgap fiber for

delivery of amplified and unamplified femtosecond laser pulses, a microelectromechanical system (MEMS) scanning mirror, a micro-optical system of aspheric and gradient index (GRIN) lenses for beam delivery and focusing. This probe also incorporated a large-core, high-NA fiber for collection of emitted photons from multiphoton fluorescence and SHG, thus enabling the use of low-energy high-repetition rate laser pulses for surgical guidance by nonlinear microscopy [60]. With this first probe, precise image-guided cellular surgery was demonstrated by imaging fluorescently labeled breast carcinoma cells in cell cultures and scattering phantoms and then by ablating selected single cells, shown in Fig 2.1d. While this probe demonstrated the potential for image-guided ultrafast laser surgery in a fiber-coupled probe, the dimensions of this probe would require an 18 mm diameter delivery channel, which precluded endoscopic delivery.

A second probe was developed based on the same architecture which reduced the probe size to less than 10 mm in diameter [26], as seen in Fig.2.1b. Compared to the first probe, the second probe improved the lateral and axial resolution by 20% and 40% to 1.27 μm and 13.5 μm , respectively, while reducing the diameter by almost half. Design analysis demonstrated the potential for further improvement with the used of custom lenses. These improvements enabled imagining of stained tissues and of intrinsic tissue signals from SHG, as shown in Fig. 2.1e in the upper and bottom images, respectively.

Our most recently developed third probe, which was developed working together with our past post-doc scholar Dr. Onur Ferhanoglu, offers a further reduction in diameter and provides an improved microsurgery speed through utilization of a compact, high repetition rate (300 kHz) erbium-doped ultrafast fiber laser (1552nm/776 nm, 3 W Discovery, Raydiance Inc.) [89]. This probe consists of a piezoelectric tube actuator for fiber scanning and two aspherical lenses that collimate and focus the light, resulting in a

simple in-line optical architecture with 5-mm overall housing diameter, as shown in Fig. 2.1c. We further improved the lateral and axial resolutions, which were measured to be 1.16 μm and 11.35 μm , respectively. A FOV of 150x150 μm^2 could be scanned in a Lissajous pattern using peak voltages as low as 20V, complying with safety limits within human body. With the given FOV and resolution, near 100% of the resolvable spots are sampled at least once in only 50 millisecond. Figure 2.1f (upper) illustrates ablation of gold on glass samples as exposed to two different scanning durations. The entire FOV could be ablated for 50 ms scanning duration, whereas only ~80% of the FOV could be ablated within 25 ms duration, leaving a small non-ablated area in the middle. These results demonstrate a potential speed of microsurgery as fast as 1 mm^2/s for near total ablation. Using this 5-mm probe, we demonstrated ablation of ex vivo scarred hamster cheek pouch using 200 nJ pulses. We could drill through the fixed tissue, which was approximately 70 μm thick, in under 10 seconds. Figure 2.1f (lower) illustrates the post-ablation SHG image of the tissue, acquired with a bench-top nonlinear microscope. Despite the narrow bandwidth of the fiber laser used in this study, this probe could still provide fluences that were higher than optical breakdown in the absence of pre-chirping to reduce laser intensities during fiber-coupling. With further development, this probe can serve as a precise and rapid ultrafast laser scalpel in the clinic.

2.5: CLINICAL MOTIVATION: MEDICINE AT THE MICROSCALE

As the frontiers of medicine and biology extend into the microscale and nanoscale, new needs are arising for novel biomedical tools. Specifically, these tools will need to be capable of providing visualization of genetic, metabolic, and morphological information with subcellular resolution, thus enabling increasingly specific diagnosis and disease staging. These tools will also need to be capable of providing treatment at the

microscale to create fine-tuned outcomes and treat localized cells in early-stage disease. Femtosecond laser pulses have emerged as a promising technology which could be used for both microsurgery and imaging to address these needs. By packaging this technology in a flexible, miniaturized endoscope, combined FLMS and NOI could be used for microscale diagnosis and treatment in many medical fields, including oncology and neurosurgery.

The field of oncology is one which could readily benefit from a tool capable of real-time combined cellular imaging and microsurgery. In 2012, cancer caused 1 out of 6 American deaths [90]. By far, the most effective way to reduce cancer death rates is to increase prevention and early detection. In fact, 85% of cancers originate in the epithelium, the layer of cells hundreds of microns thick that lines the skin and body cavities. If these small neoplastic lesions are detected and eliminated before penetrating the basal membrane, patient survivability approaches 100%. Currently, when a suspicious lesion is identified and suspected to be cancerous, the gold standard for cancer diagnosis is to surgically biopsy the suspect tissue for analysis by a histopathologist. Unfortunately, this process is time consuming, costly to the healthcare system, and causes patients significant discomfort. Alternatively, a combined ULMS and NOI tool could provide real-time optical biopsy by imaging the tissue in situ, potentially presenting metabolic or gene-expression information in addition to the standard morphological indicators used in histopathology. Because both NOI and ULMS at near infrared laser wavelengths can penetrate throughout the epithelial layer, a combined NOI/ULMS tool would be uniquely suited to not only provide real-time diagnosis, but to microsurgically remove small regions of diseased cells in the event of a positive diagnosis. Moreover, a ULMS endoscope could be potentially powerful for ablating cancerous cells in sensitive areas such as the vocal folds, while maximizing retained functionality after surgery.

Microscale imaging and treatment is perhaps most vital to the field of neurosurgery [91, 92]. In neurosurgery, every cell counts; thus, there are many potential applications for a device capable of combined NOI and FLMS. The visualization and removal of small regions of cancerous cells would be even more beneficial in the brain. Here it would allow neurosurgeons to be more conservative during resection to avoid removing healthy brain tissue, knowing that a sensitive cellular-level imaging and treatment technology could be used after bulk surgery to clean the tumor margins [92]. This method would be particularly useful because, though tumors in the central nervous system often cannot be distinguished from the surrounding healthy tissue by conventional intraoperative imaging [91], researchers have shown that two-photon microscopy methods can be used to image brain tumors with high contrast to the surrounding tissue [22]. Because of this discriminative imaging ability, an NOI, specifically two-photon microscope, and ULMS endoscope device could be useful for neuronavigation as well as treatment.

In addition to neuro-oncology, NOI-guided ULMS could be useful for functional neurosurgery as well, where ULMS has already proven adept at severing individual axons (neural connections) without damaging nearby tissue [32, 42]. As the field of neuroscience continues to mature and further understanding of individual neural pathways is gained, targeted axotomy may prove useful for achieving specifically tailored outcomes for diseases such as Parkinson's and epilepsy. Alternatively, NOI-guided FLMS could be used to replace conventional surgical instruments in certain current surgical procedures. For example, in endoscopic third ventriculostomy, an endoscope is used to perforate the floor of the third ventricle to relieve obstructive hydrocephalus. Currently, the ventricle is most often perforated by twisting a dull glass tube through the brain tissue. Though lasers have been successfully used for perforation of the ventricle

floor, they are frequently avoided due to concerns over heat dissipation damaging the nearby sensitive tissue [93, 94]. Due to the decreased heating and thermal dissipation during femtosecond laser-based ablation, this procedure could potentially be done with less mechanical trauma to the surrounding cells while still avoiding collateral damage from heating.

Despite advances in NOI and ULMS techniques and technology, many obstacles still remain before these treatments become reality. Some of these obstacles are specific to certain applications, such as which contrast agents to use (if at all) and how to apply them. Solutions to these problems are arising everyday as medical knowledge expands. The primary obstacle that must be first addressed, however, is the creation of a device capable of delivering femtosecond laser pulses at microsurgery-level pulse energies while also being small enough and flexible enough that it can reach the desired operating areas with a minimal degree of invasiveness. In addition to being small and flexible, however, the device must also have the imaging speed, field of view (FOV), resolution, and signal collection efficiency to meet the needs of this wide variety of clinical applications. Though there has yet to be a clinical demonstration of any in-vivo fiber-based ULMS probe, progress has been made in the area of miniaturized NOI devices for biomedical imaging.

Chapter 3: Parameters Affecting Ultrafast Laser Microsurgery of Subepithelial Voids for Scar Treatment in Vocal Folds¹

3.1: INTRODUCTION

Recently, there have been significant developments in phonosurgery, the surgical treatment of vocal fold pathology, but vocal fold scarring remains a therapeutic challenge [1]. Chronic voice impairment due to vocal fold scarring is estimated to affect ~4 million people in the US alone [2]. However, there is no reliable treatment for restoring proper phonation to individuals with scarred vocal folds. One of the current treatment methods, speech therapy, consists of training appropriate voice behavior [95]. Although this technique has been reported to improve voice quality in some cases, surgical restoration of scarred phonatory mucosa is still difficult to achieve in the clinic [96]. The use of injectable materials to restore pliability of the superficial lamina propria (LP) is a strategy that has shown promise in pre-clinical studies [1, 3-7]. Ongoing development of such materials is a significant research focus in the field of phonosurgery. A common unsolved problem facing the surgical use of injectable materials is their accurate and effective placement in a superficial plane in scarred vocal folds.

Contemporary understanding of the microanatomy of the human vocal fold [8] reveals a layered structure that consists of epithelium as the outermost layer followed by the LP and the vocalis muscle. The LP can be subdivided into superficial, intermediate, and deep lamina sub-layers based on distribution of extracellular matrix (ECM) fibrous proteins such as collagen and elastin. Collagen and elastin fibers are largely responsible

¹ Yildirim Murat, Onur Ferhanoglu, James Kobler, Steven M. Zeitels, and Adela Ben-Yakar. "Parameters affecting ultrafast laser microsurgery of subepithelial voids for scar treatment in vocal folds." *Journal of biomedical optics* 18, no. 11 (2013): 118001-118001. Murat Yildirim designed and performed the experiments. Onur Ferhanoglu helped performing the experiments. James Kobler and Steven Zeitels provided hamster samples. Adela Ben-Yakar supervised the project.

for providing the strength and elasticity of the vocal folds. The superficial lamina propria (SLP) has a thin sheet of collagen fibers that are highly aligned along the length of the vocal fold [9]. Below these fibers, the SLP mainly consists of amorphous ground substance (primarily, proteoglycans and glycosaminoglycans) with scattered elastin and collagen fibers, fibroblasts, and other elements typical of loose connective tissue [10]. During the wound healing response, scar tissue can replace the SLP along with deeper parts of the LP. The scar tissue predominantly consists of collagen and fibronectin, both of which increase the stiffness of the mucosa and can lead to severe impairment in voice production, or dysphonia [1].

According to Zeitels and colleagues [11], injection of soft biomaterials in the sub-epithelial region of scarred vocal fold tissue is likely to be challenging due to presence of dense scar tissue. Such dense tissue could require high injection pressures and limit precision since injections tend to take a path of least resistance. We propose to overcome this challenge by creating a planar ablation void - essentially a thin sub-epithelial plane of separation that injected substances could easily dissect into, forming a mattress-like layer similar to normal SLP regardless of scar tissue inhomogeneities [13]. The ablation plane would ideally encompass the scarred phonatory area, which could extend over an area as large as $3 \times 10 \text{ mm}^2$ in a heavily scarred vocal fold. We hypothesize that such void will reduce the required injection pressure and improve the superficial localization of an injected biomaterial for restoration of a phonatory mucosal wave.

Focused ultrafast laser pulses are uniquely suited for creating sub-surface voids. Having short pulse durations and thus high peak intensities, ultrafast lasers ensure the use of minimal energies for high precision ablation with minimal damage to surrounding tissue. Ablation of a dielectric material, such as tissues, with ultrafast laser pulses begins with generation of free electrons through combination of multi-photon ionization and

band-gap (Zener) tunneling [29, 30]. The quasi-free electrons may then act as seed electrons for avalanche ionization. During avalanche, quasi-free electrons accelerate by gaining kinetic energy from the incident laser field. Accelerated free electrons collide with bound valence electrons and ionize them through impact ionization. This exponential multiplication process repeats and cascades until the termination of the laser pulse. The final value of the free electron density determines the photo-damage mechanism, which can be photochemical, induced by thermo-elastic stress confinement, or a result of optical breakdown when a critical electron density is reached [31, 32]. In the thermo-elastic stress confinement, thermalization of the plasma occurs faster than the acoustic relaxation time [30]. The confinement of thermal stresses can overcome tensile strength of tissue and lead to its tearing. Similarly, tissue fracture/tearing may occur in the optical breakdown regime due to the shock wave formation as the strength of the pressure increase across the shock wave exceeds tissue tensile strength [27].

In addition to mechanical effects, the mechanism for the free electron generation determines the ablation threshold that depends on the laser pulse duration, initial seed electrons, and the linear absorption of tissue. The multiphoton ionization dominates the free electron generation for pulse widths < 100 fs [33]. At longer pulse durations in the range of 500 fs – 10 ps, the contribution of cascade ionization to the formation of free electrons increases by at least 3 – 4 orders of magnitude, however, with no drastic change in the ablation threshold and the thermo-mechanical effects [34]. Lower threshold fluence can be observed in the presence of initial seed electrons in the focal volume due to impurities. However, this effect is only noticeable for pulse widths > 10 ps [35]. As for the effect of linear absorption, a 2 – 3 fold decrease in the ablation threshold can be observed if tissue absorption coefficient is increased by 3 orders of magnitude from 0.1 to 22 cm^{-1} [36].

The ultrafast ablation process relies upon efficient and rapid energy absorption at the focal plane which results in minimal energy deposition to the surrounding tissue. The nonlinear nature of the process further confines the efficient absorption to sub-focal volumes. Such a high-degree of damage confinement is especially important when working with delicate tissue such as vocal folds and may reduce post-ablation scar formation. Successful laser microsurgery of vocal fold tissue using femtosecond laser pulses has been previously demonstrated, showing the potential for sub-surface ablation confined within the sub-layers of the LP by our group [13] and others [97].

To guide ultrafast laser microsurgery, focused ultrafast laser pulses can also be used to visualize intrinsic molecular and morphological properties of tissues through nonlinear optical microscopy. Specifically, simultaneous two-photon autofluorescence (TPAF) and second harmonic generation (SHG) microscopies [50, 98, 99] can provide complementary information on the structure of the superficial layer of vocal folds and scar tissue that might be present. The use of near infrared (NIR) wavelengths provides superior penetration depth for nonlinear microscopy techniques with respect to conventional fluorescence microscopy. Low-energy ultrafast laser pulses for imaging can thus provide ultrafast laser microsurgery devices a means for visualizing the region of surgery with the identical field of view and resolution of the surgical laser.

We have recently demonstrated fiber-based miniaturized probes for delivering ultrafast laser pulses for microsurgery and nonlinear imaging [60, 61] and found that we could create two-dimensional voids within porcine vocal folds using laser and focusing parameters that are deliverable with these probes [13]. Here, we examine the effect of morphological and structural differences on the creation of thin voids within *ex vivo* tissue samples. We specifically compare ablations in superior and inferior porcine vocal folds, and healthy and scarred hamster cheek pouches. Our primary goals are to

characterize the ablation parameters such as ablation threshold fluence (pulse energy per area of the focused laser spot), maximum ablation depth, and dynamics of bubbles in sub-epithelial voids in these samples.

3.2: METHODS AND MATERIALS

3.2.1: Experimental Setup

We upgraded our home-built, bench-top laser-scanning microscope (Figure 3.1) to include two channels for simultaneous imaging of two-photon autofluorescence (TPAF) and second harmonic generation (SHG) signals. For both microsurgery and imaging, the microscope uses a single ultrafast laser system; a 303 kHz (or 2 MHz) repetition rate, 3 W erbium-doped fiber laser (1552 nm/776 nm Discovery, Raydiance Inc.). This laser is a slightly modified version of the one used in our previous study [13] and provides two modes of repetition rate, a 2 MHz mode (1 ps pulse duration) and a 303 kHz mode (3.2 ps pulse duration). It can be frequency doubled to 776 nm with a 36% conversion efficiency at the SHG box. At 776 nm, the laser produces maximum pulse energies of 0.5 μJ and 3.6 μJ , at 2 MHz and 303 kHz, respectively. The overall optical transmission of the microscope at 776 nm is 42%, delivering maximum pulse energies of 0.2 μJ and 1.5 μJ , at 2 MHz and 303 kHz, respectively, to tissue surface.

We focused the laser beam with a 0.75-NA, 20 \times air objective (Nikon Plan Apo) to a spot size achievable in our recent miniaturized microsurgery probes [60, 61]. We characterized the spatial distribution of laser beam at the focal volume by measuring the two-photon point spread function (IPSF²) of our system. Specifically, we used 100 nm fluorescent beads (Invitrogen, F8803) suspended in agar gel at a concentration of 2×10^{10} beads/ml and covered with a glass cover slip (0.17 mm thickness). This bead

concentration provided an equivalent scattering length of $35 \mu\text{m}$ at 776 nm excitation wavelength, which was in the range of effective scattering length of lamina propria of our samples. Independently, previous studies have demonstrated that the IPSF^2 in turbid media is constant in the range of our imaging depths as the two-photon signal is mainly generated by the ballistic photons reaching to the focal volume [100-102]. The average lateral and axial FWHM of the IPSF^2 were measured to be $0.58 \pm 0.07 \mu\text{m}$ and $2.17 \pm 0.15 \mu\text{m}$, corresponding to $1.39 \pm 0.17 \mu\text{m}$ and $5.21 \pm 0.37 \mu\text{m}$ $1/e^2$ diameter of the intensity distributions. The $1/e^2$ diameter of the intensity distribution is $2/\sqrt{\ln(2)}$ times of the FWHM of the IPSF^2 [50].

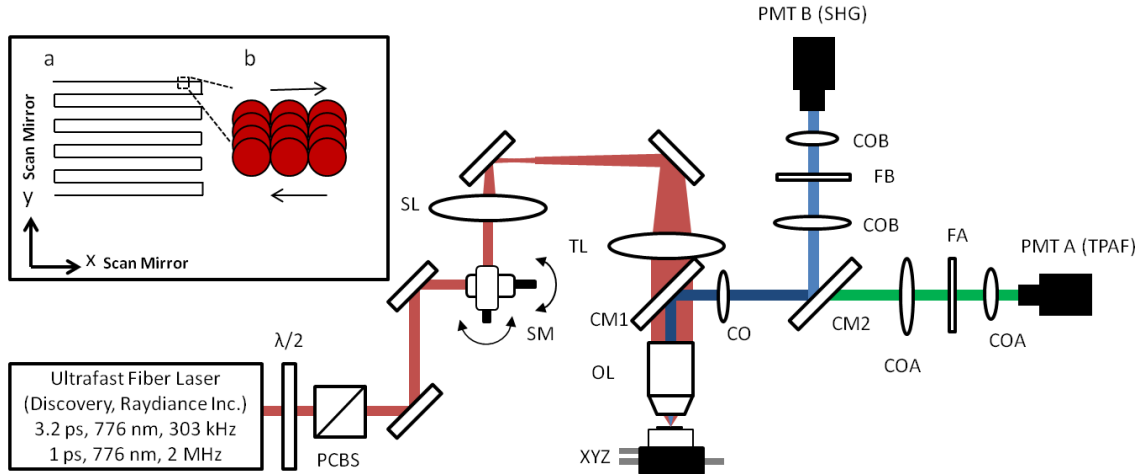


Figure 3.1. Schematic of the two-channel, bench-top microscope for combined nonlinear imaging and microsurgery. Ultrafast laser pulses from a compact fiber laser system pass through an energy attenuator consisting of a half-wave plate ($\lambda/2$) and polarizing cube beam splitter (PCBS). The beam is scanned by a pair of galvanometric scanning mirrors (SM) through a scan lens (SL) and tube lens (TL) which image the beam on the SM to the back aperture of a 0.75-NA, 20x objective lens (OL). The laser pulses irradiate the sample placed on a three-axis motorized stage (XYZ), for either ablation or imaging. Emitted light is collected by a cold mirror (CM1- HT-1.00, CVI Laser) and collection optics (CO). A second cold mirror (CM2 - Di01 - R405, Semrock) separates the SHG and TPAF signals into different collection paths. We collect the TPAF signal through collection optics A (COA) and a laser blocking filter (FA) into the PMTA (H10770PA-

40, Hamamatsu) and the SHG signal through collection optics B (COB) and a laser blocking filter B (FB) into the PMT B (R3896, Hamamatsu). The two PMT's, stage, and scanning mirrors are all connected to a personal computer through data acquisition cards (not shown). Insets show (a) the schematic of the laser-scanning pattern at the sample during microsurgery and (b) the degree of overlap between subsequent laser pulses.

For microsurgery, we raster-scanned the laser beam at a single depth below the surface for the duration of one frame, namely 310 ms (3.21 fps), using a pair of galvanometric mirrors (Cambridge Technologies, Inc.). The inset in Fig. 3.1 shows how the focal spot was swept over a $250 \times 250 \mu\text{m}^2$ area. This scanning mechanism was slightly different than the one used in our previous study [13] where the surgery beam was raster-scanned only in one direction while a translation stage continuously moved the sample in the other direction. With a goal to minimize the ablation duration, we chose to use minimal continuous overlapping of the laser pulses in the direction of the scanning. A low degree of overlapping improves the possible beam distortion of consequently overlapping pulses as well as improves the speed of ablation. However, without significant pulse-to-pulse accumulation effects, higher pulse energies are usually needed for complete ablation [32]. The choice of one overlapping pulse in the x -direction (822 Hz) automatically dictates approximately three overlapping pulses in the y -direction (3.21 Hz) by the imaging software (MPScan). Considering it takes 310 ms to scan a $250 \times 250 \mu\text{m}^2$ wide region, we can estimate the speed of ablation with 3 overlapping pulses as $12 \text{ mm}^2/\text{min}$.

The axial displacement of the sample was performed using a motorized stage. The amount of the axial movement of the stage results in a focal shift within the tissue due to the index of refraction mismatch at the air/tissue interface. The ratio of the real displacement within tissue to that of the stage, the focal shift ratio, is defined by the ratio of the refractive index of the tissue to the medium in which it is immersed in. We

experimentally determined the focal shift ratio of the air lens through taking a stack of images and comparing it to the images acquired with a water-dipping lens, having a negligible mismatch at the water/tissue interface. By comparing images at different depths, we observed the focal shift ratio to be 1.2, slightly less than the expected value of 1.33. We attributed the low focal shift ratio possibly to positive spherical aberrations observed in the air objective, when focused in tissue samples. In our experiments, we therefore multiplied the stage displacement by the measured ratio of 1.2 to obtain the correct focal shift, thus axial scaling, within the tissue.

3.2.2: Ex vivo tissue samples

The elastin and collagen distributions within the porcine lamina propria (LP) have been shown to be similar to human [103-105]. As a model of scarred mucosa, we used the hamster cheek pouch. The hamster cheek pouch model has been accepted as one of the best animal models for studying epithelial diseases [106-108] and determining the efficacy of treatments [109-111]. In order to understand the effect of fiber structure and morphology on ablation, we used five fresh porcine vocal folds (superior and inferior) and three Golden Syrian hamster cheek pouches (healthy and scarred).

3.2.2.1: Fresh Porcine Vocal Folds

We acquired fresh porcine airway specimens from a local slaughterhouse and isolated the larynx in a room temperature saline bath within 2 hours after sacrificing the animal. Porcine vocal folds have layered LP very similar in structure to human vocal folds. Although some preliminary studies showed the presence of a prominent sub-epithelial collagen layer in the SLP, there is no agreement whether the superior or inferior LP of the porcine is primarily responsible for phonation [112]. Therefore, we decided to use both superior and inferior porcine vocal folds for our experiments to test whether

differences in their microanatomy correlate in meaningful ways with differences observed in laser ablation and imaging.

After excision, we placed each vocal fold in saline and covered it with a glass cover slip (0.17 mm thickness) to flatten the surface. In a clinical application, the glass cover slip would be akin to having the window of a microsurgery probe in contact with the sample, thus helping to maintain a constant depth of ablation. Short-lived cellular autofluorescence of fresh tissue samples guided us to identify the surface of the sample during imaging.

For follow-up histology, we placed the superior and inferior vocal fold samples in 10 mL of 10% formalin (SF98-4, Fisher) and stored them at 4 °C for at least 48 hours prior to paraffin embedding, sectioning, and staining (TherapeUTex; Austin, Texas). The dehydration process was performed with ethanol and Citrisolv. A combination Masson-Trichrome and Verhoeff staining was used to differentiate elastin and collagen [113].

3.2.2.2: Hamster Cheek Pouch Mucosa as a Scar Model

We used adult male Golden Syrian hamsters (Charles River Labs, Wilmington, MA) of 100 – 120 g. body weight as an animal model in which scar can be created within an easily accessible mucosal surface. The goal in these experiments was to observe how the structural differences between normal and scarred buccal mucosa affected ablation results. To scar the cheek pouches, we first anesthetized the animals by injecting a mixture of Ketamine (200 mg/kg) and Xylazine (8 mg/kg) intraperitoneally. We then cauterized 5 – 10 mm diameter circular areas of one cheek pouch with an electrocautery unit (Conmed Saber 2400). The hamsters were euthanized after a survival period of 1 month using 0.5 ml intraperitoneal Euthasol. The scarred and contralateral normal cheek pouches were removed and mounted on rubber test-tube stoppers with fine needles to

hold the cheek pouch mucosa flat. After rinsing with saline, the tissue was frozen in isopentane cooled in liquid nitrogen. The cheek pouch tissue was prepared at Massachusetts General Hospital Voice Laboratory (MGH) in Boston and shipped on dry ice to the Ben-Yakar Laboratory at the University of Texas at Austin for bench-top testing. After delivery, the cheek pouches were stored at -80 °C. For each experiment, we thawed the cheek pouches in saline solution and covered them with a glass cover slip to flatten their epithelial surface.

For the histological analysis of the healthy and scarred tissue, we placed them in 10 mL of 10% formalin (SF98-4, Fisher) and stored them at 4 °C prior to paraffin embedding, sectioning, and staining (TherapeUTex; Austin, Texas). For cheek pouches, an additional dehydration step with ethanol and xylene was added due to the abundant fat content in this tissue. Masson-Trichrome staining was used to show the orientation of the collagen fibers [113].

3.3: RESULTS

3.3.1: Imaging of Tissue Architecture

We combined two-photon autofluorescence (TPAF) and second-harmonic generation (SHG) nonlinear imaging modalities for characterizing the tissue architecture of our samples, identifying the desired depth for laser ablation, analyzing the dynamics of the ablated voids, and finally characterizing the tissue ablation properties. The combination of SHG and TPAF imaging is a powerful method to differentiate the structure and type of fibers in the SLP, whether it is made of collagen and/or elastin. Previous studies have shown that elastin fibers auto-fluoresce [114-116] but cannot produce SHG signal, while a wide variety of collagen fibers generates SHG [99]. Therefore, SHG is considered to be selective of collagen fibers. Since some collagen

types with SHG signal can also auto-fluoresce [116], TPAF alone, however, is not considered to be selective of elastin fibers. Therefore, combined SHG and TPAF imaging is necessary to clearly identify the fiber type and its density.

Figure 3.2 shows a stack of representative overlaid images of TPAF and SHG signals through the mucosa of fresh superior porcine vocal fold. Close to the surface, only TPAF (red) signal, originating from the epithelial cells, was visible. Starting at a depth of 42 μm SHG (green) signal accompanied TPAF, indicating the existence of fibrous structures. The SHG showed thick bundle-like fibers, while the TPAF showed thin, and long fiber structures. The orientation of these signals was different, suggesting they might be originating from different fiber structures. As imaging depth increased, the SHG-generating structures became denser, covering the whole FOV. Beyond 120 μm , the contrast decayed substantially.

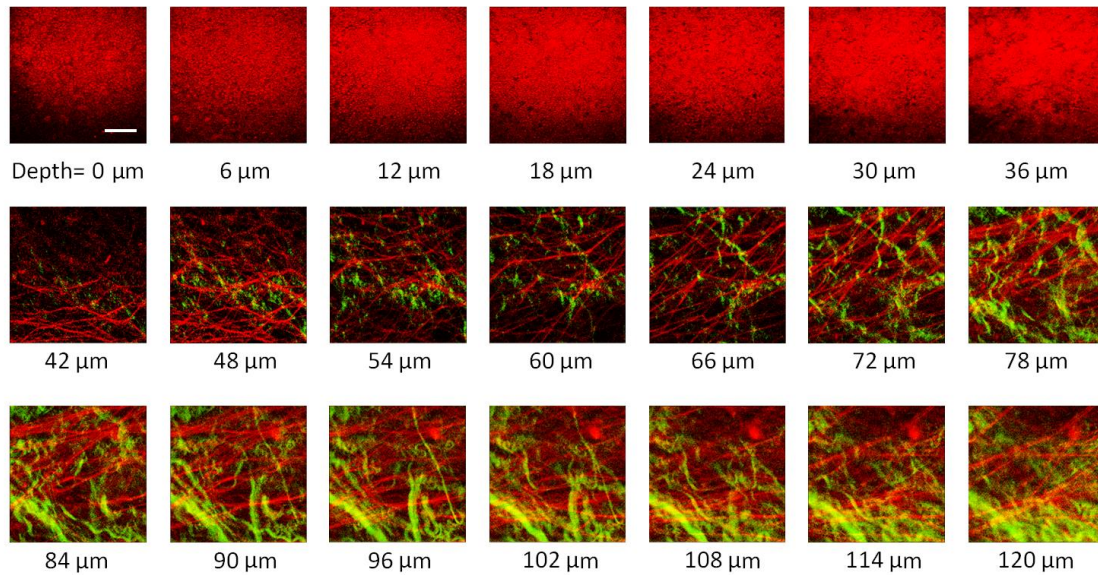


Figure 3.2. Overlaid TPAF (red) and SHG (green) images of fresh superior porcine vocal fold. TPAF signals from epithelial cells are observed until a depth of 36 μm and then TPAF and SHG signals from different fiber structures are detected up to 120 μm depth, beyond which the imaging contrast decays substantially. We increased the average

imaging power gradually from 0.9 mW at the surface to 6 mW at 120 μm depth. The scale bar represents 100 μm .

Figure 3.3 shows representative images of porcine inferior vocal folds. Here the TPAF and SHG signals overlaid better than was seen for the superior vocal folds, suggesting they were originating from similar fibers. Since SHG mainly originates from collagen, these SHG-positive fibers in the inferior vocal folds were mostly collagen with less elastin content as opposed to superior vocal folds.

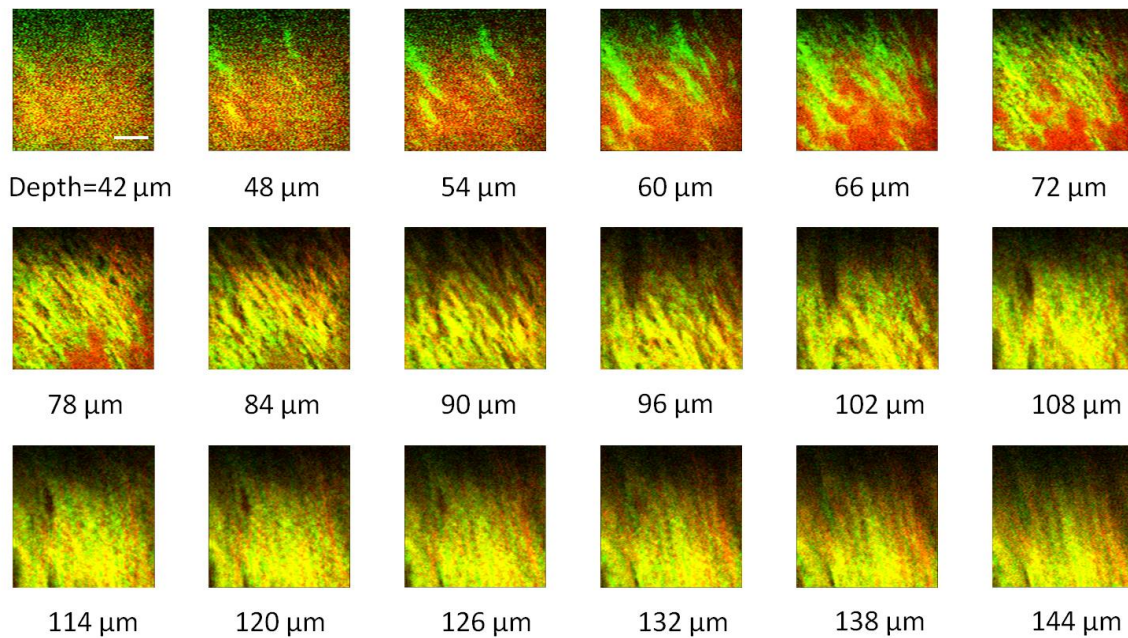


Figure 3.3. Overlaid TPAF (red) and SHG (green) images of fresh inferior porcine vocal fold. The overlaid signals appear in yellow. Both TPAF and SHG signals show similar fiber structures that can be detected up to 144 μm , beyond which the imaging contrast decays substantially. We increased the average imaging power gradually from 0.9 mW at the surface to 8.2 mW at the maximum imaging depth. The scale bar represents 100 μm .

To identify the type of fibers in the vocal folds more deterministically, we used stains selective for collagen and elastin fibers. Specifically, we used a combined Masson-Trichrome/Verhoeff method that stains collagen fibers green and elastin fibers black [113]. Thin smooth elastin fibers (black) and wavy collagen bundles (green) were visible

in the superior vocal fold (Fig. 3.4(a)), while mostly collagen and sparsely distributed elastin fibers were seen in the inferior vocal fold (Fig. 3.4(b)), confirming our observations from nonlinear imaging.

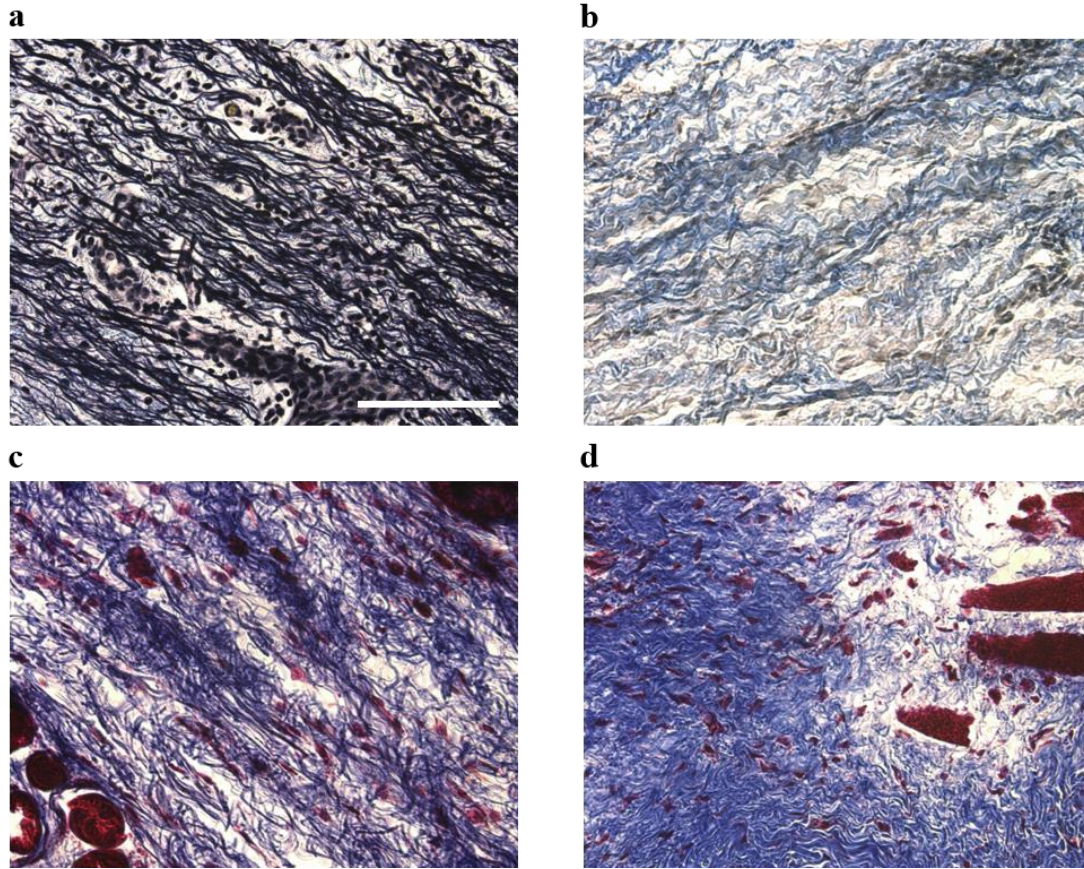


Figure 3.4. Histology images of porcine vocal folds and hamster cheek pouches. (a) Superior and (b) inferior vocal folds at 70 μm depth with combined Masson Trichrome (shows blue for collagen fibers) and Verhoeff (shows black for elastin fibers) stain. (c) Control and (d) scarred cheek pouches at 70 μm depth with Masson Trichrome stain. Scaling bar represents 100 μm .

We next studied the morphology differences between control and scarred hamster cheek pouches. Similar to the porcine vocal folds, the cheek pouch consists of a thin squamous epithelium with a thickness varying between 35 - 45 μm , a thin LP of loose connective tissue, and underlying striated muscle. As would be expected with previously frozen tissue samples where the main autofluorescence sources such as NADH, NADPH,

and flavins would be substantially degraded, TPAF signal could not be observed in the epithelium. Unlike the porcine vocal folds, we did not observe any TPAF signal below the epithelium in the region where a substantial SHG signal was present.

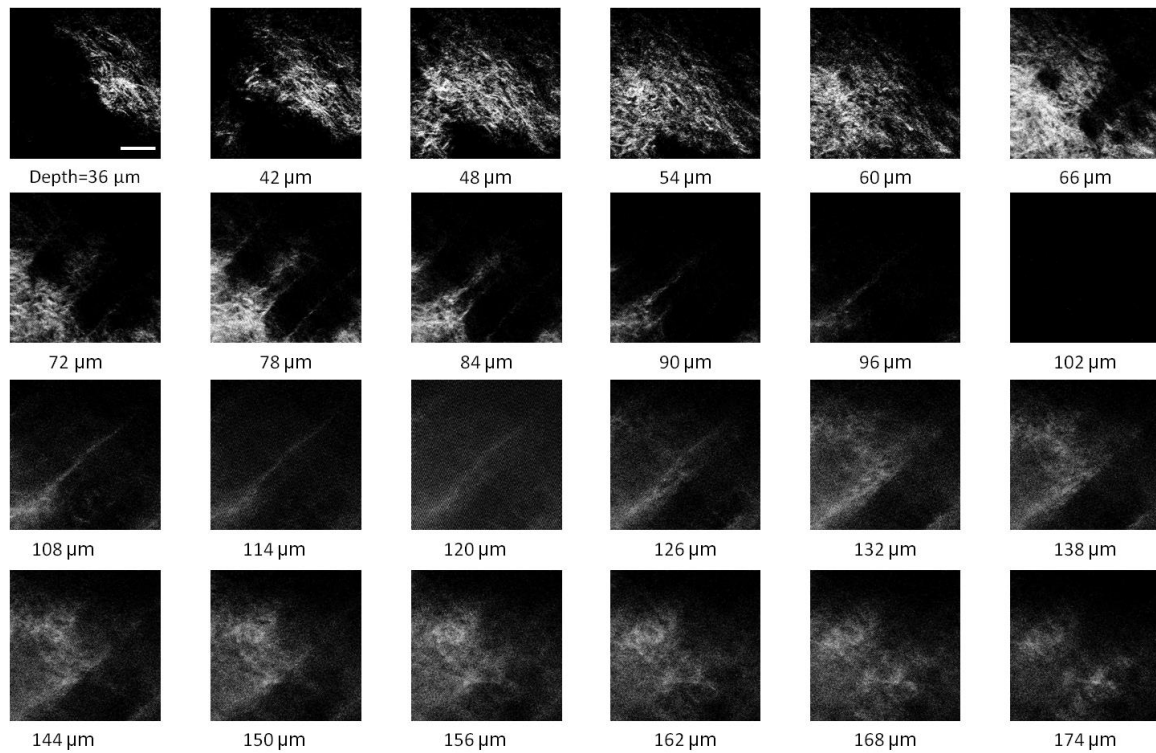


Figure 3.5. Representative SHG images of control hamster cheek pouch samples. Starting at 36 μm depth, SHG signals shows randomly aligned collagen fibers with an increasing, decreasing, and again increasing density. We increased the average imaging power gradually from 0.8 mW at the surface to 9.6 mW at 174 μm . The scale bar represents 100 μm .

Figures 3.5 and 3.6 show SHG images of control and scarred hamster cheek pouches, respectively. The SHG signal in both samples started to appear at a depth of 36 μm , first increasing and then decreasing in intensity along the tissue depth. This SHG signal most probably originates from collagen fibers, delineating the interface between the epithelium and LP. At a depth of 60 μm , the SHG signal covered almost the whole

FOV, where we chose to perform our ablations. Collagen fibers seemed to be randomly organized in the healthy control samples and more aligned and denser in the scarred samples, in agreement with another study that compared healthy and scarred rabbit vocal folds [117]. Histology analysis of the Masson-Trichrome stained hamster cheek pouches further confirmed these observations and provided insight on the pathology of the scarring. As compared to control (Fig. 3.4(c)), scarred tissue showed regular and dense patterns of collagen fibers (Fig. 3.4(d)).

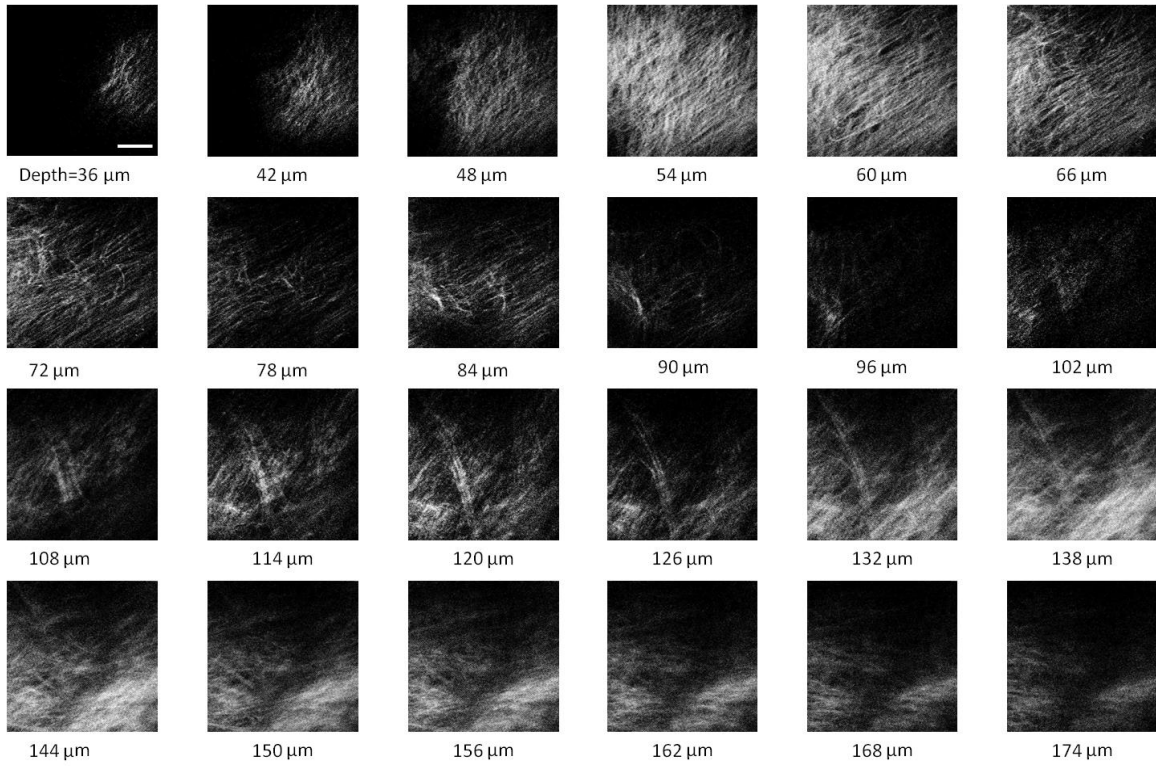


Figure 3.6. Representative SHG images of scarred hamster cheek pouch samples. Starting from 36 μm , SHG signals from uniformly aligned collagen fibers appear with an increasing, decreasing, and again increasing density. The scale bar represents 100 μm .

3.3.2: Ablation Studies

The primary goal of this work was to identify laser parameters for the successful ablation of sub-epithelial voids in vocal folds and how these parameters vary when ablating scar tissue. For each tissue sample, we investigated ablation threshold fluences (pulse energy per area of the focused laser spot), maximum ablation depth, and initial bubble size and lifetime.

3.3.2.1: Ablation versus Pulse Energy

We previously showed that ultra-short pulses with sub- μJ energies can create voids below the epithelium layer using 0.75-NA, 20 \times air objective [13]. Here, we studied how the size of these voids varies with the pulse energy and how scarring affects the ablation properties.

First, we verified how well nonlinear images correlated with the extent of the ablated voids by comparing them to histology images of H&E stained tissue. Figure 3.7 presents this comparison for two different pulse energies, including a near-threshold energy. Overall, there was a good correlation between the TPAF and histology images in terms of the extent and morphology of voids for each pulse energy. The void ablated with the near threshold energy of 250 nJ appeared incomplete and the one ablated with the higher energy of 750 nJ was more complete and uniform. Consistent with our previous study [13], histology images showed slightly smaller voids, mainly in their heights because of three potential reasons: 1) contraction during the histology preparation, 2) focal point shift in the TPAF images due to the deflection of the beam at the tissue-void interface as a result of the index of refraction mismatch between tissue and gas, and 3) shrinkage of voids during the period between TPAF imaging and tissue fixation. The heights of the voids were 40-50% smaller in the histology images as a result of the reasons mentioned above.

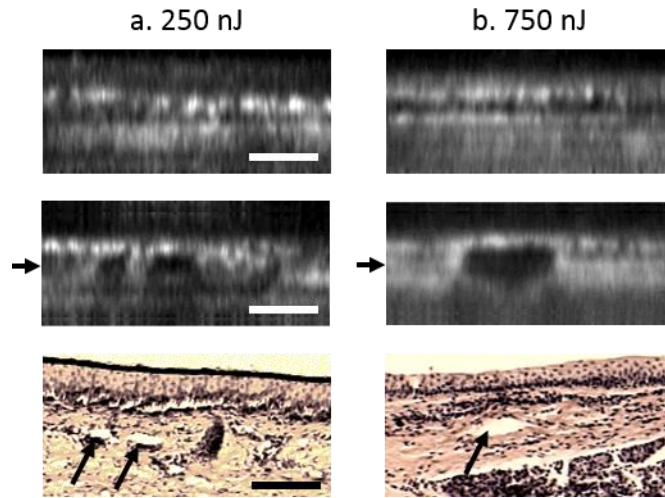


Figure 3.7. Comparison of cross-sectional TPAF images with histological analysis of voids in an inferior porcine vocal fold. The voids were ablated using (a) 250 nJ and (b) 750 nJ pulse energies at a depth of 90 μm beneath the tissue surface. Pre-ablation TPAF, post-ablation TPAF, and H&E stained histology images are presented in the first, second, and third rows respectively. Arrows in the TPAF images indicate the plane targeted for ablation. Arrows in the histology images indicate the location of the identified voids, corresponding well with the TPAF images. All scale bars are 100 μm .

We then studied ablation properties of healthy and scarred tissue samples. Figure 3.8 illustrates representative TPAF images of porcine superior and inferior vocal folds one minute after ablation with different incident pulse energies. The ablation depth was 90 μm , where collagen fibers covered the whole FOV and the plane of focus was completely below the epithelium within the SLP. We chose the ablation size (250 x 250 μm^2) smaller than the FOV for imaging (430 x 430 μm^2) to visualize the entire region of interest before and after ablation. The black areas with no signal presumably represent voids that are filled up with a temporary bubble containing gaseous products of the vaporized ablated tissue. At low pulse energies from 250 nJ up to 500 nJ, the ablation was partial and could not cover the whole targeted area and the bubbles appeared small and scattered. Pulse energies of 750 nJ and above provided a more uniform and complete ablation. Inferior porcine vocal folds repeatedly required slightly less energy to obtain complete ablation.

Figure 3.9 shows representative SHG images of control and scarred hamster cheek pouch samples one minute after ablation, performed at a depth of 60 μm where the SHG signal covered most of the FOV. While laser pulse energies of 150 nJ were just enough to initiate partially ablated spots in the control samples, they resulted in more uniformly ablated regions in scarred tissue. Scarred tissue repeatedly required less energy to obtain complete ablation.

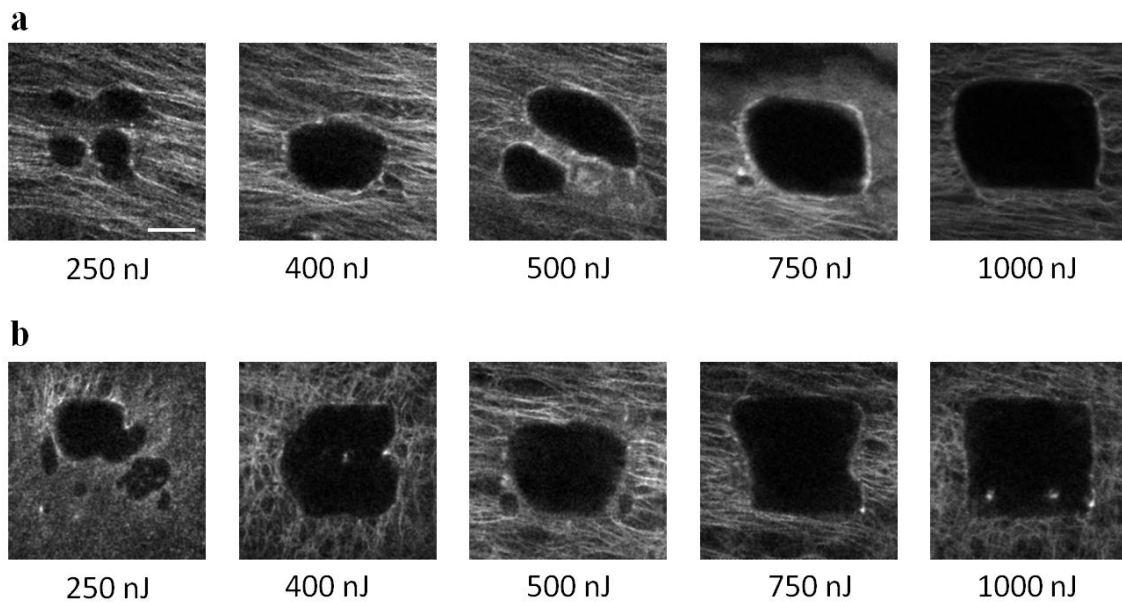


Figure 3.8. The effect of incident laser pulse energy on the subsurface ablation properties of porcine vocal folds. Two photon autofluorescence (TPAF) images show the characteristics of sub-epithelial voids (bubbles) one minute after ablation with different pulse energies (as measured at the surface) in superior (a) and inferior (b) vocal folds at the ablation depth of 90 μm . Scale bar indicates 100 μm .

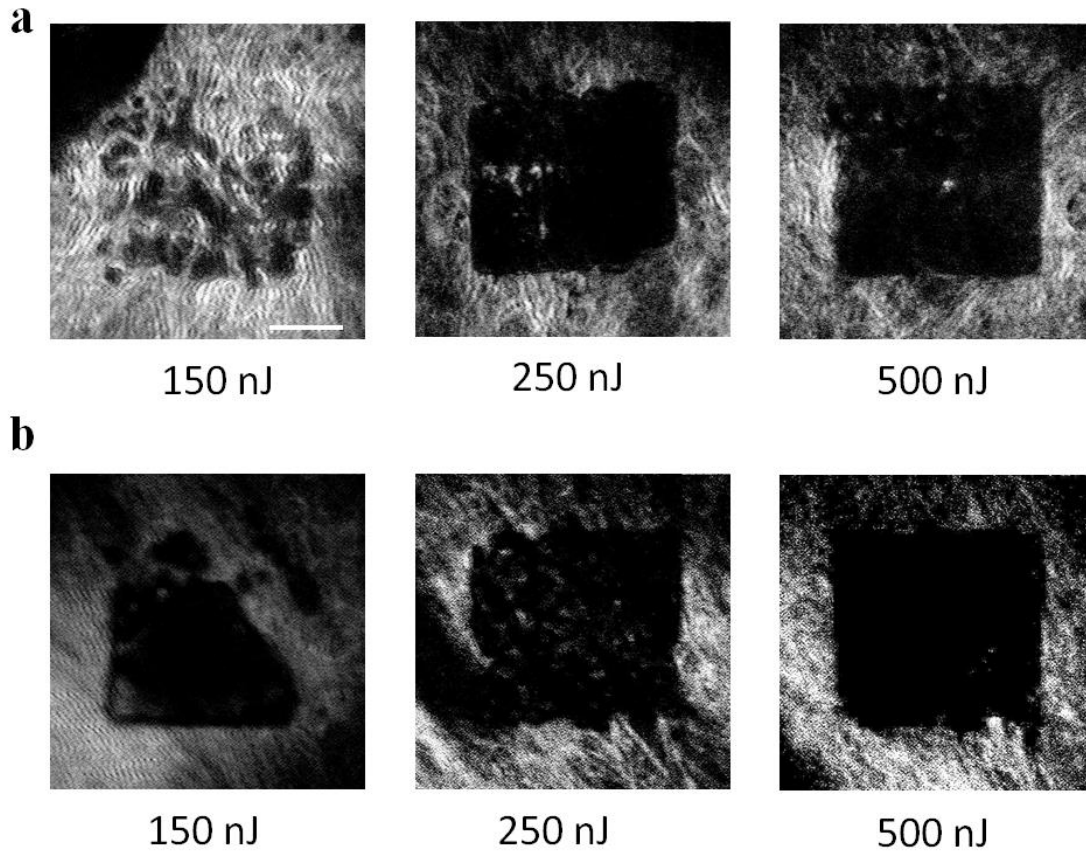


Figure 3.9. The effect of incident laser pulse energy on the subsurface ablation properties of hamster cheek pouches. Second harmonic generation (SHG) signal images of sub-epithelial voids (bubbles) for different incident energies one minute after ablation in control (a) and scarred (b) hamster cheek pouches at the ablation depth of 60 μm . Scale bar indicates 100 μm .

3.3.2.2: *Sample-to-Sample Repeatability of Tissue Ablation*

To understand how the ablation characteristics of a specific tissue type vary from sample-to-sample, we studied 5 sample sets of fresh porcine vocal folds (5 samples for superior and 5 samples for inferior) and 3 sample sets of hamster cheek pouches (3 samples for control and 3 samples for scarred) at 3 different locations per pulse energy per sample. We measured the initial area of the bubble at the targeted plane immediately after ablation for each incident pulse energy varying between 50 – 1500 nJ. Figure 3.10

represents the plots of these measurements as normalized to the size of the targeted ablation area of $250 \times 250 \mu\text{m}^2 = 0.0625 \text{ mm}^2$. A unit area is considered to indicate a complete ablation. As a general trend, the size of the bubbles gradually increased with the laser pulse energy and covered the whole targeted ablation area at higher energies.

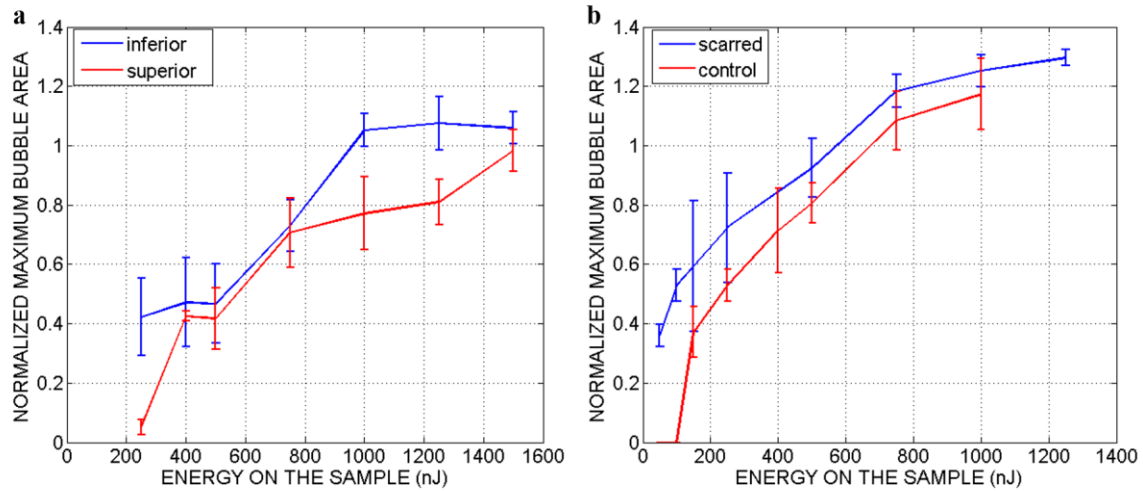


Figure 3.10. Normalized area of the initial bubbles in the ablated voids at different incident pulse energies one minute after ablation. Each data point represents an average of (a) 15 measurements in 5 fresh porcine vocal folds and (b) 9 measurements in 3 hamster cheek pouches. The error bars represent the standard deviation of the mean of the samples.

Figure 3.10(a) indicates that inferior vocal folds generally required less energy than the superior to create the same size of bubbles. The area of the initial bubble matched the targeted area as the incident pulse energy approached to $1.0 \mu\text{J}$ and $1.5 \mu\text{J}$ in the inferior and superior vocal fold, respectively, and exceeded the targeted area beyond those energy levels. The difference in the initial bubble area was also distinct close to the threshold energy. For example, ablation at 250 nJ resulted in minimally observable bubbles in the superior folds and in slightly larger bubbles, covering more than 40% of the targeted area, in the inferior. The ratios of the pulse energies for complete ablation

(100% of the area) and partial ablation (40% of the area) were approximately 4 for both types of vocal folds.

Figure 3.10(b) compares the bubble area results for healthy and scarred hamster cheek pouch samples. As shown in the previous section, the minimum energy required for ablation in this tissue was lower than for porcine vocal folds. Interestingly, however, the scarred tissue required less energy than the healthy tissue to initiate ablation at 60 μm depth. Close to threshold where 40% of the area is ablated, ablation initiated in the scarred tissue with incident energies as low as 50 nJ at which no bubble appeared in the healthy tissue. The initial bubble area approached the targeted area between 600 - 700 nJ pulse energy while it was consistently larger in scarred samples for the same energy levels.

The standard deviation of each data presented in Figure 3.10 show noteworthy differences in the areas of the initial bubbles. Nonetheless, we could extract general trends of each tissue type as the error bars of each tissue type did not significantly overlap with its counterpart (inferior vs. superior and control vs. scarred). To summarize, these results indicated that it was easier to ablate scar tissue than healthy tissue and it was easier to ablate inferior vocal fold than the superior vocal fold. In the next section, we will discuss hypotheses explaining these differences in ablation thresholds.

3.3.2.3: Ablation Threshold and Tissue Scattering Properties

The differences in the incident energy thresholds for different tissue types might be a result of one or both of the following factors: (1) the scattering length of the tissue that determines the portion of the incident energy reaching the focal volume and (2) the sensitivity of the specific tissue to ablation, which we refer to as tissue specific ablation threshold – TSAT fluence (F_{th}). Independent measurement of these two parameters is not

straightforward, as they depend on each other. While it is easy to measure the incident pulse energy at the surface that is required to initiate ablation at a given depth, the calculation of the energy reaching the actual ablation depth requires knowledge of the extinction properties of the tissue. Furthermore, the extinction properties might vary with depth as the light passes through different layers, e.g. from the epithelium into the LP. We therefore, developed a method to measure ablation threshold fluence and extinction properties of tissue simultaneously in a single set of experiments.

In our approach, we assumed that scattering dominated the extinction properties of tissue in the NIR wavelengths and is different in the epithelium and LP but constant within each layer. This assumption is valid since the absorption coefficients are expected to be three orders of magnitude smaller than the scattering coefficients as observed in skin epidermal measurements [118, 119]. We also assumed that the TSAT was independent of depth within the LP and thus should remain constant in the targeted regions of sub-epithelial ablations. Finally, we assumed that Beer's Law could be used to estimate the attenuation of light reaching the focal volume, since the nonlinear ultrafast ablation processes are mostly governed by the ballistic photons reaching the focal plane.

In the light of these assumptions, we measured the minimum incident energy required to initiate ablation at three ablation depths, z_{ab} , and used the Beer's law to describe the exponential beam attenuation with depth for each case:

$$F_{th} = \frac{E_{th,surface}}{\pi w^2} \cdot \exp\left(\frac{-z_{ep}}{\ell_{s,ep}} - \frac{z_{ab}-z_{ep}}{\ell_{s,LP}}\right) = \frac{E_{th,surface}}{\pi w^2} \cdot \exp\left(\frac{-z_{ab}}{\ell_{s,eff}}\right) \quad (1)$$

Here, the pulse energy reaching to the focal plane at the ablation depth decays exponentially with the effective scattering length, $\ell_{s,eff}$;

$$\ell_{s,eff} = \frac{z_{ab} \cdot \ell_{s,ep} \cdot \ell_{s,LP}}{z_{ep} \cdot \ell_{s,LP} + (z_{ab} - z_{ep}) \cdot \ell_{s,ep}} \text{ if } (z_{ab} > z_{ep}) \quad (2)$$

We could then estimate the three unknown parameters, TSAT fluence at the focal plane, F_{th} , epithelium scattering length, $\ell_{s,ep}$, and LP scattering length, $\ell_{s,LP}$ by solving Eq. (1) at three depths. The radius of the laser beam at the focal plane was $w = 0.7 \mu\text{m}$ and the local epithelium thickness, z_{ep} , was measured via the nonlinear images for each ablation data point.

To find the three unknowns in our experiments, we performed ablations at three different depths (72, 90, and 108 μm for porcine vocal folds and 60, 78, and 96 μm for hamster cheek pouches). At each depth, we measured the local z_{ep} and found $E_{th,surface}$, defined as the energy required to create an initial bubble covering 40% of the targeted area. For each tissue type, we used two samples and for each depth, we collected data at 3 different locations to obtain an average value. The results are tabulated in Table 3.1 and the data points for each tissue.

These data shed light on the ablation threshold results observed in the previous section. We found cheek pouches to be more scattering than porcine vocal folds ($\ell_{s,eff} \sim 25 \mu\text{m}$ vs. $33 \mu\text{m}$), but they had ~ 3.5 times lower ablation threshold fluence than the porcine vocal folds, an average F_{th} of 0.5 J/cm^2 for cheek pouches vs. 1.75 J/cm^2 for vocal folds. While the scattering lengths were different, the normalized depths presented in Figures. 3.8-3.10 were nearly constant ($z_{ab}/\ell_{s,eff} \sim 2.4$ and 2.7 , for cheek pouches and vocal folds, respectively) considering the different ablation depths. We could therefore conclude that the difference in the ablation threshold fluences was the main factor for the lower incident energies, $E_{th,surface}$, required to ablate hamster cheek pouches (50 – 150 nJ) as compared to those required for porcine vocal folds (250 – 500 nJ) to initiate ablation.

Table 3.1. Summary of tissue optical and mechanical properties and ablation thresholds. Epithelium thickness (z_{ep}), scattering lengths of epithelium ($\ell_{s,ep}$) and superficial lamina propria ($\ell_{s,LP}$), the resultant effective scattering length at the ablation depth ($\ell_{s,eff}$), and tissue specific ablation threshold – TSAT fluence (F_{th}) for each tissue type for 776 nm light and $1/e^2$ focused beam spot diameter of 1.4 μm . The ablation depth for vocal folds was 90 μm and for cheek pouches was 60 μm . The last columns summarize the observed trends for the content of elastin and collagen fibers of each tissue type with their interpreted stiffness and tensile strengths.

Tissue Type	z_{ep} (μm)	$\ell_{s,ep}$ (μm)	$\ell_{s,LP}$ (μm)	$\ell_{s,eff}$ (μm)	F_{th} (J/cm^2)	Collagen Content	Elastin Content	Stiffness	Tensile Strength
Superior Vocal Fold	36 \pm 3.5	30 \pm 0.3	33 \pm 0.2	31.6 \pm 0.5	1.9 \pm 0.06	Low / Medium	High	+	++++
Inferior Vocal Fold	46 \pm 2.0	30 \pm 0.4	39 \pm 0.3	33.8 \pm 0.6	1.6 \pm 0.06	Medium	Low	++	+++
Healthy Cheek Pouch	44 \pm 2.8	21 \pm 0.3	50 \pm 0.9	24.8 \pm 0.6	0.6 \pm 0.02	High	None	+++	++
Scarred Cheek Pouch	41 \pm 1.0	21 \pm 0.4	40 \pm 0.5	24.7 \pm 0.4	0.4 \pm 0.03	Very High	None	++++	+

The data in Table 3.1 also assist interpreting the lower incident energies required for scarred cheek pouches. In comparing normal and scarred hamster cheek pouch mucosae, surprisingly we found that the scarred samples showed similar scattering properties to normal tissue. Thus, the main reason for lower incident ablation energy threshold in scarred mucosa observed in the previous section could also be related to the TSAT fluence that was about 30% lower than for normal tissue.

Considering the ablation and scattering properties measured in this set of experiments, we plotted the maximum ablation depths that are achievable for a given incident pulse energy for each tissue type in Figure 3.11. For the maximum pulse energy of $1.5 \mu\text{J}$ available in our system, the maximum ablation depth is approximately $5 \ell_{s,eff}$ in cheek pouches and $3.5 \ell_{s,eff}$ in vocal folds for creating partial ablation (where initial bubbles cover 40% of the targeted area). Since the ablation threshold is higher for a more complete ablation, the maximum ablation depth will further decrease. For example, for the ablation of 60 – 80% of the target area, maximum ablation depth may be roughly $4 \ell_{s,eff}$ for cheek pouches and $3 \ell_{s,eff}$ for vocal folds as shown in dashed lines in Figure 3.11. In principle, one could ablate deeper with the availability of larger pulse energies. However, as the pulse energy increases other non-linear phenomena such as self-focusing might initiate and cause out of focus damage in the form of filamentations [120]. We can estimate that self-focusing in scarred cheek pouches might occur when ablating at depths of $\sim 6 - 7 \ell_{s,eff}$ with $\sim 10 \mu\text{J}$ pulse energies using 3 ps NIR laser pulses.

This ablation depth limitation might be overcome by introducing novel techniques such as temporal focusing to reduce the out of focus peak intensities [121, 122]. In simultaneous spatial and temporal focusing, a dispersive element such as a grating is used to spatially separate the spectral components of the ultrafast laser pulse [123]. The resulting pulse is temporally as well as spatially dispersed, resulting in a dramatically reduced peak intensity. Focusing by the objective lens serves to spatially confine the spectrally dispersed beam back to a diffraction-limited spot, thus recombining the spectral pulse components and restoring the ultrafast pulse duration at the focus. The reduced peak power of the pulse during propagation reduces undesirable non-linear effects such as self-focusing and filamentation, thereby improving the maximum ablation depth and axial confinement.

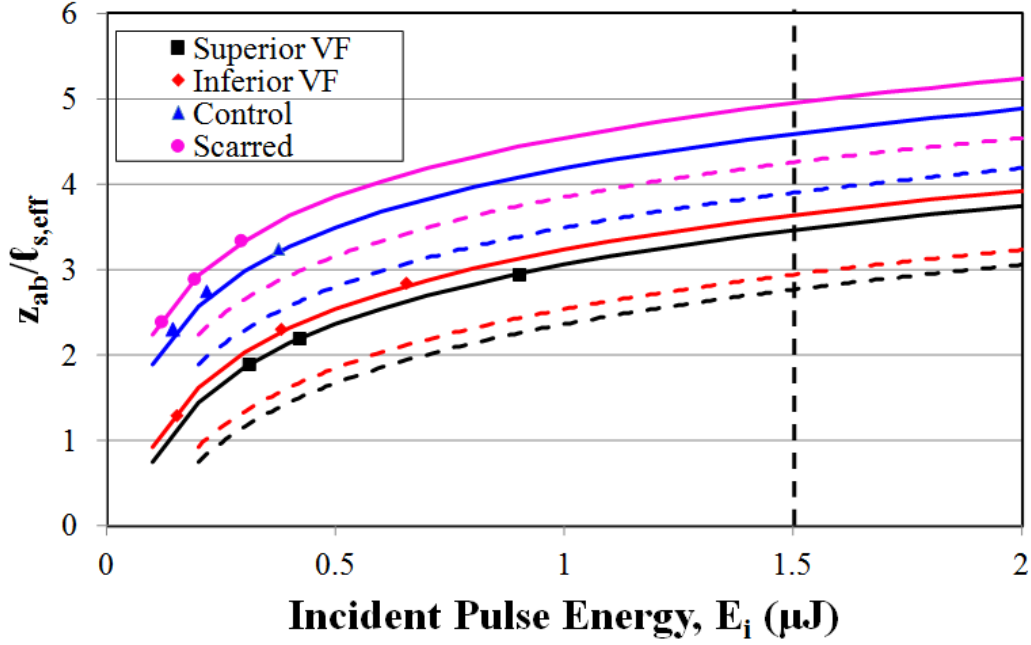


Figure 3.11. Minimum pulse energy at the surface to initiate ablation at different depths and the resultant maximum ablation depth dependence on pulse energy. Three experimental data points for each tissue type and the resultant fits according to Eq. (1) considering the calculated ablation and tissue properties tabulated in Table 3.1. Solid lines represent estimates for the ablation of 40% of the targeted area and dashed lines represent estimates for a more complete ablation of 60-80%. Vertical black dashed line indicates the maximum pulse energy of 1.5 μJ that can be delivered to tissue surface in our setup.

3.3.2.4: Bubble Dynamics in Ablated Voids

In our previous studies, we have found that the initial bubbles formed right after ablation, shrank to a thin layer within 45 minutes. Figure 3.12 shows representative time-lapse images of the side view of such a bubble in porcine vocal fold where the tissue was illuminated from the left side. The images show gradually shrinking bubble as the vaporized tissue diffused out. As the bubble shrinks, it leaves behind a thin layer of ablated void, indicated as a thin layer of dark region in the last nonlinear image.

These bubbles could also be detected with the naked eye after the ablation and used as indicators of successful void creation and presumably for guiding the injection needle. We therefore studied the lifetime of these bubbles for a range of energies for which bubbles covering more than 80% of the targeted area can be created and how they vary between two representative samples. Specifically, we followed volumes of bubbles in two sets of samples for each tissue type whose initial bubble areas were presented in Fig. 3.10.

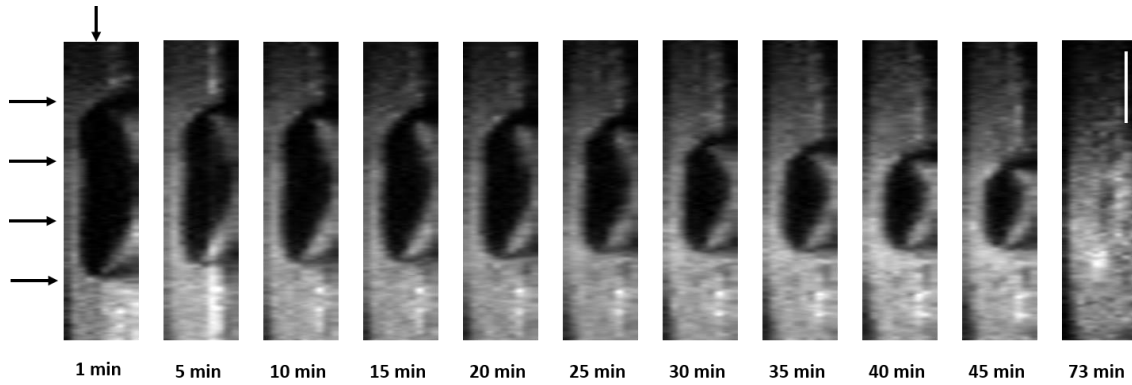


Figure 3.12. Time-lapse side view TPAF images of a bubble in a sub-epithelial void that was created with 750 nJ pulse energy in inferior vocal fold. Multiple arrows on the left side show the direction of the laser beam. The arrow on top shows the axial location of the targeted ablation plane. Scale bar indicates 100 μm .

Figure 3.13 illustrates dynamics of bubble volumes with time. We measured the bubble volume by counting the number of dark pixels in 3D nonlinear images. To correct for the artifact of tissue/gas index of refraction mismatch at the boundaries of the void, the axial dimension of the bubble was downsized by a factor of 1.2 assuming that the bubble had an index of refraction similar to that of air. We note that this correction simply reverses the original focal shift correction made for the air lens when focused within the tissue.

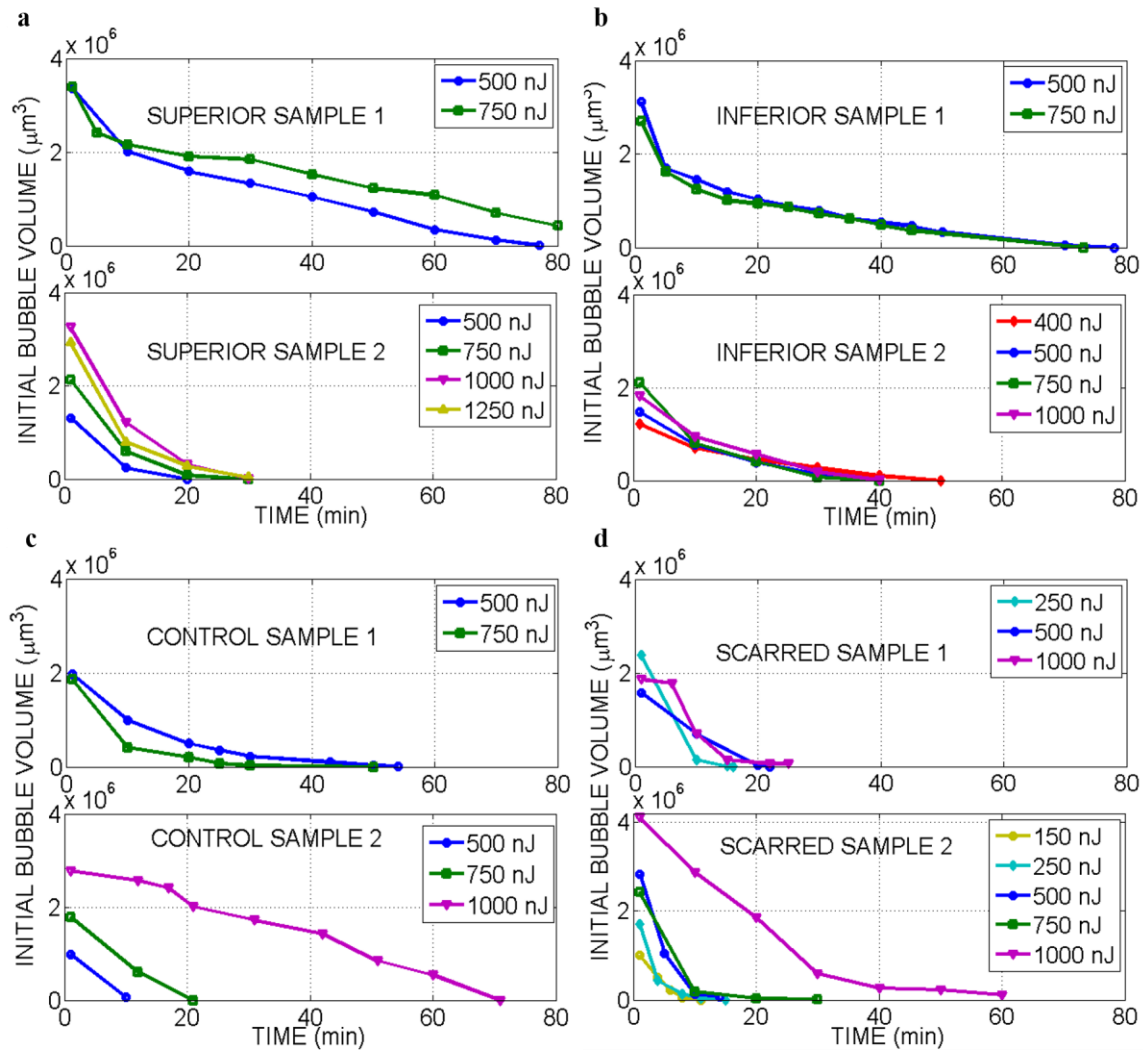


Figure 3.13. Bubble lifetimes for different pulse energies for 2 different samples for each tissue. (a-b) Superior and inferior porcine vocal folds. (c-d) Control and scarred hamster cheek pouches. Solid lines represent sample 1 and dashed lines represent sample 2.

The bubble lifetimes were generally consistent within a sample but varied between the two samples. For example, in the first porcine samples, the bubble lifetimes in both superior and inferior vocal folds were between 80-100 min. In the second sample, their lifetime dropped to 30-40 min, highlighting sample-to-sample variability. In a given

sample, the bubble lifetime did not change significantly with incident pulse energy even if their initial volume did.

In the hamster cheek pouches, the lifetime of bubbles in both control and scarred tissue were shorter than porcine samples while the biggest drop was observed for the scarred tissue. Although the initial volumes of bubbles were, in general, larger in scarred cheek pouches than in the control, they lasted a shorter time on the average. As will be discussed in detail in the discussion section, shorter lifetime of bubbles can likely be attributed to higher compression imposed by the dense and stiffened mechanical structure of scarred tissue.

Overall bubble lifetime did not change within a sample significantly with the incident pulse energy but showed sample-to-sample variability. While the bubbles had the shortest lifetime (10-20 mins) for scarred tissue, they might still provide enough time for verifying the creation of voids and guiding the injection of biomaterials.

3.4: DISCUSSION AND CONCLUSIONS

The primary goal of this work was to study laser ablation parameters for creation of sub-epithelial voids in vocal folds and how these parameters varied in scar tissue using animal models. We specifically investigated the differences in tissue architecture and scattering properties, and their relation to ablation thresholds and bubble lifetime. By using nonlinear imaging we analyzed tissue architecture and bubble dynamics. By developing a new method, we measured the ablation threshold below tissue surface while simultaneously extracting the extinction properties of different tissue layers. In this section, we will discuss how the mechanical properties as interpreted from the nonlinear images could be related to the observed differences in the ablation characteristics and bubble lifetime.

3.4.1: Mechanical Properties of Tissue

Nonlinear images provided valuable information on the architecture of LP in different tissues, shedding light on their stiffness and elasticity properties. We observed a predominance of collagen fibers (TPAF+SHG) in the inferior porcine vocal folds, while the density of elastin (TPAF) and collagen fibers (SHG) appeared roughly equal in the superior folds. On the other hand, the hamster cheek pouch samples showed only SHG signal below the epithelium, indicating a collagenous extracellular matrix, which increases in density with scarring.

The collagen content of tissue defines its mechanical stiffness which is directly proportional to the shear elastic modulus. In general, the elastic modulus of collagen is a couple of orders of magnitude greater than that of elastin [124]. In addition, a 3 fold increase in the shear elastic modulus has been found for scarred samples compared to normal ones [125]. Therefore, hamster cheek pouches having mostly collagen and no elastin are expected to be stiffer than the vocal folds, and scarring of cheek pouches is expected to increase in stiffness further due to their increased collagen density.

In addition to being stiffer, collagen fibers also possess a higher tensile strength than elastin and can theoretically withstand much higher stresses in comparison to elastin. However, the extra cellular matrix that is composed of both collagen and elastin, referred as a "two-phase" material, can provide even higher overall tensile strength than that of collagen alone. Elastin in two-phase material can distribute the stressing forces uniformly and thus transfer stresses at flaws to other parts of the system. The uniform distribution of stresses across the system prevents the extension of structural defects and permits the tensile strength of the collagen to approach the theoretical value [124]. In an opposite trend to the stiffness, this analysis points that cheek pouches potentially possess a lower tensile strength compared to vocal folds.

The ability of a collagen matrix to withstand high stress levels is related to its concentration as well as fibril diameter [126]. While a clear correlation between the tensile strength and collagen concentration has been shown [124], scarring is not simply an increase in collagen content, but it is a wound healing process. In the process of wound healing, although collagen content increases, the new fibrils, filling in defects, is not as thick as those in normal tissue. Morphologically, the diameters of collagen in a scarred tissue have been observed to be less than that observed in normal tissue [127]. Furthermore, the collagen matrix in the scarred area is poorly reconstituted, in dense parallel fibers, unlike the mechanically efficient basket-weave meshwork of collagen in healthy tissue [128]. Therefore, the tensile strength of the scar tissue only reaches 70 – 80 % of that of a normal skin and is not fully restored [127].

These mechanical properties of biological tissues are of great importance that could potentially determine the dynamics of the ablation process and bubble lifetime [27, 129]. To guide our discussion below, we summarized the observed trends for the content of elastin and collagen fibers of each tissue type with their interpreted stiffness and tensile strengths in Table 3.1.

3.4.2: The Effect of Mechanical Properties of Tissue on Bubble Dynamics

When the ablation occurs within a confined volume below the surface, as in our experiments, the gaseous ablated tissue is confined within a bubble. These bubbles can initially expand slightly beyond the scanned area laterally (in the current study $250 \times 250 \mu\text{m}^2$) and up to $100 \mu\text{m}$ axially. As the gas slowly diffuses out, the initial bubble shrinks and eventually becomes a thin permanent void.

The dynamics of bubble formation depends on the stiffness of media in which bubbles are generated. Recent vocal fold studies [12, 125, 130] report a higher stiffness

of scarred tissues because of their higher shear elastic modulus and dynamic viscosity. A force balance at the bubble wall reveals that the stiffness of the surrounding tissue aids surface tension in resisting and thus dissipating energy for bubble growth during bubble expansion, thereby reducing maximum bubble radius. On the other hand, during bubble collapse, tissue stiffness aids the bubbles to shrink faster. Since the scarred tissues are expected to be stiffer, as discussed above, higher tension on the slowly shrinking bubble will help it to collapse faster than the less stiff normal tissue. In conclusion, shorter bubble lifetimes of scarred tissue observed in our experiments can be associated with their increased stiffness.

3.4.3: The Effect of Mechanical Properties and Impurities on Ablation Threshold

The ablation threshold results revealed, in average, a 3.5 times smaller threshold fluence for cheek pouches (average $\sim 0.5 \text{ J/cm}^2$) than vocal folds (average $\sim 1.75 \text{ J/cm}^2$). Interestingly, the scarred cheek pouches showed a further 30% lower ablation threshold fluence (0.4 J/cm^2) than the healthy cheek pouches (0.6 J/cm^2). The reduced ablation thresholds for scar tissue may be useful if this selectivity can be exploited in clinical applications.

As discussed in the introduction, TSAT can be influenced by tissue mechanical properties, the amount of initial seed electrons due to impurities, and linear absorption. We first consider the effect of the mechanical properties of different tissues in terms of their stiffness and tensile strength by referring to the summary in Table 3.1. The optical breakdown can create shock waves and when the strength of the pressure across the shock wave exceeds the tensile strength of the tissue, it may cause to further damage by a tearing/rapturing mechanism. Therefore, tissue with a higher tensile strength is expected to have a higher ablation threshold. The results clearly indicate a direct correlation

between the tensile strength of tissue and the ablation threshold. The higher the content of elastin in the collagen/elastin system, the higher the tensile strength and thus the ablation threshold. The observations of lower damage fluence for scarred cheek pouches with respect to control tissue are also in accordance with their lower tensile strengths as result of wound healing process discussed above.

To understand the effect of the initial seed electrons, we have simulated free electron generation in water for varying initial free electron densities. Considering both multi-photon and cascade ionizations [27, 33, 35] and assuming that the optical breakdown occurs when a critical electron density of 10^{21} cm^{-3} is reached, we could estimate the threshold intensity for a 3 ps laser pulse. At the minimum possible electron density of 10^{12} cm^{-3} that corresponds to the existence of a single electron in the focal volume, we found that the threshold for optical breakdown remained similar to the threshold in the absence of seed electrons. In the presence of a larger number of seed electrons (10 electrons per volume – 10^{13} cm^{-3}), there was only a slight decrease (10 %) in the threshold. It is possible that the scarring creates additional free electrons, possibly leading to slight threshold reduction discussed above. However, it is not clear how much the scarring might change the number of seed electrons and whether or not it leads to any possible linear absorption. Therefore, we conclude that the main mechanism for the differences in the TSAT fluences might be related to the mechanical properties of tissue, mainly to its tensile strength.

In conclusion, ablation with moderate repetition rate (<1 MHz) ultrashort laser pulses of 3 ps, resulted in precise and repeatable cutting of tissue and was confined within the focal volume with no collateral damage observable in the histology images. The existence of long-lasting bubbles should provide ample time for monitoring the completeness of ablation and guiding the surgeon better to the injection site, as verified in

our recent studies [131]. We have successfully demonstrated localization of a polyethylene glycol based biomaterial inside the ablated sub-epithelial voids in a scarred hamster cheek pouch. Our attempts on injecting without priorly created sub-epithelial voids resulted in back-flow of the biomaterial along the point of injection. In contrast, the presence of sub-epithelial voids created at 90 μm below the tissue surface provided the space for the biomaterial that greatly reduced back-flow at the injection site and resulted in a lasting localization of the injection material.

The ablation characterization efforts presented in this chapter will guide development of an ultrafast laser-assisted method to reduce injection pressures in the scarred vocal folds while improving localization of injected biomaterials. We are currently developing a new generation endoscope suitable for in vivo micro-laryngoscopic testing in large animal models.

Chapter 4: Tripling the Maximum Imaging Depth with Third-Harmonic Generation Microscopy²

4.1: INTRODUCTION

Multi-photon nonlinear imaging microscopies can perform noninvasive and three-dimensional deep tissue imaging with subcellular resolution using tightly focused femtosecond pulses. They provide better axial resolution and improved signal to background ratios than standard laser scanning fluorescence microscopy [50, 132, 133]. Specifically, two-photon microscopy (TPM) with near infrared (NIR) excitation is advantageous for deep tissue imaging because (i) NIR light can excite natural fluorophores in tissue, (ii) intrinsic three-dimensional sectioning is possible with the confined fluorescence generation in the focal volume, and (iii) imaging resolution is negligibly degraded from scattering because fluorescence generation in the focal volume is dominated by ballistic photons [62, 102, 134]. Unfortunately, this technique still has several limitations when it comes to deep tissue imaging, including potential in-focus cell damage and multi-photon photo-toxicity due to high optical intensities [135, 136]. Crucially, there is a fundamental limit to the maximum imaging depth due to gradually increasing out-of-focus (background) fluorescence signal when increasing imaging depth to compensate for the losses due to scattering. Thus, the maximum imaging depth reaches a fundamental limit, when the background generated close to the surface equals the signal arising from the focal volume. This maximum imaging depth was found to be dependent on the tissue optical properties as well as its homogeneity [102]. Several studies showed

² Yildirim Murat, Nicholas Durr, and Adela Ben-Yakar. "Tripling the maximum imaging depth with third-harmonic generation microscopy." *Journal of biomedical optics* (2015), accepted for publication.

Murat Yildirim designed and performed the experiments, and heat simulations. Nicholas Durr helped for Monte-Carlo simulations. Adela Ben-Yakar supervised the project.

that the maximum imaging depth for TPM around 800 nm excitation wavelengths is restricted to 3-5 scattering lengths depending on tissue types [54, 62, 102, 134, 137].

In recent years, there have been very promising studies to enhance the maximum imaging depth for multi-photon microscopy techniques. For example, the TPM maximum imaging depth was increased 1.4 times by performing multi-photon activation of photo-activable fluorophores (PAF) in tissue phantoms labeled with either a synthetic caged fluorescein dye or genetically encodable PAFs [138]. In this study, multiphoton activation switched on a higher percentage of PAFs at the focus than those out-of-focus which were originally in the dark state. Then, another multiphoton activation was performed to bring these bright state PAFs to fluorescent state which happened at a higher possibility at the focus leading to a significantly reduced background fluorescence. Another study related to reducing background fluorescence signal introduced the theoretical analysis and numerical simulations to switch the two photon excited fluorescence on and off at the focus by using stimulated emission reduced fluorescence (SERF) microscopy [139]. In this study, they combined continuous wave stimulated emission (SE) beam collinearly with two-photon excitation beam and detected both fluorescence signals generated with and without SE. By subtracting the fluorescence signal without SE from that of with SE they could obtain the fluorescence signal mainly generated in the focus. Consequently, they estimated this technique could potentially achieve 1.8 times higher imaging depth compared to original two-photon fluorescence imaging in brain tissues. In another study, implementing TPM at a longer excitation wavelength with fluorescently labeled blood vessels in mouse brain led to a demonstrable two fold improvement in maximum imaging depth compared to shorter excitation wavelengths [140]. More recently, *in vivo* three-photon microscopy in a mouse brain at 1700 nm wavelength was shown to enhance the maximum imaging depth by a factor of

1.8 compared to two-photon microscopy at 800 nm [141]. This imaging depth improvement occurred due to two reasons: increase in extinction length due to increase in excitation wavelength and the reduced probability of three-photon absorption in the out-of-focus region.

Improving maximum imaging depth by using a longer excitation wavelength and a three-photon process can also be achieved by utilizing other nonlinear imaging techniques such as second- and third-harmonic generation microscopies. These techniques in principle deposit no energy on the tissue sample and thus reduce the probability of photo-toxicity [142, 143]. Second-harmonic generation (SHG) necessitates intense femtosecond laser pulses passing through a highly polarizable material with a non-centrosymmetric molecular organization like collagen fibers [142]. Third-harmonic generation (THG) on the other hand can apply to all molecules wherein three photons at the fundamental frequency are converted to a photon at the third harmonic frequency. The signal intensity in THG is very sensitive to index of refraction and third order susceptibility ($\chi^{(3)}$) changes [144, 145]. Previous related research has shown different applications of THG, like imaging neurons and their processes [143, 146], lipid bodies in plant seeds and *Drosophila* embryos [147], zebrafish embryo and larvae [148, 149], cardiomyocytes [150], elastin and collagen fibers [151, 152], malaria parasites [153], myelin in the vertebrate central nervous system [154], and human cornea [155]. The use of endogenous THG for imaging is critical in applications where the external fluorophores may be deemed invasive and toxic. Thanks to the reduced probability of three-photon absorption in the out-of-focus volume, reduced scattering probability of longer excitation wavelength, and no energy deposition on the sample, THG microscopy can also improve the maximum imaging depth in turbid tissues remarkably. While THG microscopy has been shown to image the whole thickness of the transparent zebrafish

embryo [148] and external capsule of mouse brain around 900 μm depth [141], highly scattering tissue samples such as hamster cheek pouch [156], fixed human [157], murine muscles [158], and mouse skin [151] could only be imaged between 100-300 μm .

The aim of this chapter is to evaluate the improvement in maximum imaging depth in a highly scattering tissue using THG microscopy at 1552 nm excitation wavelength as compared to TPM at 776 nm wavelength with a turnkey femtosecond fiber laser. The frequency doubled femtosecond laser pulses can also be tightly focused to create precise sub-surface cuts inside the tissue at substantially higher energies. Having short pulse durations and high peak intensities, femtosecond lasers ensure the use of minimal energies for high-precision ablation with minimal collateral damage to the surrounding tissue. Therefore, the combined nonlinear imaging and precise microsurgery capabilities of femtosecond lasers would make them ideal for image-guided laser surgery in clinical applications. However, combining these unique capabilities of femtosecond pulses in a single laser has been a challenge until the advent of the femtosecond fiber lasers. Femtosecond fiber lasers can provide a repetition rate high enough for nonlinear imaging, and an adequate pulse energy for microsurgery [159, 160]. Our group has pioneered the use of femtosecond fiber lasers in performing deep tissue microsurgery guided by nonlinear imaging for the treatment of vocal fold scarring [13, 54].

The clinical challenge that we address in our studies is related to vocal fold scarring. This is one of the major causes of voice disorders and may arise from overuse or post-surgical wound healing. One promising treatment uses the injection of soft biomaterials aimed at restoring viscoelasticity of the outermost vibratory layer of the vocal fold, superficial lamina propria (SLP). A common unsolved problem facing the surgical use of injectable materials is its accurate and effective placement in a superficial plane in scarred vocal folds [6]. In recent experiments, we successfully achieved

biomaterial localization by ablating such sub-epithelial voids approximately 100 μm deep in the SLP of a porcine vocal fold [131]. However, our maximum imaging depth was limited to between 100 and 150 μm deep in the tissue with two-photon autofluorescence and SHG microscopies. To guide such a high-precision microsurgery in different layers of SLP, there is a need for high-resolution imaging deep inside the vocal folds for both locating the scarred tissue and assessing the efficacy of ablation below the epithelium.

This chapter presents results from *ex vivo* porcine vocal fold deep tissue imaging experiments to enable reaching the maximum theoretical imaging depth possible using THG at 1552 nm and improve it substantially compared to TPM at 776 nm wavelengths. Based on a novel ablation-based method we previously developed, we first measure tissue optical properties [54]. Using these optical properties, we then perform analytical and Monte-Carlo modeling of maximum imaging depths that can be obtained with these nonlinear imaging modalities. More importantly, to avoid tissue heating during deep tissue imaging, we analyze the heating properties of tissue and estimate the depth-resolved temperature distribution by utilizing numerical and experimental techniques. Overall, this chapter illustrates how THG microscopy at 1552 nm excitation wavelength can be used as a new imaging modality to perform deep tissue imaging in highly turbid tissue, like scarred vocal folds, with the capability to guide our precise laser microsurgery method.

4.2: METHODS AND MATERIALS

4.2.1: Experimental Setup

We used our home-built, inverted laser-scanning microscope to perform TPM and THG microscopies (Fig. 4.1a). The excitation laser was a femtosecond Er-doped fiber laser (Discovery, Raydiance Inc.) with 3W average power at 1552 nm (1.5 μJ pulse

energy) and 1 W when frequency doubled to 776 nm (0.5 μ J pulse energy) at 2 MHz with 600 fs pulse width. We focused the laser beam with a 0.75-NA, 20 \times air objective (Nikon Plan Apo). We measured the spot size by imaging 100 nm polystyrene beads (Invitrogen, F8803) embedded in agar gel at depths varying from 50 to 500 μ m. The agar-bead phantom consisted of 10 μ l of the stock bead solution (2 % solids) dispersed in 2 ml of 4% agar in water, which is then allowed to gel. This protocol resulted in a bead concentration of 2×10^{10} beads/ml which provided a 35- μ m scattering length at 776-nm excitation wavelength. This scattering length is in the range of effective scattering lengths expected from the lamina propria of our sample. The average lateral full width half maximum (FWHM) of the two-photon point spread function (PSF) was 0.58 ± 0.07 μ m and three-photon FWHM of the PSF was 0.95 ± 0.11 μ m. In order to satisfy the Nyquist criterion, we chose a pixel size with less than half of the resolution of both imaging modalities. Since the resolution of TPM (0.6 μ m) is better than the resolution of THG (0.9 μ m), we choose our field of view (150×150 μ m²) having a 0.3 μ m pixel size in both directions. We scanned the laser beam in the x and y-axes using a pair of the galvanometric mirrors (Cambridge Technologies, Inc.), and swept the focal spot over a 150×150 μ m² field of view for 3.3 s. The number of pixels (512 in both axes) corresponded to 2.3 pulses/pixel/raw image for both TPM THG imaging. We collected 10 images at each plane and averaged them together. We used a dichroic mirror (Semrock, FF735-Di01) to transmit the excitation light to the sample and reflect the emitted signal from the sample to the collection optics. A photo-multiplier tube (PMT) (Hamamatsu, H10770 PA-40) collected the signal via collection optics, laser blocking filters (Edmund Optics, 84-650 for THG imaging, or Semrock, FF01-750/SP-25 for TPM imaging) and laser transmission filters (Chroma, HQ515/15M for THG imaging, Schott, BG38 for

TPM imaging). The computer software (MPScan) reconstructed these signals into 512×512 pixel images at a frame rate of 3.05 Hz [161].

We characterized the order of nonlinear processes by measuring the detected signal on the PMT while increasing imaging power on the sample. As shown in Fig. 4.1b, the slope of the PMT signal vs. imaging power curve yielded 3.02 ± 0.12 and 2.05 ± 0.08 on a log-log scale for THG and TPM, respectively. As expected, these results confirmed that THG and TPM imaging were second- and third-order nonlinear processes.

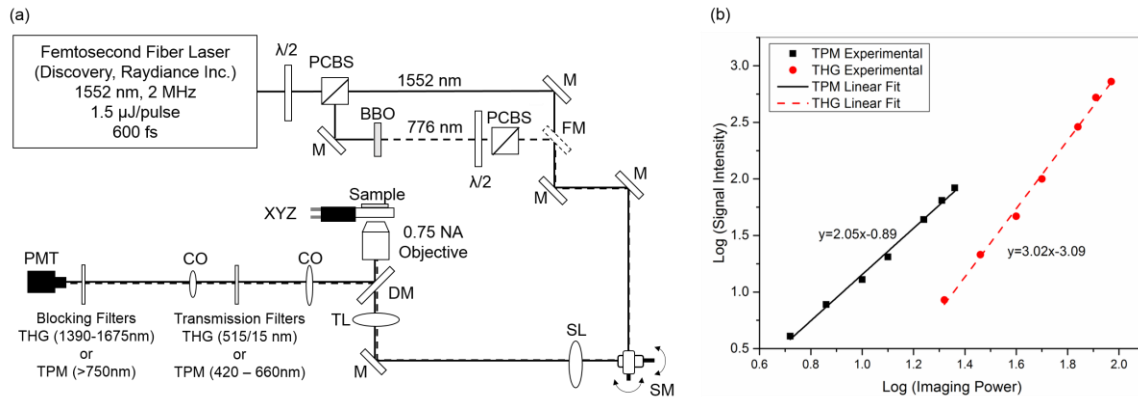


Figure 4.1. Schematic of the inverted microscope system for nonlinear imaging and ablation. (a) Femtosecond laser pulses were obtained from a compact fiber laser system at the fundamental wavelength (1552 nm) and passed through an energy attenuator consisting of a half-wave plate ($\lambda/2$) and polarizing cube beam splitter (PCBS). Frequency doubled pulses (776 nm) were achieved using a BBO crystal. Both beams were scanned by a pair of galvanometric scanning mirrors (SM), which was then imaged on the back aperture of a 0.75-NA, 20 \times objective by a pair of a scan lens (SL) and a tube lens (TL). The samples were placed on a three-axis motorized stage (P280, Nanocube, PI) for nonlinear imaging. Emitted light (either TPM or THG) was collected by a dichroic mirror (DM), collection optics (CO), laser blocking filters (Edmund Optics, 84-650 for THG imaging, or Semrock, FF01-750/SP-25 for TPM imaging), and imaging specific either THG filter (Chroma, HQ515/15M) or TPM filter (Schott, BG38) into the photomultiplier tube (PMT) (H10770 PA-40, Hamamatsu). (b) The slopes of signal intensities versus imaging power verified the degree of nonlinear processes for both TPM and THG imaging on a log-log scale plot.

4.2.2: Ex vivo Tissue Preparation

The lamina propria (LP) of porcine vocal folds has been previously studied and was found to be most similar to the human LP in terms of their elastin and collagen distribution [103, 105]. Our previous study also showed that superior porcine vocal folds have a fiber structure similar to human vocal folds as compared to inferior porcine vocal folds at the depths we are interested in [54]. Thus, we decided to use freshly excised superior porcine vocal folds in our experiments. We acquired fresh porcine airway specimens from a local slaughter house and isolated the larynx in a room temperature saline bath within 2 hours of sacrificing the animal. After excision, we placed the vocal folds in saline solution and covered them with a glass cover slip to flatten their upper surface. In a clinical application, the glass cover slip would be akin to the window of a microsurgery probe in contact with the sample, thus maintaining a constant depth of ablation. Short-lived autofluorescence of fresh tissue samples and fluorescence beads helped identifying the surface of the sample during TPM imaging. For THG imaging, high contrast at the air and glass interface allowed us to identify the tissue surface easily.

4.3: RESULTS

4.3.1: Extinction Properties of Tissue

To determine extinction properties of fresh porcine vocal folds at both excitation wavelengths (776 nm and 1552 nm), we used a novel ablation-based method that we developed in our recent work [54]. In this method, we perform ablations at three different depths below the epithelium in the SLP (72, 90, and 108 μm) and find the minimum pulse energy required to initiate ablation ($E_{th,surface}$) at each depth. For these ablation measurements we use the laser at 303 kHz repetition rate. To find the extinction

properties of the two layers, we obtain three equations by applying Beer's law for each ablation experiment:

$$F_{th} = \frac{E_{th,surface}}{\pi w^2} \cdot \exp\left(\frac{-z_{ep}}{\ell_{ext,ep}}\right) \cdot \exp\left(-\left[\frac{z_{ab}-z_{ep}}{\ell_{ext,LP}}\right]\right) \quad (1)$$

$$F_{th} = \frac{E_{th,surface}}{\pi w^2} \cdot \exp\left(\frac{-z_{ep}}{\ell_{ext,ep}} - \frac{z_{ab}-z_{ep}}{\ell_{ext,LP}}\right) = \frac{E_{th,surface}}{\pi w^2} \cdot \exp\left(-\frac{z_{ab}}{\ell_{ext}}\right) \quad (2)$$

where F_{th} is the unknown ablation threshold fluence of SLP, $E_{th,surface}$ is the measured pulse energy at the tissue surface, w is the $1/e^2$ measured radius of the laser beam at the focal plane, z_{ep} is the epithelium thickness that can be measured from nonlinear images, z_{ab} is the chosen ablation depth, $\ell_{ext,ep}$ is the unknown epithelium extinction length, and $\ell_{ext,LP}$ is the unknown SLP extinction length. By solving three equations, we can then determine the three unknowns: $\ell_{ext,ep}$, $\ell_{ext,LP}$, and F_{th} . The effective extinction length of tissue, ℓ_{ext} at the maximum imaging depth, z_m can then be deduced from Eq. 2 by replacing z_{ab} with z_m as follows:

$$\ell_{ext} = \frac{z_m \cdot \ell_{ext,ep} \cdot \ell_{ext,LP}}{z_{ep} \cdot \ell_{ext,LP} + (z_m - z_{ep}) \cdot \ell_{ext,ep}} \quad (3)$$

For 776 nm excitation wavelength, the tissue extinction length is equal to the scattering length because of the negligible tissue absorption. However, the absorption is considerable at 1552 nm. To identify the scattering and absorption components of the extinction length at 1552 nm, we estimated the scattering length using the following empirical correlation for fibrous soft tissues [162]:

$$\ell_{sca,\lambda_2} = \ell_{sca,\lambda_1} \left(\frac{\lambda_2}{\lambda_1}\right)^{1.627 \pm 0.115} \quad (4)$$

The resulting scattering length was $108 \pm 8 \mu\text{m}$ at 1552 nm wavelength according to Eq. 3 and the absorption length could then be deduced as $135 \pm 15 \mu\text{m}$. Several studies have found that the absorption length in pure water is around 200-250 μm at 1552 nm wavelength [163, 164]. In addition to these studies, we performed a 3-depth ablation experiment until the observation of bubble formation with THG imaging at 303 kHz repetition rate to determine the absorption length at 1552 nm wavelength. This experiment revealed an absorption length of $200 \pm 50 \mu\text{m}$. Thus, we believe that our tissue experimental results correlated very well with water absorption results and we can attribute the small difference in absorption length between water and vocal folds to the absorption lengths of vocal fold constituents such as collagen, elastin, and hyaluronic acid. We used these values in our Monte Carlo and heat transfer simulations. The summary of all extinction lengths, which were generally in agreement with the values reported in the literature [162, 165] for both excitation wavelengths, are tabulated in Table 4.1.

Table 4.1. Summary of measured tissue optical properties at 776 and 1552 nm excitation wavelengths. Extinction lengths for epithelium ($\ell_{\text{ext,ep}}$) and lamina propria ($\ell_{\text{ext,LP}}$) at the maximum imaging depths for two-photon and third harmonic generation imaging in the corresponding wavelengths. The effective scattering (ℓ_{sca}) and absorption lengths ($\ell_{\text{sca,eff}}$) at the maximum imaging depths (z_m) are also tabulated.

λ_{exc} (nm)	z_{ep} (μm)	$\ell_{\text{ext,ep}}$ (μm)	$\ell_{\text{ext,LP}}$ (μm)	z_m (μm)	ℓ_{ext} (μm)	ℓ_{sca} (μm)	ℓ_{abs} (μm)
776	60 ± 6	33 ± 3.2	37 ± 3.5	140 ± 6	35 ± 2.4	35 ± 2.4	$\sim 10^5 \pm 10^4$
1552	60 ± 6	44 ± 4.8	67 ± 7.1	420 ± 6	60 ± 3.9	108 ± 8	135 ± 15

4.3.2: Maximum Imaging Depth

We imaged an excised fresh superior porcine vocal fold using both TPM and THG imaging modalities to compare their maximum imaging depths at 776 and 1552 nm excitation wavelengths, respectively (Fig. 4.2). The tissue surface was identified by the presence of externally applied fluorescent beads in TPM and the presence of large signal contrast at the interface between the tissue surface and the glass cover in THG. The depth at which collagen fibers first appeared varied between the locations of imaging, ranging from 40 to 70 μm below the surface. As the imaging depth was increased, we detected TPM and THG signals originating from different tissue components, which helped to differentiate epithelium and superficial lamina propria (SLP). For instance, TPM at 776 nm excitation wavelength could detect, NAD(P)H, and flavins in the epithelium [50] and collagen and elastin fibers in the SLP [98, 99] (Fig. 4.2b). On the other hand, THG enabled us to image epithelial cells and ECM fibers in superior porcine vocal folds. The THG signal originated from the index of refraction changes, geometric shape of scatterers, and third order susceptibility differences inside the tissue (Fig. 4.2a). Comparison between the nonlinear images of a superior porcine vocal fold clearly showed that THG at a longer wavelength (1552 nm) qualitatively improved the maximum imaging depth substantially. At the maximal imaging depths, the applied maximum imaging power was 10 and 55 mW for TPM and THG, respectively.

To quantitatively analyze the maximum imaging depths, we analyzed how the signal-to-background ratio (SBR) varied with imaging depth (Fig. 4.3). We calculated the SBR

by selecting a line of pixels across resolvable features at different locations in each image using Image J software. These resolvable features were either epithelial cells in the epithelium or extracellular matrix (ECM) fibers in the SLP. Then, we calculated the ratio of maximum signal intensity to the average of 10 pixels on the right and left tail of the $1/e^2$ of the maximum signal intensity. The SBR for each imaging modality is presented with respect to the imaging depth on a semi-log plot in Fig. 4.3a. The maximum imaging depth, z_m , was defined as the depth where the SBR fell to one. In addition, we plotted SBR against imaging depth normalized with tissue extinction length, z_{ext} (Fig. 4.3b).

Figure 4.3a quantitatively shows that THG imaging provided three times deeper imaging, increasing the imaging depth from 140 μm (TPM at 776 nm) to 420 μm (THG at 1552 nm). Figure 4.3b also shows that SBR became one at normalized imaging depths of approximately four and seven extinction lengths for the TPM and THG imaging modalities, respectively. Such improvement of non-dimensional depths (~ 1.7 times) was a direct result of the reduced probability for out-of-focus generation in three-photon process as well as the reduced absorption of the signal generated at longer wavelengths. Overall, both longer excitation and emission wavelengths and three-photon processes had improved the maximum imaging depth for THG microscopy at 1552 nm excitation wavelength. This maximum imaging depth improvement reveals a potential application in imaging scarred human vocal folds, which have thicker epithelium compared to porcine vocal folds.

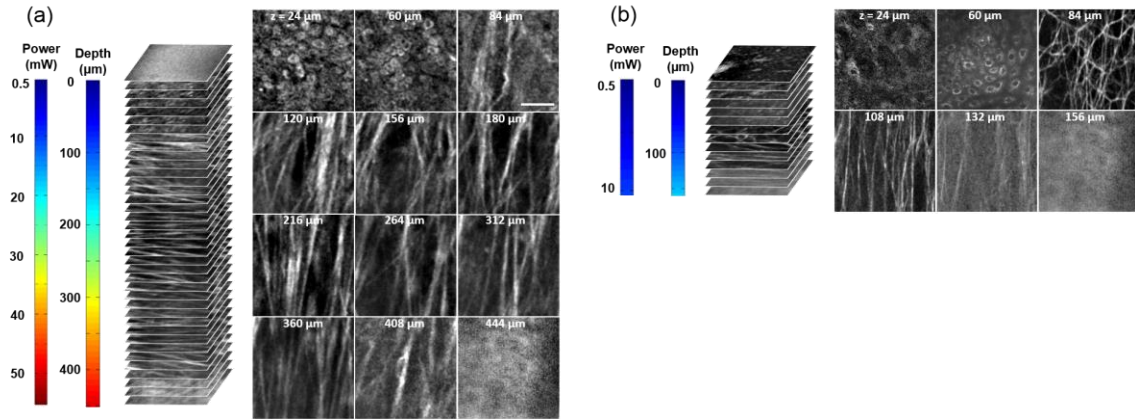


Figure 4.2. Representative nonlinear optical images of a fresh superior porcine vocal fold. (a) Images of THG showing clear collagen features beyond 400 μm using imaging powers in the range of 50 mW. (b) Images of combined TPM and SHG indicating maximum imaging depths limited to below 150 μm . The scale bar represents 50 μm .

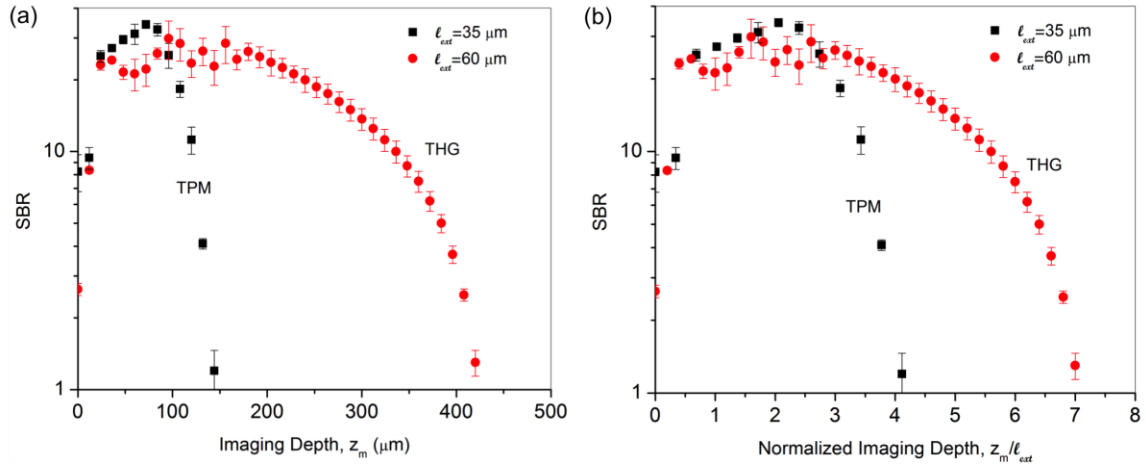


Figure 4.3. Signal to background ratio (SBR) values for both nonlinear imaging modalities. (a) SBR with respect to imaging depth, z_m . (b) SBR with respect to normalized imaging depth, z_m / ℓ_{ext} .

4.3.3: Analytical and Monte-Carlo Modeling of Maximum Imaging Depths

To model the maximum imaging depths, we utilized analytical and Monte-Carlo methods used previously by our group for varying extinction lengths and inhomogeneities (χ) [102]. Assuming the concentration of fluorophores within focal

volume is constant, C_s , and that the out of focus fluorophore concentration is diffuse enough to be approximated by the average fluorophore concentration, C_b , we defined the staining inhomogeneity, χ , as the ratio of C_s and C_b . As we explained in details in our previous publication [102], we added 0, 4, 10 and 25 μM concentration of fluorescein (Fluka 46955) into low melting point agarose (1%, Sigma), polystyrene beads (Invitrogen) to control the staining χ of tissue phantoms. These fluorescein concentrations resulted in χ values of 10, 25, 62, and 300 [102]. We adapted the analytical method developed by Theer and Denk [62] to calculate the ballistic and scattered light distributions in turbid media, which were then combined to obtain the total fluorescence distribution with depth. The intensity for ballistic photons was assumed to have Gaussian spatial and temporal distributions. Monte-Carlo simulations were used to simulate photon transport in the tissue with an anisotropy factor of $g = 0.85$ by separately modeling the excitation and emission phenomena. Simulations calculated the spatiotemporal distribution of the intensities (I^2 and I^3) and the spatial dependence of collection efficiency. The image contrast could then be calculated as the ratio of the signal in the focal volume to the background. The imaging depth was found at the depth where the image contrast fell to one. In the case of THG, the emitted photons were directed forward, unlike the two-photon autofluorescence process where emission was assumed to be isotropic [166, 167]. Also, the background signal in THG depends on the interference between harmonics generated at different depths of the sample. To calculate this interference, we calculated both focus and far field radiation using a chirp z-transform. This transform is based on Green-function approach and is calculated using fast Fourier

transforms. The chirp z-transform technique has been previously shown to model SHG imaging of collagen fibers and THG imaging of interfaces and multilayer structures [168, 169].

Figure 4.4 presents the results from Monte-Carlo simulations and analytical calculations for different extinction lengths. For TPM imaging, normalized imaging depth had a logarithmic dependence on extinction length, as expected according to the Beer-Lambert's law (Fig. 4.4a). Monte-Carlo simulations correlated well with the analytical calculations. Normalized imaging depth was estimated to be between 4 – 5 extinction lengths for the inhomogeneity (χ) range of 25 – 62 for the range of the measured tissue scattering (which is equal to extinction since absorption is minimal at 776 nm) lengths. These calculations were consistent with the experimental results shown in dashed circular box in Fig. 4.4a.

Similar to the TPM case, normalized maximum imaging depth in THG microscopy also exhibited a logarithmic dependence on extinction length and increased with the increase in inhomogeneity for all extinction lengths (Fig. 4.4b). The measured extinction length in our experiments was 60 μm and the corresponding maximum imaging depth was estimated to be in the range of 7.0 extinction lengths that matched well the simulated results for the inhomogeneity (χ) range of 25 – 62 similar to the TPM results. Another important conclusion drawn from Fig. 4.4b was that THG microscopy improved maximum imaging depth approximately two times compared to TPM microscopy at the same extinction lengths for all inhomogeneity values. This conclusion could be attributed

to the effect of three-photon processes on reducing background signal and thus increasing SBR value.

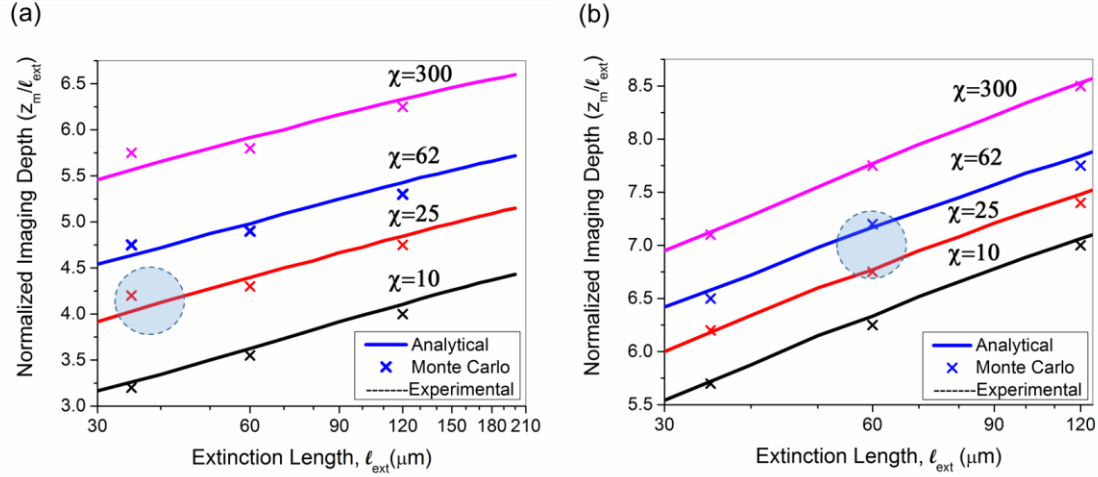


Figure 4.4. Analytical and numerical modeling of maximum imaging depths. (a) For TPM at 776 nm excitation and 515 nm emission wavelengths. (b) For THG at 1550 nm excitation and 515 nm emission wavelengths. The maximum imaging depths were calculated as a function of the effective extinction length (ℓ_{ext}) and for different tissue inhomogeneities (χ). The extinction length varied for different scattering lengths representing different tissue types and assuming a negligible absorption length at 776 nm and $\ell_{\text{abs}} = 135 \mu\text{m}$ at 1552 nm. THG results were presented for extinction lengths smaller than 120 μm , corresponding to a maximum scattering length of 600 μm (expected values for brain tissue at 1552 nm). Cross marks represent Monte Carlo simulation results and circles with dashed lines represent the approximate range of our experimental results.

4.3.4: Tissue Heating Properties during THG Imaging

To avoid thermal damage during THG imaging, we investigated the heating properties of tissue by measuring tissue surface temperature using an infrared thermal camera (FLIR, A325SC). We also performed heat transfer simulations to predict the temperature distribution below the surface. To keep the field of view clear for the thermal camera's view, the laser light was focused on tissue surface using a long working distance objective (Nikon, Plan Apo, 10 \times , 0.3NA) for surface temperature measurements.

From these surface temperature measurements, we first characterized thermal relaxation time of the tissue, τ , defined as the time that the temperature dropped to $1/e$ of its maximum value after the laser was shut down. Knowledge of this parameter enabled us to perform THG imaging without causing substantial heating of tissue by blocking the laser between different imaging planes for the duration of the characteristic cooling times. We measured the thermal relaxation time of the bulk tissue for different laser excitation conditions where the tissue was juxtaposed against a cover glass, and the laser was scanned for 4 seconds while being focused at the maximum imaging depth of 420 μm within the tissue. The measured temperature distribution for a single imaging session (Fig. 4.5a) showed a maximum temperature increase of 1 to 6 $^{\circ}\text{C}$ as the imaging power was increased from 120 mW to 480 mW. The thermal relaxation times (τ), tabulated in Table 4.2, varied only slightly around 15 s which were in the range of the values cited in literature for various tissue types [165, 170]. The average value was also in agreement with an estimated value of 13.86 s that could be obtained using the simplified expression for relaxation time:

$$\tau \sim \frac{\rho V c}{h A_s}, \quad (4)$$

where $\rho = 1050 \text{ kg/m}^3$ is the tissue density, $c = 3940 \text{ J/kgK}$ is the specific heat of the tissue, $A_s = 9.1 \times 10^{-8} \text{ m}^2$ is the area of the spot size, $V = 3.1 \times 10^{-12} \text{ m}^3$ is the volume of the laser spot, and $h = 10 \text{ W/m}^2\text{K}$ is the convective heat transfer coefficient of ambient air.

Table 4.2. Tissue thermal relaxation times (τ) for exposure to different average powers (P_{ave}).

Average Power, P_{ave}	120 mW	240 mW	480 mW
Experimental τ (s)	15 ± 0.5	15 ± 0.4	15 ± 0.2
Theoretical τ (s)	14 ± 1.1	14 ± 1.1	14 ± 1.1

Since the maximum temperature was expected to be close to the focal volume below the surface where we could not measure the temperature, we performed heat transfer simulations to estimate the depth-resolved temperature distribution. Our numerical analysis first calculated the intensity distribution inside the tissue by using the transient Radiative Transport Equation [171, 172]. It then calculated the temperature distribution by coupling Pennes energy equation with a non-Fourier damped heat conduction equation [171, 172]. It has been previously shown that the non-Fourier hyperbolic heat conduction model was more accurate model since it takes into account the relaxation time of the tissues. In addition, the Fourier parabolic heat conduction model is found to deviate significantly from experimental measurements while studying heat transfer phenomenon for time scales shorter than thermal relation time of the medium [165].

To validate our numerical results, we measured the evolution of surface temperatures and imaging power over the duration of a depth resolved THG imaging (Fig. 4.5b). To avoid heating the tissue, we blocked the laser in between different imaging planes (separated by 12 μm steps) for 2 thermal relaxation time periods (30 s). The measured surface temperature distribution correlated best with the numerical temperature distribution assuming a 15 s thermal relaxation time in agreement with the measured data. The corresponding results indicated that the maximum surface temperature did not

exceed 32 °C, representing only a 5.5 °C increase from the initial room temperature. These results were obtained with a long working distance objective for an average excitation power ranging from 1 mW at the surface up to 100 mW at the maximum imaging depth of 420 μm . This result verified both our experimental and numerical methods to determine depth-resolved tissue temperature distribution for THG imaging.

After this verification, we applied our numerical analysis for a typical 3D THG imaging where we used the high NA objective (0.75 NA, 20 \times , Nikon) and varied the excitation power with depth as indicated in Fig. 4.6. The estimated surface temperature and imaging power over the duration of this experiment are shown in Fig. 4.6a. Figure 4.6b represented estimated depth-resolved temperature distribution. A maximum temperature increase of about 2 °C occurred at the maximum imaging depth of 420 μm , where imaging power was maximum (55 mW). This temperature increase was not deemed detrimental to the tissue constituents [173, 174]. This temperature model was based on linear absorption of water and we developed another numerical model according to the study of Vogel and his colleagues to elucidate the effect of nonlinear absorption on the transient temperature evolution at the focus. This nonlinear absorption analysis resulted in roughly 0.3 °C temperature increase for both a single pulse and series of pulses. Thus, we safely neglected nonlinear absorption in our thermal model. This result showed how accurately we could control temperature increase by measuring the thermal relaxation time and manipulating the laser shuttering time in THG imaging.

Finally, we estimated the maximum temperature inside the tissue at the focal plane for different designated periods of time between consecutive imaging planes separated by $12\text{ }\mu\text{m}$ steps (Fig. 4.6c). An interval time of 30 s (twice the thermal relaxation time) indeed provides an optimized condition from the point of view of both experimental duration and temperature increase in the focal plane. For these conditions, the experimental duration is less than 20 minutes and maximum temperature increase is less than $2\text{ }^{\circ}\text{C}$.

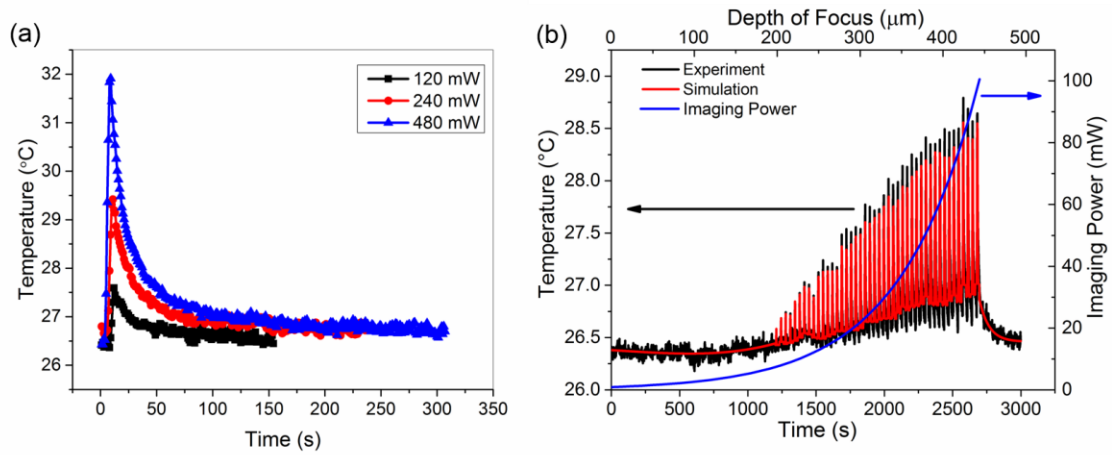


Figure 4.5. Tissue surface temperature measurement using an IR camera. (a) Measurement of tissue surface temperature to calculate tissue relaxation time for three imaging powers applied for the duration of 4 s at the maximum imaging depth of $420\text{ }\mu\text{m}$. (b) Comparison of measured surface temperature evolution with our heat transfer simulation results. Experimental results correlated well with the experiments for a thermal relaxation constant of 15 s. The laser was focused inside tissue using a long working objective lens to clear the imaging path for the IR camera.

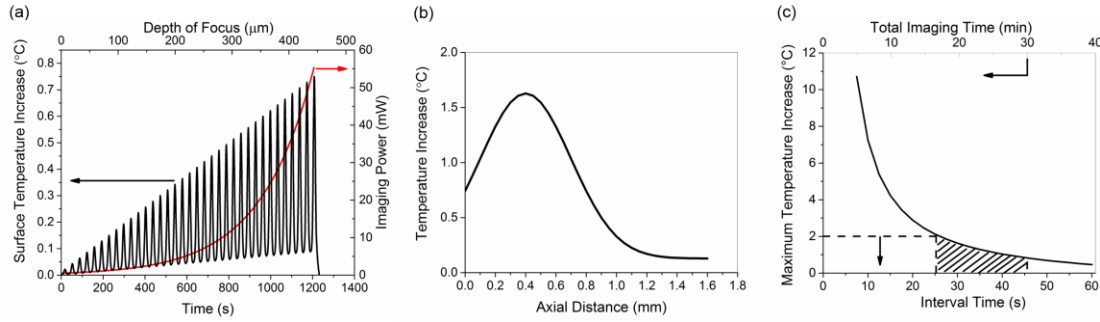


Figure 4.6. Dynamics of tissue temperature during typical THG imaging conditions. (a) The evolution of the surface temperature and imaging power as we image deeper into tissue. (b) Axial distribution of tissue temperature as modeled using 15 s time constant. The maximum temperature increase was observed at the central line of the focal plane at the maximum imaging depth (420 μm) with maximum imaging power (55 mW) and was roughly 2 $^{\circ}\text{C}$. (c) Tissue focal plane temperature and experimental duration vs interval time between consecutive THG imaging with 0.75 NA objective lens.

4.4: DISCUSSION

Overall, our heat transfer simulations concluded that the imaging at 1552 nm required special attention on choosing the correct time interval in between different imaging planes in order to avoid heating damage to tissue. Nevertheless, it was possible to image the tissue of interest down to its theoretical maximum imaging depth beyond 400 μm if the laser was shut down for the duration of two thermal relaxation times (30 s) for cooling in between consecutive imaging planes.

In principle, it should be possible to avoid heating overall by using a laser with shorter pulses and or lower repetition rates. To understand this effect, we need to analyze the relationship between parameters affecting the time averaged signal generation in three-photon based microscopy techniques given as [154]:

$$\langle I_{f3P}(t) \rangle \sim \frac{P_{ave}^3}{(\tau_p f_p)^2} \left(\frac{NA^2}{hc\lambda_{exc}} \right)^3 \quad (5)$$

Here I_f represents generated nonlinear signal intensity, P_{ave} is the average laser power, τ_p is the pulse width, f_p is the repetition rate of the laser, NA is the numerical aperture of the objective, and λ_{exc} is the excitation wavelength. It is evident from this equation that P_{ave} can be kept low by either increasing the objective NA or/and decreasing τ_p and f_p . Considering our experimental conditions ($\tau_p = 600$ fs, $f_p = 2$ MHz, and effective $NA \sim 0.5$), the maximum imaging power could be reduced by ~ 3 times by decreasing the τ_p to < 100 fs. The second parameter to consider would be the NA of the focusing objective. Since water absorption at this wavelength is high, it was not feasible to utilize water dipping lens. Thus, air objective lens with the highest NA possible (0.75 NA) was the only option for deep imaging using 1552 nm. Increasing the NA could have provided a remarkable reduction in average powers used.

The third option to avoid heating would be to reduce the repetition rate. In one hand, f_p is required to be high enough (\sim MHz levels) to provide fast imaging speeds (at least 1 fps) for realistic clinical applications, on the other hand, decreasing f_p would reduce tissue heating. For example, reducing the repetition rate from 2 MHz, the maximum available repetition rate with our fiber laser, to 300 kHz would reduce the required P_{ave} by 3.5 times. Indeed, when we tested THG imaging at 300 kHz repetition rate where the pulse duration of our laser changed to 1.5 ps, we needed to use about half of the average power to obtain THG images, consistent with the expected relationship given in Eq. 5. However, while reduced average power reduced tissue heating effects, the increase in

high peak intensities started initiating optical breakdown in tissue as we imaged deeper. A quick calculation showed that at depths of 300 μm , the fluence at the focal plane could reach to approximately 1 J/cm^2 at low repetition rates, causing tissue ablation. We therefore chose 2 MHz repetition rate for our imaging conditions while cooling in between the imaging planes to avoid tissue heating.

A similar phenomena was also observed in a recent study, where THG was used to image myelin in mouse using 1045 nm laser [154]. They found that the maximum imaging depth in their excitation wavelength was limited to less than 2 scattering lengths, 50 – 75 μm deep in the tissue. Due to the very short, highly absorbed, UV emission wavelengths (350 nm), even at these shallow imaging depths, high laser powers (25 – 50 mW) were required to generate enough THG signal, causing either nonlinear optical breakdown or tissue heating depending on the chosen repetition rate of the laser.

In conclusion, as with all nonlinear imaging modalities, in THG microscopy it is especially important to understand how to optimize laser and optical parameters such as average power, pulse width, repetition rate, numerical aperture, and excitation wavelength to optimize maximum imaging depth while avoiding damage to tissue. Even though excitation wavelength of 1552 nm shows strong tissue absorption, by carefully choosing the imaging parameters one can perform deep tissue imaging without causing any thermal damage to tissue. Of course, one can avoid λ_{exc} with strong water absorption in the range of 1.2 – 1.8 μm to avoid tissue heating all together and emit photons in the visible range to have remarkable collection efficiency. Thus, either 1.3 or 1.7 μm

wavelength could be a good fit for this purpose. In terms of repetition rate, ~2 MHz should be enough to have reasonable frame rate (~1 fps) and also provide enough THG signal. Finally, the pulse width should be tuned to the regime <100 fs to avoid thermal damage and optical breakdown during imaging.

4.5: CONCLUSION

The primary goal of this work was to perform in-depth analysis using numerical, analytical, and experimental techniques to understand the limitation of maximum imaging depths with third-harmonic generation microscopy in turbid tissues such as vocal folds compared to two-photon autofluorescence microscopies. Our experimental results revealed that maximum imaging depth improved significantly from 140 μm to 420 μm using THG microscopy at 1552 nm excitation wavelength as compared to TPM at 776 nm. This maximum imaging depth improvement was a direct result of the increased total extinction length and reduced out-of-focus signal resulting from three-photon processes.

Another important contribution of this study was to understand how to avoid thermal heating during THG imaging at 1552 nm excitation wavelength. By performing surface temperature measurements, optimizing the repetition rate of the laser, and modeling tissue temperature as a function of depth, we avoided tissue heating. We characterized the thermal relaxation time of tissue with different imaging powers and utilized this relaxation time to estimate the depth resolved temperature distribution. The experimental and theoretical thermal relaxation times (~ 15 s) correlated well with each other, implying that the optical and thermal tissue properties used were accurate. Then, we developed a numerical algorithm where the intensity distribution inside the tissue was determined by

the Radiative Transport Equation (RTE) and the temperature distribution estimated by coupling the Pennes Bioheat equation with a non-Fourier damped heat conduction equation. By shuttering the laser beam for 30 s between consecutive imaging planes we avoided heating and kept a maximum temperature increase of less than 2 °C inside the tissue. Such temperature control avoided thermal damage to the tissue, which made THG imaging at 1552 nm wavelength safe to use.

Overall, with effective thermal management, the threefold improvement in maximum imaging depth presented here will guide development of turn-key femtosecond fiber laser-assisted treatment methods for sub-epithelial image guided surgeries, similar to the proposed scarred vocal folds treatments currently under development in our lab.

Chapter 5: Quantitative Differentiation of Normal and Scarred Tissues using Second Harmonic Generation Microscopy for the Treatment of Vocal Fold Scarring

5.1: INTRODUCTION

Vocal fold scarring is one of the predominant causes of voice disorders, affecting an estimated 2 to 6 million people in the US alone [2, 175-179]. Vocal fold scarring arises as a wound healing response to injury or inflammation and results in collagenous scar tissue which impairs vibration [117, 180-182] by reducing the viscoelasticity of the vocal fold. During the wound healing response, scar tissue can replace the superficial lamina propria (SLP) along with deeper parts of the lamina propria (LP). The scar tissue predominantly consists of collagen and fibronectin, both of which increase the stiffness of the mucosa and can lead to severe impairment in voice production or dysphonia [1]. Unfortunately, current methods for treating vocal fold scarring are inconsistent and frequently ineffective, and there is currently no accepted treatment for restoring phonation to scarred vocal folds [1, 6, 7, 95, 96, 125, 183, 184].

In scarred vocal folds, collagen fibers are found to be more organized and densely packed compared to normal vocal folds [54, 117, 185]. The collagen fiber orientation and density are good indicators for different properties of biological tissues [186, 187]. The gold standard method to determine collagen fiber density and direction is to stain tissue sections with picrosirius red or Masson's trichrome. This analysis requires complex and destructive sample preparation to stain collagen fibers, and analysis is typically based on subjective scoring systems, which limits comparisons among different studies. Thus, there is a need to develop a nondestructive technique to resolve collagen fibers in three-dimensional (3-D) tissues and automatically quantify fiber density and directionality to provide objective endpoints for evaluating the treatment of vocal fold scarring.

The hamster cheek pouch model has been widely used as a model for mucosal disease processes such as carcinogenesis [106-108, 110]. Like the vocal fold mucosa, there is a squamous epithelium, an underlying lamina propria (which is thinner than specialized vocal fold lamina propria) and then a thin layer of striated muscle. The layered structure is analogous to the vocal fold although the thickness of the constituent layers is thinner in the cheek pouch. The cheek pouch is much more accessible and has a larger area than the vocal fold. While the surface area of one vocal fold is a few mm² in laboratory rodents, the hamster cheek pouch area that can be everted through the mouth is a fold of mucosa that is about 100 mm² on each side. Thus, the size of the cheek pouch, the fact that it can be everted for treatment or imaging, and the analogous anatomical organization of the tissue layers are the main advantages of this model. Using this model, one could track the development of scar in vivo or follow the effects of scarring-related treatments such as application of steroids or drugs targeting pathways involved in fibrosis.

Multi-photon nonlinear imaging microscopies such as two-photon autofluorescence microscopy (TPAF) and second-harmonic generation (SHG) microscopy can perform noninvasive and three-dimensional deep tissue imaging with subcellular resolution using tightly focused ultrashort pulses [50, 99]. Second-harmonic generation (SHG) microscopy is a coherent two-photon process necessitating intense ultrashort laser pulses passing through a highly polarizable material with a non-centrosymmetric molecular organization, such as collagen fibers [142]. SHG microscopy has been shown to be a highly functional and noninvasive tool to obtain 3-D resolved collagen distribution and density in human cadaver vocal folds [188] and porcine vocal folds [54].

Different computational methods have been suggested to quantify the average fiber direction and fiber density in an image obtained by different imaging modalities. The Fourier transform is most commonly applied and the two dimensional (2D) power spectral density (PSD) of an image can be computed [189-192]. Sampling the average power of the PSD at pixels corresponding to different angles can yield an accurate measure of the total fiber orientation distribution in the image [193]. More complex fiber orientation determination techniques also have been demonstrated with defining and tracking fiber objects through energy minimization or line propagation algorithms [194-196]. Recently, an algorithm to rapidly and accurately detect fiber orientation was developed³⁷ and used to quantify fiber organization in cutaneous scar tissue which was created on dorsum by pressing a brass block preheated to approximately 95 degree celcius to the skin for 10 s [197]. For the fiber density calculations, it is required to determine the optimum threshold intensity that represents the minimum collagen fiber intensity for each image. Then, collagen fiber density can be computed by taking the ratio of the number of pixels with intensities exceeding the optimum threshold intensity relative to the total number of pixels. The selection of appropriate intensity thresholds can be determined by Otsu's method, which calculates the optimal threshold intensity to divide signal and background values so that their combined variance is minimal [186, 198, 199].

The aim of the present chapter is to differentiate control and scarred hamster cheek pouch samples through quantifying collagen direction and density with an automated SHG image analysis technique. This technique is based on taking the Fourier transform (FT) and calculating the 2D power spectral density of depth-resolved SHG images to determine collagen fiber direction. Additionally, our technique utilizes intensity thresholding of the SHG signal to calculate any differences in collagen fiber

density. Overall, this chapter illustrates the feasibility of utilizing SHG imaging and automated image analysis techniques to non-invasively quantify collagen organization during vocal fold scarring and guide surgical interventions. With this mucosal model, one could test scar treatments such as drugs or growth factors, and eventually measure treatment outcomes of vocal fold scarring in humans.

5.2: MATERIALS AND METHODS

5.2.1: Experimental Setup

We used our home-built, upright laser-scanning microscope to perform two-photon autofluorescence (TPAF) and second-harmonic generation (SHG) microscopies (Fig. 5.1) using an ultrafast Er-doped fiber laser (Discovery, Raydiance Inc.). This laser provided 3 W average power at 1552 nm (1.5 μ J pulse energy) and 1 W when frequency doubled to 776 nm (0.5 μ J pulse energy) at 2 MHz with a 600 fs pulse width. We utilized frequency doubled 776 nm excitation wavelength to perform SHG and TPAF imaging. We focused the laser beam with a 0.75-NA, 20 \times air objective (Nikon Plan Apo). To correctly measure the spot size, we suspended 100 nm fluorescent beads (Invitrogen, F8803) in agar gel and measured the spot size at imaging depths from 50 to 500 μ m. The average lateral full width half maximum (FWHM) of the two-photon point spread function (PSF) was $0.58 \pm 0.07 \mu$ m, corresponding to a $1.39 \pm 0.17 \mu$ m $1/e^2$ diameter of the intensity distribution. We scanned the laser beam in the x and y-axes using a pair of galvanometric mirrors (Cambridge Technologies, Inc.), and swept the focal spot over a $150 \times 150 \mu$ m² field of view in 3.3 s. The axial displacement between consecutive SHG images was 2 μ m, and SHG imaging depth was increased until the signal to noise ratio became 1. The maximum SHG imaging depth was approximately 120 μ m for all control and scarred tissue samples. Since the number of pixels was 512 in both axes, there were 2

pulses/pixel for TPAF and SHG. The computer software (MPScan) reconstructed these signals into 512×512 pixel images at 3.05 frame per second (fps).

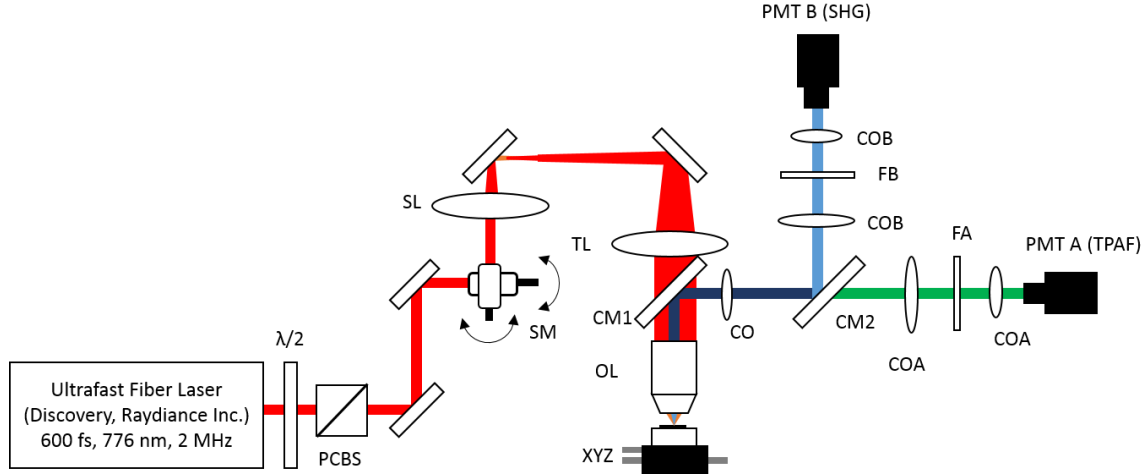


Figure 5.1. Schematic of the upright microscope system for nonlinear imaging. (a) Ultrafast laser pulses at 776nm from a compact fiber laser system first pass through an energy attenuator consisting of a half-wave plate ($\lambda/2$) and polarizing cube beam splitter (PCBS). Laser pulses are scanned by a pair of galvanometric scanning mirrors (SM), which is imaged on the back aperture of a 0.75-NA, 20 \times objective lens (OL) by a scan lens (SL) and tube lens (TL) pair. The samples are placed on a three-axis motorized stage (XYZ) for nonlinear imaging. Emitted light (either TPAF or SHG) is collected by a cold mirror (CM1) and collection optics (CO). A second cold mirror (CM2) separates SHG and TPAF signals into different collection paths.

5.2.2: Automated SHG Image Analysis Technique

Collagen fiber direction in the SHG images was determined in a similar manner to previous Fourier-based analysis approaches [191, 193, 200]. Each gray scale image is composed of pixels that vary spatially in intensity. Rapid changes in intensity are indicative of object edges and thus fiber orientation can be quantitatively analyzed through a 2D Fourier transformation of the image into frequency space. Prior to transformation, SHG images were apodized using a Hann window to eliminate discontinuities at the edges of the image. A power spectral density (PSD) was computed from real and imaginary parts of the 2D discrete Fourier transform and provided the

relative magnitudes of the underlying frequency components of the image. Rapid changes in intensity across an image at a given orientation are reflected by greater power density values in the orthogonal direction in Fourier space. The PSD map is symmetrical about the origin located in the center of the map, and polar coordinates relative to the origin were assigned to each PSD pixel location. Average PSD values were computed in discrete increments of 1° within spatial frequencies ranging from 0.05 to 0.5 pixels^{-1} to obtain orientation distribution histograms for each image. The average collagen fiber direction and directional variance were calculated from the orientation distribution of each image through vector addition [200]. Directional variance values range from 0 (perfectly aligned fibers) to 1 (isotropic/random organization).

Collagen fiber density in the SHG images was obtained by computing the number of pixels with intensities exceeding the optimum threshold intensity relative to the total number of pixels. Determination of this optimum threshold intensity was automated using Otsu's method [199]. Otsu's method is a nonparametric and unsupervised method for automatic threshold selection for 2-D images using the zeroth- and the first-order cumulative moments of the gray-level histograms.

In order to perform a reliable image analysis in terms of selection of the region of interest without any bias, we chose 5 different locations in a 1.7 mm^2 region for all control and scarred samples. Each region of interest consists of $150 \times 150 \times 120 \text{ }\mu\text{m}^3$ tissue block. In all images, collagen density and directionality calculations were performed between the tissue imaging depths where collagen fibers first appeared and signal to noise ratio became one. In order not to be biased with the region of interest, the center of the first tissue block location was randomly selected and the center of other 4 regions of interest was selected 1 mm apart from the center of the first tissue block in all directions (east, west, north and south). For each tissue block, average fiber direction and density

results were calculated by averaging corresponding 2-D results over the whole tissue block. Then, we averaged each tissue block results to calculate overall fiber direction and density for each control and scarred sample.

5.2.3: Animal Model

We used 4 adult male Golden Syrian hamsters (Charles River Labs, Wilmington, Massachusetts) of 100 to 120 g body weight, in which scars could be created within an easily accessible mucosal surface. To scar the cheek pouches, we first anesthetized the animals by injecting a mixture of ketamine (200 mg/kg) and xylazine (8 mg/kg) intraperitoneally. We then cauterized 5 to 10-mm-diameter circular areas of one cheek pouch with an electrocautery unit (Conmed Saber, Utica, NY, 2400). The hamsters were euthanized after a survival period of 1 month using 0.5 ml intraperitoneal euthasol. The scarred and contralateral normal cheek pouches were removed and mounted on rubber test-tube stoppers with fine needles to hold the cheek pouch mucosa flat. After rinsing with saline, the tissue was frozen in isopentane and cooled in liquid nitrogen. The cheek pouch tissue was prepared at Massachusetts General Hospital Voice Laboratory (MGH) in Boston and shipped on dry ice to the Ben-Yakar Laboratory at the University of Texas at Austin for bench-top testing. After delivery, the cheek pouches were stored at -80°C . For each experiment, we thawed the cheek pouches in saline solution and covered them with a glass cover slip to flatten their epithelial surface to compensate aberrations with the objective. To ensure the proper identification of the tissue surface with TPAF, 5 μl of a solution of 100 nm fluorescent beads (F-8823, Invitrogen) in saline was deposited onto the tissue surface prior to placement of the cover slip.

5.2.4: Statistical Analysis

Paired Student's *t* tests were used to compare the collagen fiber directional variance and density between scarred and controlled cheek pouches with $\alpha=0.05$.

5.3: RESULTS

We utilized SHG nonlinear imaging to characterize the direction and density of collagen fibers in normal and scarred hamster cheek pouches. Representative SHG images of normal (Fig 5.2a) and scarred (Fig 5.2d) tissue samples revealed qualitatively that collagen fibers are denser and more aligned in scarred samples than control samples. To obtain a quantitative analysis for collagen fiber direction and density, we performed Fourier-based analysis and intensity thresholding, respectively. In a representative example, the FT results showed that scarred tissue samples (Fig 5.2e) had a directional variance of 0.61 and the amplitude of the dominant direction was at least 4-fold greater than other directional angles. On the other hand, control tissue samples (Fig 5.2b) had a variance of 0.70 and the amplitude of the dominant direction was comparable to most of the other directional angles. After determining fiber direction in the SHG images, we performed automatized intensity thresholding to obtain the collagen fiber density. A representative example of this analysis showed that the fiber density in the scarred tissue samples (Fig. 5.2f) was 4-fold higher than the fiber density in the control tissue samples (Fig. 5.2c).

To reveal the distribution of collagen fiber direction with respect to imaging depth, we report a depth-resolved plot of collagen fiber orientation distribution for both normal and scarred tissue samples in Figure 5.3. In Figure 5.3, the collagen fiber direction distribution is represented with respect to imaging depth as well as its corresponding average power as a color bar on the right hand side. Normal tissue samples (Fig 5.3a) had no dominant fiber direction for the entire 120 μm imaging depth. On the

other hand, scarred tissue samples (Figure 5.3b) showed significant fiber alignment between 40 and 100 μm imaging depth. The average fiber direction was $130 \pm 5^\circ$ and this direction was approximately constant in the range of 40-100 μm imaging depth. Collagen fibers did not appear between 0-40 μm , because this corresponded to the epithelial layer of the tissue.

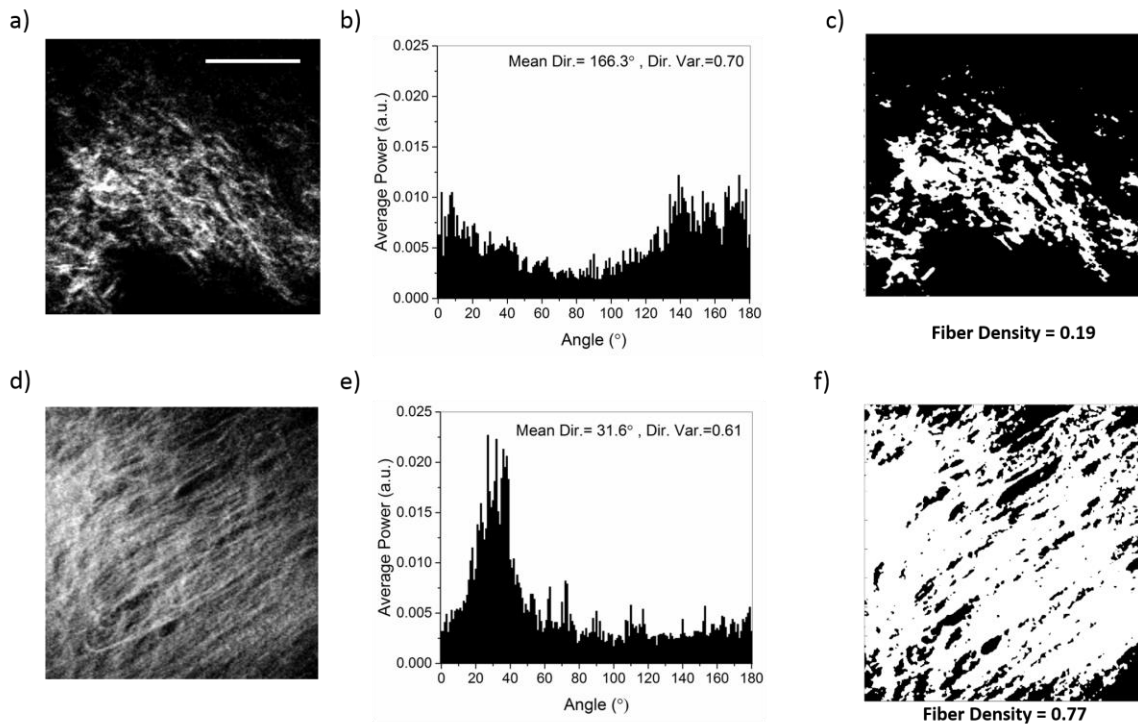


Figure 5.2. Representative SHG images, collagen fiber direction histograms, and collagen fiber density plots for a control (a,b,c) and a scarred (d,e,f) hamster cheek pouch. The scale bar represents 50 μm .

To evaluate the utility of these quantitative metrics and understand inter- and intra-sample variations in fiber density and direction, we performed depth-resolved fiber direction and fiber density analysis at 5 different locations with 4 different normal and scarred tissue samples as shown in Figure 5.4. Lower collagen fiber directional variance ($p < 0.005$ for Sample 1,3 and 4 and $p < 0.05$ for Sample 2) was observed in scarred tissues

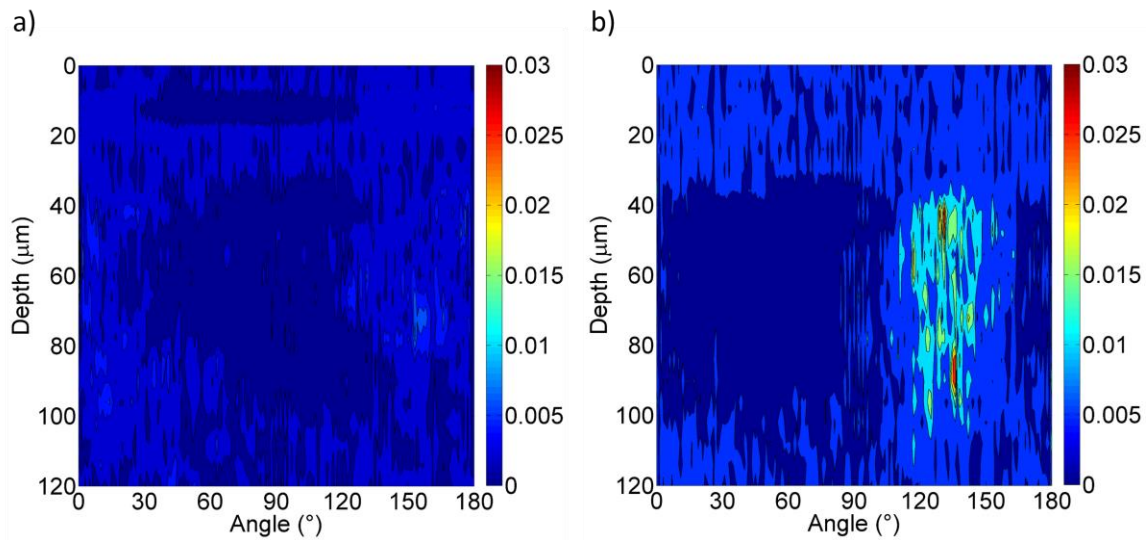


Figure 5.3. Representative depth-resolved collagen fiber direction for a control (a) and a scarred (b) hamster cheek pouch.

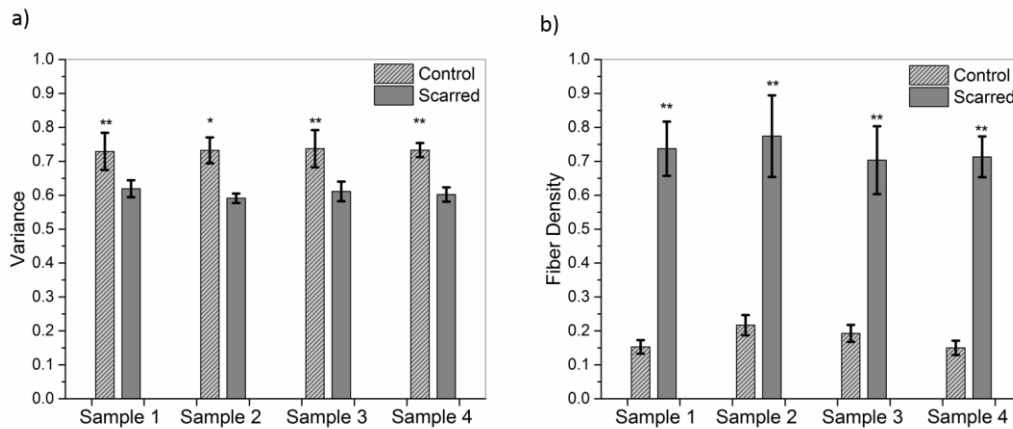


Figure 5.4. Collagen fiber directional variance and fiber density for 5 different regions of 4 samples. (a) In all samples, directional variance is lower in scarred samples than control samples. (b) Collagen fiber density is 3-5 folds higher in scarred samples than in control samples. (**= $p < 0.005$, *= $p < 0.05$)

than control ones (Fig. 5.4a). This analysis showed that scarred tissue samples had more aligned collagen fibers than the controls for all 4 samples. The fiber density in scarred tissues was also higher ($p < 0.005$) than control tissues for all 4 samples (Fig. 5.4b). The ratio of fiber density between scarred and control tissues varied between 3- and 5-fold. Overall, both fiber direction and fiber density analysis revealed a statistically significant difference between control and scarred tissue samples.

5.4: DISCUSSION

To develop and evaluate effective treatments, it is necessary to understand and objectively characterize structural changes during vocal fold scarring. Density and organization of the extracellular matrix (ECM) components determine the biomechanical function of the lamina propria. Several previous studies have addressed the distribution and density of collagen fibers in the lamina propria in relation to vocal fold scarring. In some of these studies, collagen density has been determined by performing immunohistology and it was shown that collagen became thicker, more organized, and denser (2-5 fold) in mature scarred vocal folds [54, 117, 185]. On the other hand, other histological studies have demonstrated low or high density and disorganized collagen fiber for early stages of vocal fold scarring [125, 185]. This difference in collagen density among previous studies may attribute to the fact that there is a different timeline in animal models for remodeling stages of vocal fold scarring where there is an ongoing process of collagen synthesis. Similarly, wound-healing studies suggest that as remodeling progresses (20 days to one year), collagen fibers become thicker and more organized (parallel arrays) with eventual crosslinking [201]. Unlike collagen fiber density, fiber direction has only been evaluated qualitatively in previous vocal fold scarring studies. As demonstrated in other tissue types, quantitative analysis of fiber density and direction provides important information on the stage of scarring [197]. In our study, fiber directional variance values, which range from 0 (perfectly aligned fibers) to 1 (isotropic/random organization), were significantly lower ($p < 0.05$) in scarred tissues compared to control ones, indicating increased fiber alignment in the scar. Lower fiber directional variance values in scar tissues are consistent with previous measurements in mature scars from a rat model of cutaneous burns [197].

Since routine histology is a destructive method requiring complex processing steps, it is a valuable alternative to be able to non-invasively determine collagen fiber direction and density to assess the progression of vocal fold scarring. Based on the results of our current study, it is expected that the combined use of these analysis metrics and SHG imaging could provide a means to non-destructively monitor vocal fold scarring in research studies and given future development of endoscopic probes in the clinic..

Nonlinear imaging modalities such as TPAF and SHG are well suited for high-resolution in-vivo imaging. SHG microscopy specifically resolves collagen fibers because of their non-centrosymmetric characteristics. Since SHG is an inherent nonlinear imaging modality, it can provide deep tissue imaging of unstained tissues. SHG microscopy provides approximately 120 μm imaging depth within hamster cheek pouches in this study. The maximum imaging depth in SHG microscopy is highly dependent on optical properties of tissues. It has been shown that the maximum imaging depth can vary between 3-4 scattering lengths at 800 nm excitation wavelengths for different tissues [202, 203]. Since the scattering length of hamster cheek pouches has been found to be 30-35 μm at 776 nm wavelength [54], the maximum imaging depth should be around 100-150 μm range, corresponding well with our experimental results. Thus, SHG microscopy is a good candidate for clinical evaluation of scarring in the superficial lamina propria of the vocal fold. Even though optical coherence tomography (OCT) has been used in the clinical setting, there remains a need for new tools such as SHG microscopy with higher specificity to collagen, and finer resolution to discriminate individual fibers within the scar.

To summarize, we utilize Fourier-based orientation analysis and intensity thresholding to determine collagen fiber direction and density, respectively, in three-dimensional SHG image stacks of control and scarred hamster cheek pouches. Our results

are promising in that both fiber direction variance ($p < 0.05$) and fiber density ($p < 0.005$) are significantly different between control and scarred hamster cheek pouches. We believe that this automated SHG image analysis method can provide significant feedback on fiber density and alignment in normal, scarred and surgically or medically treated vocal folds. Also, one could test scar treatments such as biomaterials, drugs or growth factors which will eventually be used to measure treatment outcome in humans.

5.5: CONCLUSION

This chapter assessed the potential of an automated SHG image analysis method to differentiate normal and scarred hamster cheek pouch samples by quantifying collagen fiber direction and density. With this method, one could track the development of vocal fold scar in vivo or follow the effects of scarring-related treatments due to the analogous anatomical organization of the tissue layers between the hamster cheek pouch and vocal folds. We utilized Fourier-based methods and intensity thresholding to determine collagen fiber directional variance and density, respectively. The resultant depth-resolved average fiber direction variance was 0.732 ± 0.041 for control and 0.606 ± 0.025 for scarred hamster cheek pouches, respectively. This analysis showed that the fiber direction in scarred samples was less random than in control samples. Depth-resolved collagen fiber density was 0.178 ± 0.025 for control and 0.721 ± 0.090 for scarred tissues, respectively. This four-fold difference in collagen fiber density demonstrated, as expected, that the average fiber densities in scarred tissues were remarkably higher than that in control tissues. The method we presented here will guide development of testing scar treatments such as biomaterials, and turn-key ultrafast fiber laser-assisted treatment methods for sub-epithelial image guided surgeries, similar to proposed scarred vocal folds treatments currently under development in our lab [13, 54, 60, 61, 89, 131].

Chapter 6: Biogel Injection in Scar Tissue Enabled by Ultrafast Laser Ablation for the Treatment of Vocal Fold Scarring

6.1: INTRODUCTION

Vocal fold scarring is one of the predominant causes of voice disorders, affecting an estimated 2 to 6 million people in the US alone [2, 175-179]. Vocal fold scarring is resulted from inflammation or injury of the mucosa which increases the stiffness of the mucosa and can lead to severe impairment in voice production or dysphonia [1]. During wound healing response, scar tissue can replace the superficial lamina propria (SLP) along with deeper parts of the lamina propria (LP). Histological changes within the SLP such as increased density and uniformity of thick collagen fibers, decreased density of elastin fibers, and hyaluronic acid (HA) are the main cause of stiffening of the scarred vocal fold [180, 185, 204, 205]. The treatment of vocal fold scarring remains a challenge and a regenerative approach is needed to alleviate this problem. This regenerative approach should target both cells and extracellular matrix (ECM) of the mucosa. Even though a variety of injectable biomaterials have yielded encouraging results with animal and human studies for treating this problem, there is no reliable treatment for vocal fold scarring in the clinic mostly due to lacking of a reliable and a novel drug-delivery system [206].

Different biomaterials have been tested to examine their efficacy on animals such as rabbit, rat and canine [12, 206-216]. Features such as size, stiffness, surface charge, polarity, release rate and PH responsiveness of the biomaterial are very important when using them in injection [3, 217, 218]. The biomaterial HA has been used extensively since its rheological properties and anti-inflammatory properties allow it as an injectable wound healing biomaterial. In a representative study performed on the rabbit model, the subject's vocal folds were first manually injured, and then unilaterally injected with HA

derivative and saline. After 6 months follow-up, the HA derivative injected subjects demonstrated a positive improvement in elastic shear modulus, and viscosity of the vocal folds. It was concluded that HA derivative continued to have a positive effect for 21 days, and these beneficial effects were observed for up to 6 months. In a separate in-vivo study, the biomaterial PEG 30 was tested on the canine vocal fold subjects to determine its effects on the vocal and structural parameters [215]. The canine subjects were endoscopically screened for disorders over 4 months, and chosen based on lack of existing conditions. It was concluded that PEG30 exhibits compatibility without major negative side effects, and shows promise for human scarring [215]. Biomaterials have a positive effect on the vocal folds of animals, and have potential as a reliable treatment to human vocal fold scarring.

According to the feedback from animal studies, biomaterial injection experiments have been conducted on human test subjects recently. Many studies using a variety of injectable biomaterials with the goal of developing a long-term cure have produced an improvement in mechanics, and vocal properties [219-222]. In a long-term study, the effects of injection of basic fibroblast growth factor (bFGF) on the scarred vocal fold were tested against regenerative surgery in addition to implantation [222]. Injection patients were injected four times with weekly intervals, and then again after three months if the effects were minimal. After two years of tracking the subjects, it was determined that the injection of bFGF had positive effects on the Voice Handicap Index, and physical properties including grade, breathiness, asthenia, and strain, but the regenerative surgery with bFGF implantation, showed improvements in all of the parameters above, as well as the maximum phonation time [222]. The effectiveness of biomaterial injection has been shown to be comparable to that of surgery, however more testing must be done to determine a reliable, effective method of treating vocal fold scarring.

Ultra-short laser pulses have been shown to perform surgery and nonlinear imaging of different kinds of tissues. The ultrafast laser surgery process relies upon efficient and rapid energy absorption at the focal plane, which results in minimal energy deposition to the surrounding tissue. The nonlinear nature of the process further confines the efficient absorption to sub-focal volumes. Such a high degree of confinement is especially important when working with delicate tissues, such as vocal folds, and may reduce postsurgical scar formation. Successful laser microsurgery of vocal fold tissue using ultrashort laser pulses have been previously demonstrated, showing the potential for subsurface ablation confined within the sublayers of lamina propria by our group [13, 54, 131]. To guide ultrafast laser microsurgery, focused ultrafast laser pulses can also be used to visualize intrinsic molecular and morphological properties of tissues through nonlinear optical microscopy. Specifically, simultaneous two photon-autofluorescence (TPAF) and second harmonic generation (SHG) microscopies can provide complementary information on the structure of the superficial layer of vocal folds and scar tissue that might be present [50, 98, 99]. For instance, TPAF can resolve NAD(P)H, flavins and cells in the epithelium, and SHG can resolve collagen fibers in the SLP. Low-energy ultrafast laser pulses for imaging can thus provide ultrafast laser microsurgery devices a means for visualizing the region of surgery with the identical field-of-view and resolution of the surgical laser.

In this chapter, we present localization of polyethylene glycol- (PEG) based biomaterial stained with Rhodamine dye into the ablated sub-epithelial voids in scarred hamster cheek pouches. These sub-epithelial voids contain both compressive and tensile forces which result in first expansion and then collapse of these voids through plasma mediated ablation of tissue. Thus, we can create a temporary larger space for biomaterial injection due to the expansion of these voids. Since we scan the laser beam on one plane

of focus in one frame rate, we remove a couple of micrometer thick tissue permanently. With the help of our previous efforts to characterize the optimum laser parameters for creation of these voids and optimization of their lifetime [13, 54] in healthy and scarred hamster cheek pouches, here we successfully create these sub-epithelial voids whose lifetime is at least 20 minutes in scarred hamster cheek pouches. This ample lifetime enables us to inject PEG 30 biomaterial into these voids in an accurate and effective way. The unique nonlinear properties of the ultrafast laser allow us to create a void under the surface of the epithelium without damaging the superficial layers with imaging feedback. This novel drug delivery technique will reduce the required injection pressure, improve the ability of the surgeon to localize the biomaterials, and allow for a minimally invasive surgery option for the patient.

6.2: MATERIALS AND METHODS

6.2.1: Experimental Setup

We used our home-built, upright laser-scanning microscope to perform ultrafast laser ablation, two-photon autofluorescence (TPAF) and second-harmonic generation (SHG) microscopies (Fig.6.1) using an ultrafast Er-doped fiber laser (Discovery, Raydiance Inc.). This laser provided 3 W average power at 1552 nm (10 μ J pulse energy) and 1 W when frequency doubled to 776 nm (3.3 μ J pulse energy) at 303 kHz with 1.5 ps pulse width. We utilized the frequency doubled 776 nm excitation wavelength to perform laser ablation, and SHG and TPAF imaging. We focused the laser beam with a 0.75-NA, 20 \times air objective (Nikon Plan Apo). To correctly measure the spot size, we suspended 100 nm fluorescent beads (Invitrogen, F8803) in agar gel and measured the spot size at imaging depths from 50 to 500 μ m. The average lateral full width half maximum (FWHM) of the two-photon point spread function (PSF) was 0.58 ± 0.07 μ m,

corresponding to a $1.39 \pm 0.17 \mu\text{m } 1/e^2$ diameter of the intensity distribution. We scanned the laser beam in the x and y-axes using a pair of the galvanometric mirrors (Cambridge Technologies, Inc.), and swept the focal spot over a $400 \times 400 \mu\text{m}^2$ field of view for 0.5 s for ablation and 2.5 s for imaging. The axial displacement between consecutive TPAF and SHG images was $2 \mu\text{m}$ and depth-resolved TPAF and SHG images were taken until the signal to noise ratio became 1.

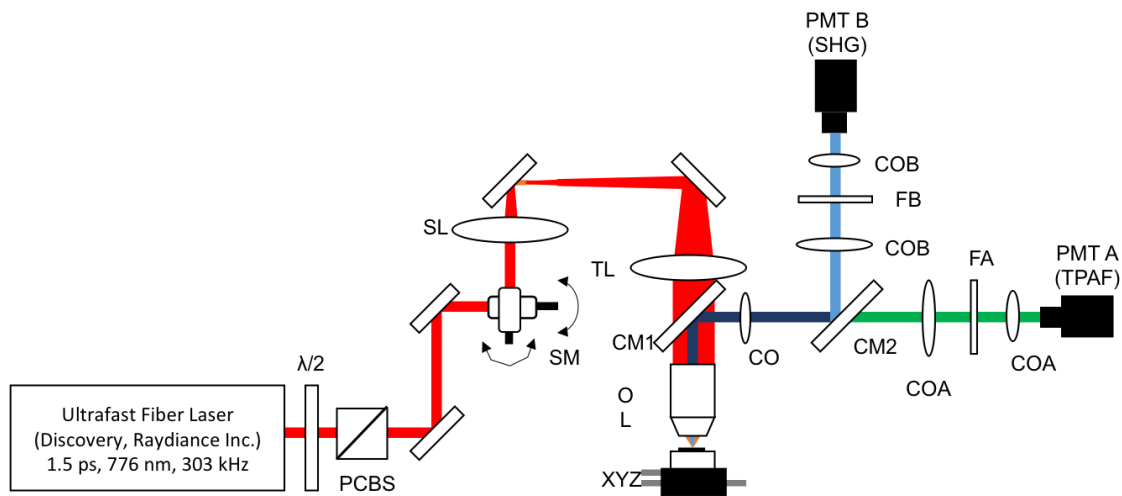


Figure 6.1. Schematic of the upright microscope system for nonlinear imaging. (a) Ultrafast laser pulses from a compact fiber laser system first pass through an energy attenuator consisting of a half-wave plate ($\lambda/2$) and polarizing cube beam splitter (PCBS) at 776nm. Laser pulses are scanned by a pair of galvanometric scanning mirrors (SM), which is imaged on the back aperture of a 0.75-NA, 20 \times objective lens (OL) by a pair of a scan lens (SL) and a tube lens (TL). The samples are placed on a three-axis motorized stage (XYZ) for nonlinear imaging. Emitted light (either TPAF or SHG) is collected by a cold mirror (CM1) and collection optics (CO). A second cold mirror (CM2) separates SHG and TPAF signals into different collection paths.

For laser microsurgery, we raster scanned the laser beam at $90 \mu\text{m}$ below the tissue surface for the duration of one frame, namely 0.5 s (2 fps), using the same galvanometric mirrors with imaging. With a goal to minimize the ablation duration, we chose to use minimal continuous overlapping of the laser pulses in the direction of the scanning. A low degree of overlapping improves the possible beam distortion of

consequently overlapping pulses as well as the speed of ablation. However, without significant pulse-to-pulse accumulation effects, higher pulse energies are usually needed for complete ablation [32]. The choice of one overlapping pulse in the x-direction (512 Hz) automatically dictates approximately 1.7 overlapping pulses in the y-direction (2 Hz) by the imaging software (MPScan). Considering that it takes 0.5 s to scan a $400 \times 400 \mu\text{m}^2$ wide region, we can estimate the speed of ablation as $19 \text{ mm}^2/\text{min}$. By translating the sample underneath the objective, we could create different sized voids ranging from 1 to 2 mm^2 .

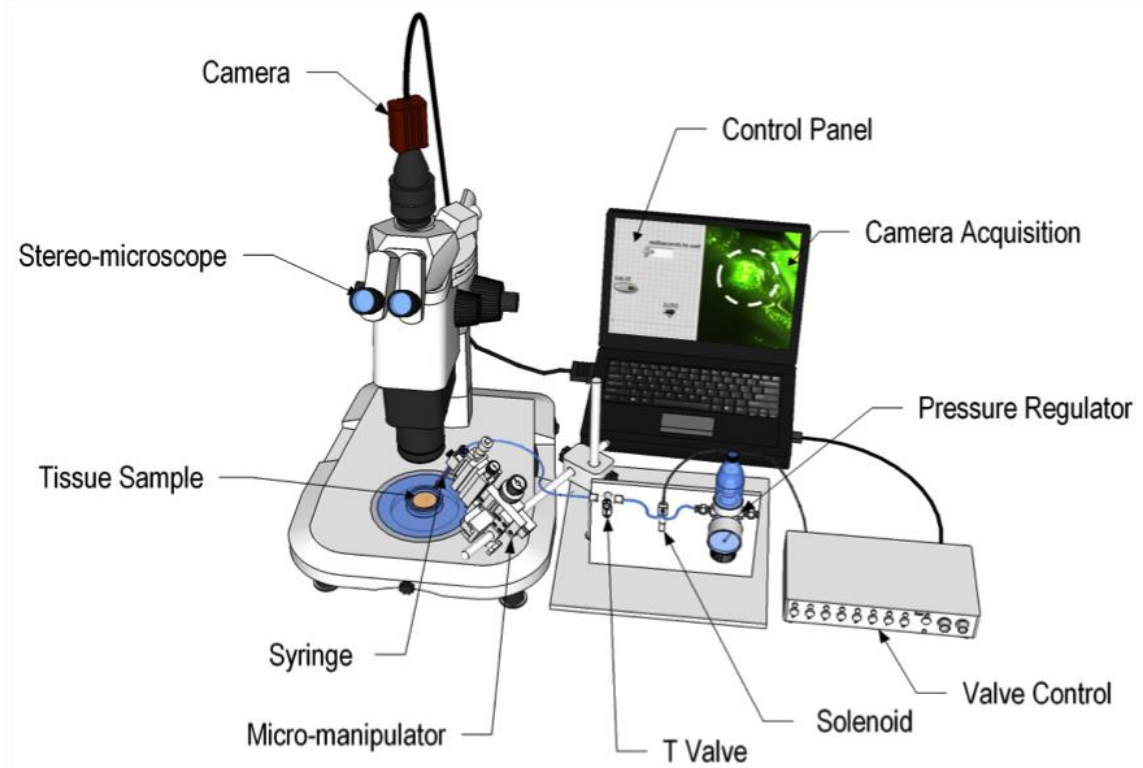


Figure 6.2. Experimental setup for control and monitor of biomaterial injection into a scarred cheek pouch. The flow rate of the biomaterial is controlled by adjusting the air pressure through a pressure regulator and by adjusting exposure time of a solenoid valve with personal laptop. A stereo-microscope is used to monitor localization of the biomaterial and the images are captured via a CCD camera.

For controlling and monitoring injection of the biomaterial, the sample was brought to the semi-automated setup (Figure 6.2). To control the flow rate of the biomaterial, we utilized a valve control, a pressure regulator, a solenoid valve and a T valve. A laptop computer controls the valve control where a custom-made software program determines the flow duration of the biomaterial through turning on the solenoid valve applying air pressure regulated by pressure regulator. The syringe is placed inside a micromanipulator which can precisely change the position of the syringe in three dimensions. In order to monitor the biomaterial injection, we utilized a stereo-microscope and a camera which is connected to the laptop computer. The fluorescent filter in the stereomicroscope enables us to image the Rhodamine 6G fluorescent dye-labeled biomaterial so that we can monitor the efficacy of the biomaterial injection. First, we brought the syringe needle on the surface of the tissue and then immersed it around 100 μm at a 45 degrees angle. Then, we set the flow duration of the biomaterial and start recording video of the biomaterial flow under the stereomicroscope. Finally, we brought the tissue under the nonlinear microscope to reveal the localization of the biomaterial with simultaneous TPAF and SHG imaging.

6.2.2: Animal Model

We used 4 adult male Golden Syrian hamsters (Charles River Labs, Wilmington, Massachusetts) of 100 to 120 g body weight in which scars could be created within an easily accessible mucosal surface. To scar the cheek pouches, we first anesthetized the animals by injecting a mixture of ketamine (200 mg/kg) and xylazine (8 mg/kg) intraperitoneally. We then cauterized 5 to 10-mm-diameter circular areas of one cheek pouch with an electrocautery unit (Conmed Saber, Utica, NY, 2400). The hamsters were

euthanized after a survival period of 1 month using 0.5 ml intraperitoneal euthasol. The scarred and contralateral normal cheek pouches were removed and mounted on rubber test-tube stoppers with fine needles to hold the cheek pouch mucosa flat. After rinsing with saline, the tissue was frozen in isopentane and cooled in liquid nitrogen. The cheek pouch tissue was prepared at Massachusetts General Hospital Voice Laboratory (MGH) in Boston and shipped on dry ice to the Ben-Yakar Laboratory at the University of Texas at Austin for bench-top testing. After delivery, the cheek pouches were stored at -80°C . For each experiment, we thawed the cheek pouches in saline solution and covered them with a glass cover slip to flatten their epithelial surface to compensate for aberrations with the objective. To ensure the proper identification of the tissue surface with TPAF, 5 μl of a solution of 100 nm fluorescent beads (F-8823, Invitrogen) in saline was deposited onto the tissue surface prior to placement of the cover slip.

6.3: RESULTS

To characterize the flow rate of the biomaterial, we measured the volume of the biomaterial with different flow durations at different air pressures. Figure 6.3 represents the mean and standard deviation of 5 measurements for three different pressure values.. Figure 6.3 reveals that the volume of the biomaterial is linearly proportional to the biomaterial flow duration for all pressure values. The experimental requirement for the volume of the biomaterial is between 0.1-0.2 μl since the surface area of the void varies between 1-2 mm^2 and the void thickness is around 100 μm when it is in full expansion. Due to the very short (long) biomaterial flow duration requirement to obtain these volumetric rates, we exclude using 30 (10) psi pressure value. Thus, the optimized experimental conditions become 20-psi pressure and 10-25 ms biomaterial flow duration.

To understand the clinical challenge, we injected PEG 30 biomaterial into a scarred hamster cheek pouch at different locations without creating any sub-epithelial void. Figure 6.4 shows representative images before (Fig 6.4a) and after (Fig. 6.4b and 6.4c) PEG 30 injection. It was obvious that there was not any fluorescent dye or marker before the injection (Fig. 6.4a). It can be easily deduced from Figure 6.4b and 6.4c that we observed a back-flow of the injected biomaterial along the point of injection when injecting the biomaterial without any sub-epithelial voids. This condition ultimately prevented localization of the biomaterial at the desired location. Specifically, Figure 6.4b and 6.4c showed that the fluorescence observed after injection without a void was in fact originating from biomaterial that had flowed back out to cover the tissue surface, and was removed by wiping the tissue after injection. These experiments revealed that it was not possible to inject the biomaterial effectively in a scarred tissue without creating any sub-epithelial voids.

To demonstrate the feasibility of novel drug delivery method with ultrafast lasers, we first created two sub-epithelial voids with the sizes of 1 and 2 mm² in a scarred hamster cheek pouch. Then, we injected PEG 30 biomaterial and wiped the tissue surface after the injection. The two representative images after injection are shown in Figure 6.5. In contrast to the biomaterial injection shown in Figure 6.4, the presence of sub-epithelial voids greatly reduced back-flow at the injection site and resulted in a lasting localization of the injected material as shown in Figure 6.5.

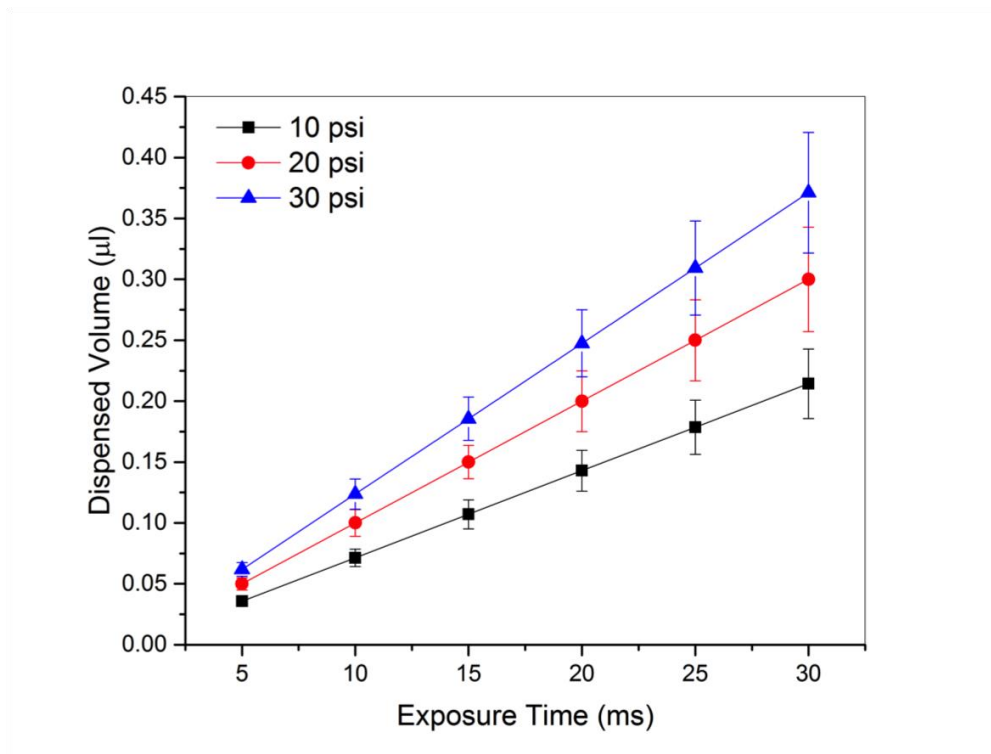


Figure 6.3. Dispersed volume of the biomaterial with respect to its exposure time at different air pressure values. Each measurement was repeated for 5 times and its average and mean standard deviation are presented. Due to the low (high) exposure time requirement, 30 (10) psi pressure option was eliminated so that 20-psi pressure value was chosen to be used in the experiments.

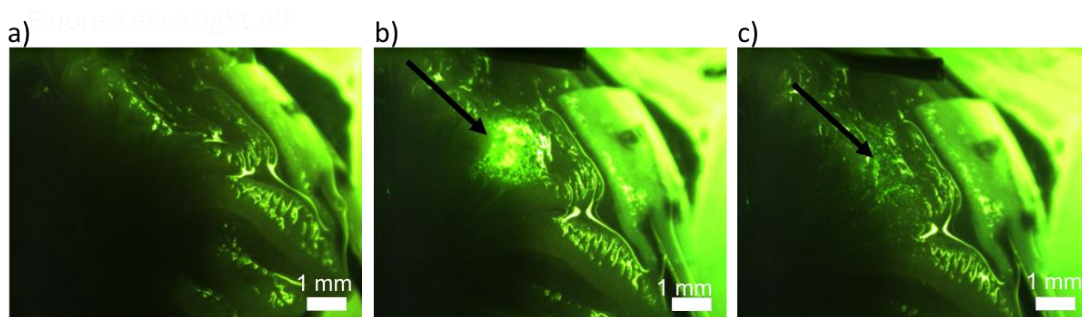


Figure 6.4. Representative fluorescence images before (a) and after (b,c) the biomaterial injection. (a) No fluorescent dye or marker existed before the injection. (b) The point of injection was shown with an arrow. It was not clear whether the biomaterial is localized inside or outside the tissue surface. (c) The tissue surface was wiped after injection and it was observed that most of the biomaterial flowed back outside the tissue surface. The scale bar represents 1mm.

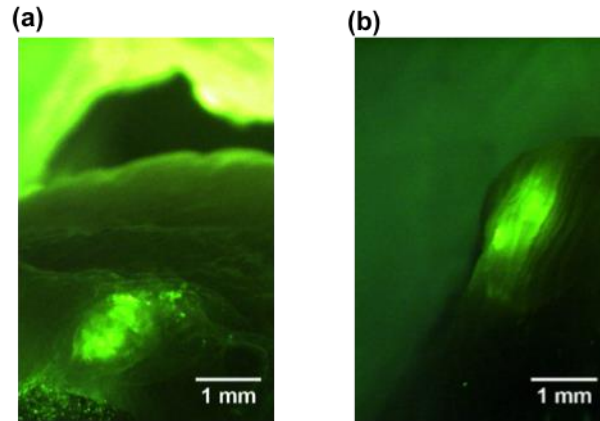


Figure 6.5. Representative fluorescence images after the biomaterial injection into different sizes of sub-epithelial voids. (a) $1 \times 2 \text{ mm}^2$, (b) $1 \times 1 \text{ mm}^2$. After wiping the tissue surface, PEG 30 biomaterial is localized successfully into both of the sub-epithelial voids. The scale bar represents 1 mm.

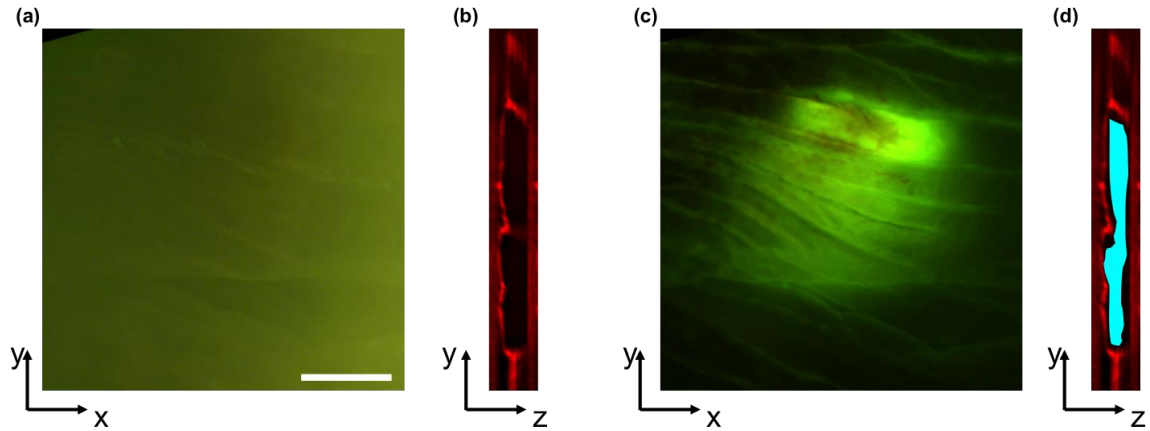


Figure 6.6. Representative fluorescence (a,c) and nonlinear microscopy (b,d) images before and after injection of the biomaterial into a sub-epithelial void. (a) Fluorescence, (b) SHG image just after creating a subepithelial void. (c) Fluorescence, (d) Combined SHG and TPAF image just after injecting the biomaterial into the sub-epithelial void. (c) Fluorescence, (d) Combined SHG and TPAF image revealed the successful biomaterial injection into the sub-epithelial void. The scale bar represents $500 \mu\text{m}$.

To have a better understanding of the localization of the biomaterial, we also performed combined depth-resolved TPAF and SHG imaging in parallel with planar

fluorescence imaging before and after injecting PEG 30 biomaterial into a sub-epithelial void. In a representative example, we first show that the creation of 1 mm² sub-epithelial void can be resolved with combined nonlinear imaging (Fig. 6b) and also planar fluorescence imaging (Fig. 6a). Then, we demonstrate that most of the injected biomaterial is localized into the sub-epithelial void by overlaying depth-resolved TPAF (blue) and SHG (red) signal generated from PEG 30 biomaterial mixed with Rhodamine dye and collagen fibers in the SLP (Fig. 6d), respectively. This depth-resolved (yz) image can provide complimentary information to the planar (xy) fluorescence image (Fig 6c) to determine the efficacy of the biomaterial injection. As a final confirmation of biomaterial localization, we performed a follow-up histology with H&E staining as shown in Figure 6.7. The location and appearance of the biomaterial pointed with an arrow correlate well with the in situ images taken by combined TPAF and SHG nonlinear imaging.

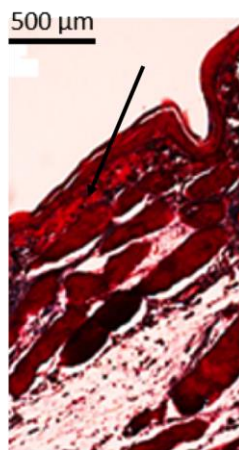


Figure 6.7. Histological follow-up of PEG 30 biomaterial injection into a sub-epithelial void. Arrow indicates the plane targeted for biomaterial injection and confirms the precise localization of the biomaterial. Histology images are stained by H&E. The scale bar represents 500 μm.

6.4: DISCUSSION

To develop an effective treatment for vocal fold scarring, it is necessary to advance functional biomaterials and novel drug-delivery methods in parallel. Although there has been extensive work related to developing promising biomaterials in the last decade, very little effort has been made in terms of drug-delivery techniques. Thus, we believe that this study demonstrates the potential of creating sub-epithelial voids with ultrashort laser pulses as a novel drug-delivery system for vocal fold restoration. By utilizing the void confinement properties of ultrafast laser ablation, planar voids can be created near the epithelium-SLP boundary, which aid in the localization of the biomaterial to be tested for its functional efficacy for any kind of regenerative treatment such as vocal fold scarring. With the use of lower energy ultra-short laser pulses from the same laser system for combined nonlinear imaging techniques such as TPAF and SHG, the structural information from collagen fibers and injected biomaterials can be obtained. In addition, to attain the structural information from the vocal folds, SHG may be useful in identifying collagen fiber direction and density to reveal the location and stage of scarring. Thus, SHG microscopy is a good candidate for clinical treatment of vocal fold scarring where three-dimensional anatomy of scar tissue still needs to be explored. Although optical coherence tomography (OCT) has been used in the clinical setting, there is still a need for new tools such as SHG microscopy with high collagen specificity, high resolution, and reliability for the treatment of vocal fold scarring.

The clinical implementation of this novel drug-delivery technique requires flexible delivery of ultra-short laser pulses to the clinical region of interest using fiber optics. While fiber optic delivery is common practice for many conventional laser applications, fiber propagation poses several challenges with ultra-short pulses. Our group has been developing special fiber-coupled ultrafast laser surgery probes with

nonlinear imaging guidance to overcome these challenges [60, 61, 89]. To follow-up biomaterial injection in the clinic, different clinically accepted visible or near infrared dyes can be utilized to perform one or two-photon fluorescence imaging. Thus, nonlinear imaging-guided ultrafast laser surgery probes can be used to greatly enhance the localization and retention of injected biomaterials used for treating vocal fold scars.

6.5: CONCLUSION

The aim of this study was to develop a novel drug-delivery method to inject and localize PEG 30 biomaterial inside sub-epithelial voids created by ultra-short laser pulses within scarred cheek pouch samples. To demonstrate the feasibility of this technique, we developed a semi-automated system to control and monitor the diffusion of the biomaterial inside scarred hamster cheek pouch samples. In addition to this semi-automated system, we utilized our home-built upright laser-scanning microscope to perform nonlinear imaging guided ultrafast laser ablation. We optimized the biomaterial flow rate parameters such as air pressure and flow duration to reach the required biomaterial volume in a reasonable time. Our results reveal that the optimized experimental conditions are 20-psi air pressure and 10-25 ms biomaterial flow duration for voids of 1-2 mm² size. After this characterization, we first performed biomaterial injection to the scarred tissue samples without any sub-epithelial void to examine the clinical challenge. We observed a back-flow of the injected biomaterial along the point of injection, preventing localization of the biomaterial at the desired locations. In contrast to the biomaterial injection outcomes without any voids, the presence of sub-epithelial voids greatly reduced back-flow at the injection site and resulted in a lasting localization of the injected biomaterial at different locations of the tissue. We also performed a follow-up H&E histology that confirmed that the location and appearance of the biomaterial

correlated well with TPAF and SHG in-situ nonlinear images. Since the direct injection of the biomaterials into the scarred vocal folds is challenging due to the presence of highly stiffened scar tissue, we believe that creation of thin sub-epithelial voids assisted with nonlinear imaging guidance by ultrafast lasers can ease the injection and localization of the biomaterials to restore the mechanical functionality of the vocal folds. The novel method we presented here will guide the development of ultrafast fiber laser-assisted treatment methods for sub-epithelial image guided surgeries, similar to the proposed scarred vocal folds treatments currently under development in our lab.

Chapter 7: A 5-mm Piezo Scanning Fiber Device for High-Speed Ultrafast Laser Microsurgery³

7.1: INTRODUCTION

Ablation with ultrafast lasers can provide an unmatched microsurgical precision [27, 42]. However its clinical adoption has been mainly achieved for ophthalmic applications due to the lack of a means to flexibly deliver the laser light to clinical sites in or on the patient [41, 131, 223, 224]. To overcome this main technological barrier, we focused our efforts, thus far, on the development of miniaturized fiber probes capable of femtosecond laser microsurgery combined with nonlinear optical imaging. The ability to deliver ultrashort laser pulses with micro-Joule levels of energy through an air-core photonic bandgap fiber (PBF), enabled us to perform precise ablation of individual cancer cells guided with nonlinear imaging using miniaturized probes [60, 61]. By incorporating a scanning mechanism based on microelectromechanical system (MEMS) mirrors, we could also perform a high resolution imaging of tissue intrinsic signals [61]. While, the use of a high repetition rate, 80 MHz, femtosecond laser oscillator was sufficient for imaging, surgery required the use of higher energy pulses from a low repetition rate, 1 kHz, amplified system. However, surgery speeds with such low repetition rate lasers are too slow for clinically relevant procedures and the need for two separate lasers makes the whole system bulky, costly, and complicated.

For clinical use, compact and robust laser systems are desired with high pulse energies and repetition rates to enable image-guided and high speed surgery. Ultrafast

³ Ferhanoglu Onur, Murat Yildirim, Kaushik Subramanian, and Adela Ben-Yakar. "A 5-mm piezo-scanning fiber device for high speed ultrafast laser microsurgery." *Biomedical Optics Express* 5 (7) (2014): 2023-2036.

Onur Ferhanoglu designed and performed experiments. Murat Yildirim performed ultrashort pulse delivery through photonic bandgap fiber experiments. Kaushik Subramanian helped performing fiber characterization experiments. Adela Ben-Yakar supervised the project.

fiber lasers offer both high pulse energies and high repetition rates within a compact housing [159, 160]. These features make them ideal for high speed surgery, simultaneously providing imaging capabilities within a single laser unit as demonstrated in our recent benchtop studies [13, 54]. Together with the ability of hollow-core photonic crystal fibers to deliver more than hundreds of micro-Joules of pulse energies [58, 59], it is now feasible to build flexible and potentially hand-held laser scalpels suited for clinical use.

Clinical compatibility also requires further miniaturization of laser scalpel to reach small regions within the body. Relatively large size of packaging and die pieces that accompany MEMS scanners limit further miniaturization of our previously developed MEMS based probes to diameters below 7 – 8 mm. Alternatively, the compact geometry of piezo-scanning based probes has already been exploited in endoscopy for various optical imaging modalities, such as confocal imaging [225], optical coherence tomography [226], and multi-photon imaging [78, 88] to gain access to sites that are otherwise challenging to reach. Additionally, piezo- scanning would enable high optical transmission efficiencies not achievable in MEMS devices with silica based reflective surfaces, which is crucial for high pulse energies during surgery.

To perform high-speed surgery within confined spaces, we have, therefore, designed, developed, and rigorously characterized a new scalpel delivering high-repetition rate laser pulses from an erbium-doped fiber laser (1.5 ps, 300 kHz, 776 nm Discovery, Raydiance Inc.). By incorporating the piezo-scanning mechanism into an in-line optical architecture, we nearly halved the size of the device diameter compared to our previous MEMS based device, reducing its outer diameter to 5 mm. A high optical transmission efficiency further ensured delivery of the high energy pulses with low loss. This chapter presents the optical design of this piezo-scanning fiber device, the

characterization of its performance, and the high speed microsurgery of a scarred tissue sample. The device acts as a variable-width laser scalpel, with which a surgeon can precisely cut around tumor margins with precision. The scan-width can be altered anywhere from providing narrow cuts ($3 - 5 \mu\text{m}$ in width) to wide cuts (up to $220 \mu\text{m}$) for rapidly removing lesions on delicate tissue such as vocal fold ligaments. This chapter also presents an in-depth analysis of ultrashort pulse delivery through the air-core PBF and discussion of the associated limitations in delivering maximum pulse energies.

7.2: RESULTS

7.2.1: Device Design and Characterization

The selection of critical components for the new 5-mm scalpel involved the consideration of several factors with particular focus on: 1) reducing the device diameter below 5 mm, which is crucial to many clinical applications, 2) using optical components with low spherical aberration and high transmission at low-cost, 3) designing the optical system for a near- diffraction limited spot size through the entire field of view (FOV) while minimizing radius of curvature, 4) tight focusing to deliver high laser fluences for tissue ablation, 5) scanning a FOV of approximately $200 \mu\text{m} \times 200 \mu\text{m}$, and 6) performing microsurgery at high-speeds.

To maintain the housing diameter below 5 mm, we limited the maximum size of the optical components to 3 mm which meant moving away from the reflective beam steering MEMS scanning mechanisms from our earlier work. In this device, we chose an in-line optical architecture where beam steering is performed by the resonant vibration of a laser delivery fiber via a piezoelectric device. The in-line configuration also increased the transmission efficiency of the device by eliminating the poorly reflecting bare silicon surfaces of our previous MEMS scanning mirrors. Though reflectivity can be enhanced

with metal deposition onto the mirror surface, the use of fiber scanning mechanisms instead of a scanning mirror offers the highest efficiency in laser energy delivery in addition to enabling the smallest probe dimensions. For our optical components, we chose off-the-shelf glass molded aspheric lenses. With no spherical aberration and high optical transmission at our operating wavelengths, these lenses provided the high optical performance we were looking for at low cost.

The size of the FOV depends on the available scanning range of the fiber tip and the overall magnification of the optical system. In turn, the extended fiber length determines the extent of tip deflection and the resonant frequency of the setup. We estimated a maximum fiber tip scan range of $\pm 250 \mu\text{m}$ for a 10-mm extended fiber length, ensuring the tip deflection could safely be accomplished using low voltages with minimal hysteresis. The fiber resonance frequency for the chosen 10-mm extended length was calculated to be at $\sim 1 \text{ kHz}$, offering ablation speeds up to near 4 mm/s translational velocity for a 150 μm wide cut, as will be shown in the results. In a clinical setting, such speeds provide the ability for the surgeon to rapidly move the scalpel in one of the lateral directions without leaving unablated regions on the tissue.

The overall design of the scalpel is illustrated in Fig. 7.1 with the measured lateral and axial resolutions of the system. It consists of (1) a 7- μm , air-core PBF with mode field diameter (MFD) of 6 μm (NKT Photonics HC-800-02), (2) a piezoelectric tube actuator having a 3 mm outer diameter (Boston Piezo-Optics, PZT-5H) for fiber scanning, (3) an aspheric lens with 0.3 NA, 3.5 mm working distance, 3 mm outer diameter, and 2.8 mm clear aperture (Lightpath 354996 designed for 634 nm wavelength) for collimation of fiber output, and (4) an aspheric lens with 0.5 NA, 2 mm focal length, 3 mm outer diameter, and 2 mm clear aperture (Lightpath 352150 designed for 780 nm wavelength) for focusing on the tissue. To accommodate the tip deflection, we

specifically investigated lenses having 3 mm diameter to match the diameter of our piezo tube, while providing largest clear aperture possible without increasing the device diameter further than that imposed by the piezo actuator. The housing wall thickness was designed to be ~ 1 mm to satisfy our overall diameter target of 5 mm, meanwhile providing a sturdy framework for the miniaturized components.

To select the optical components and estimate the expected device performance, we modeled the surgery beam pathway using ZEMAX optical design software. Figure 7.1(a) shows simulated rays, launched from the fiber tip at two different locations: the blue line represents ray on the optical axis, red represents a ray at the edge of the clear aperture namely at the edge of the full scan range. Their centerline rays intersect with the optical axis at $1/3$ of the fiber length away from the fiber fixation point, in other words $2/3$ of the fiber length away from the fiber tip, as dictated by cantilever bending formulation [227]. The beam divergence at the fiber tip, represented by two outer rays, is considered to be at the measured fiber NA of 0.17 (Fig. 7.2(a)).

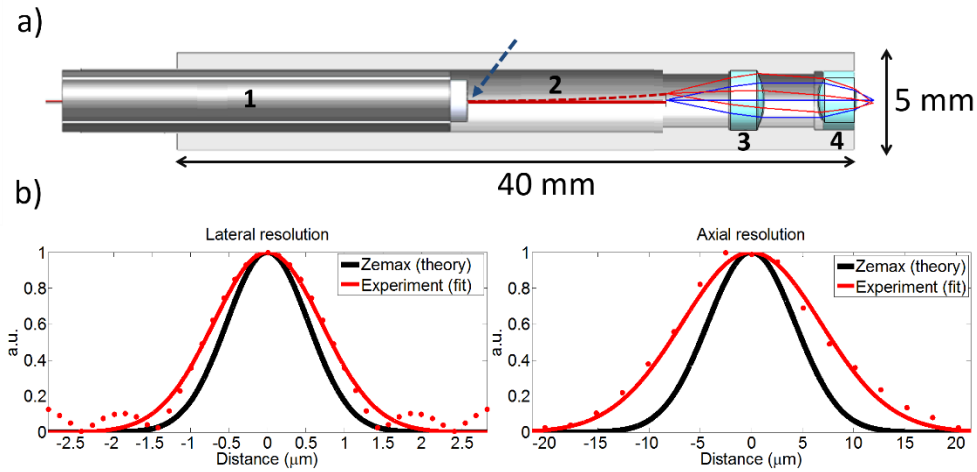


Figure 7.1. Optical architecture and resolution of the scalpel. a) A computer assisted drawing (CAD) of the scalpel consisting of 1 – piezo actuator tube, 2 – air core PBF, 3 – collimation lens, and 4 – objective, as overlaid with ZEMAX ray tracing diagram. Blue

arrow shows fiber fixation location. b) Measured and theoretical lateral and axial intensity distributions.

Simulations showed that a collimation lens with 0.3 NA and over 2 mm clear aperture (Lightpath 354996) could accommodate a fiber tip deflection up to $\pm 250 \mu\text{m}$ without vignetting. Among the available high NA lenses, we chose a 0.5 NA lens (Lightpath 352150) as the focusing lens that could provide tight focusing over a square FOV of $220 \mu\text{m} \times 220 \mu\text{m}$ for the maximum fiber tip deflection. Alternatively, we could choose a lens with a higher NA to achieve smaller spot size while compromising on the FOV and the working distance. Considering the curvature models of the lenses provided by the manufacturer, the ZEMAX simulation estimated the $1/e^2$ focused spot size to be $2.11 \mu\text{m}$ (Fig. 7.1(b)) at the optical axis with a Strehl ratio of 0.99. The aspheric lenses preserved the spot size during the scan, resulting in a Strehl ratio larger than 0.85 over the entire FOV. The radius of curvature of the FOV was 1.1 mm, mainly due to the fiber tip motion. This curvature corresponded to a $\pm 4 \mu\text{m}$ axial variation in the focal plane throughout the FOV from a planar surface. Furthermore, tolerance analysis on lenses and the fiber revealed that the resolution remained constant up to a $200 \mu\text{m}$ decenter and 2° tilt.

The housing was 40 mm long to hold all optical components in an in-line fashion. Its 5- mm outer diameter represents a near 50% reduction over our most recent MEMS-based endoscope with a 9.6 mm diameter [61]. The housing was 3-D printed via stereolithography technique, using DSM-Somos epoxy resin that mimics engineered plastics. With superior chemical resistance and broad heat and humidity tolerances, this material is a reliable and robust prototyping material for medical devices. The housing consisted of three grooves in which the rear side of the piezo tube and both lenses were

press-fitted. Press-fitting allowed for simple assembly of the scalpel. However the lack of positioning control limited the ability to adjust component alignment that could partially be mitigated by testing a few housing iterations with different dimensions.

To fit the PBF inside the piezo tube actuator, we used a 23 gauge steel tubing to hold the PBF. Steel tubing was then inserted inside a polyethylene tubing with matching diameter to the piezo tube. After cleaving the fiber, we adjusted the extended length to approximately 11 mm and glued it to the steel tubing. Three electrical wires were soldered to + x/+y electrodes and ground terminals of the piezo tube for single sided actuation. Both piezo channels were connected to a signal generator through voltage amplifiers. We placed the objective, after adjusting the distance between the piezo tube and the collimation lens using a micro- manipulator to ensure collimation.

After assembling all micro-optical components and the piezo actuator tube within the housing, we coupled the laser beam into a ~1 meter long PBF using an underfilled 0.25 NA objective and a 5-axes stage (Newport, 561 series). The overall optical transmission of the system was 59% as a result of losses at fiber coupling and slight misalignment of optical components within the device that partially clipped the beam.

To characterize the resolution of the scalpel, we placed an external objective across the device and monitored the laser transmission using a photodetector while moving the United States Air Force (USAF) resolution chart across the focus. The resolution was deduced by focusing the beam from the device on to the USAF chart profile with a 2.2 μm line width, and by deconvolving the experimental data. The deconvolution was performed in the Fourier domain by dividing the Fourier transform of the acquired experimental data to that of the USAF chart profile. Rectangular windowing was performed in the frequency domain to suppress frequencies with high noise which led to small ringing artifact. We verified our resolution calculation by convolving an ideal

Gaussian beam having equal width with that found from the deconvolution method and the USAF chart profile, which agreed well with the experimental data. These measurements matched well with knife-edge measurements within 2% difference.

At focus, the FWHM resolution was measured to be $1.64 \pm 0.05 \mu\text{m}$ and $16.21 \pm 0.05 \mu\text{m}$ in lateral and axial directions, respectively (Fig. 7.1(b)). The deduced resolutions reflect the mean and standard deviation for five different measurements. These resolutions correspond to intensity squared (two-photon) FWHM lateral and axial resolutions of $1.16 \pm 0.04 \mu\text{m}$ and $11.46 \pm 0.04 \mu\text{m}$, respectively, showing a 10% improvement over our previous probe in both axes [61]. The resulting lateral $1/e^2$ intensity width was $2.8 \pm 0.09 \mu\text{m}$, which is essential in estimating the average laser fluence at the focal plane and defining fluence thresholds for ablation. The measured lateral and axial resolutions were 30% and 60% higher than their corresponding ZEMAX results. As expected, the axial resolution showed a higher difference between measured and simulated values due to its quadratic dependence on NA, as opposed to a linear dependence on NA for the lateral resolution. Despite having slightly poorer axial resolution than expected, ray simulations revealed that the collimating and focusing lens formed a powerful pair that could accommodate a FOV up to $220 \mu\text{m} \times 220 \mu\text{m}$ without vignetting while maintaining near diffraction limited lateral resolution at all fiber scan angles.

7.2.2: Study of Maximum Pulse Energy Delivery Through the Air-Core Photonic Bandgap Fiber

The maximum energy that can be delivered using a single-mode, air-core PBF in our experimental conditions is expected to be limited by the ablation damage induced on the cladding by the tail of the propagating beam. This damage is likely to occur at the input face because of two general factors: 1) input energies are always higher than the

output energies due to coupling efficiencies that are lower than 100% and/or transmission losses through the fiber and 2) even slight misalignments during coupling can cause the Gaussian beam to shift off the center slightly both laterally and axially and cause damage on the cladding at lower energies than the perfectly centered beams.

To increase the pulse energy that can be coupled into an air-core PBF, pre-chirping can be used to increase the pulse duration at the coupling while fiber dispersion can compress the pulse duration back to its original value at the fiber exit. Since the damage threshold of silica depends on the pulse duration and longer pulses cause damage at higher laser fluences, one can deliver higher pulse energies into the fiber by pre-chirping them to longer pulses. We previously observed an increase of more than 3 times in delivered energy by pre-chirping a 10 nm bandwidth, 120 fs laser pulse into a 3.8 ps pulse [60]. The pulse could then be chirped back to near its original value as it propagated inside the fiber, experiencing negative dispersion. The limiting factor for maximum deliverable energies in this case was observed to be the damage at the input face of the 6 μm core size fiber. If a higher pre-chirping with a longer fiber was used or better coupling efficiencies could have been achieved, we could potentially deliver even higher pulse energies through the fiber. In that case, the ablation of the cladding could move somewhere along the fiber as the pulse compresses to shorter durations and increases its intensity. In the current study, however, the narrow bandwidth fiber-laser (3 nm) and the low dispersion of the fiber at the central laser wavelength, limited our pre-chirping capability.

There are other nonlinear mechanisms that can result in damaging the cladding and limit the maximum pulse energies deliverable through the PBFs. The high peak intensity of ultrafast laser pulses at the fiber core can induce a refractive index change in air due to the optical Kerr effect, arising from the third order nonlinear polarization.

Varying index of refraction results in the phase modulation of the beam both temporally as well as spatially. The temporal phase modulation results in self-phase modulation (SPM) that broadens the spectra in PBFs and shortens the pulse as it propagates along the fiber. Reducing the pulse duration below its original value, SPM can cause the ablation of the cladding to occur along the fiber, as the damage threshold fluence of silica reduces due to reduced pulse widths. The spatial modulation of the index of refraction, on the other hand, may result in catastrophic self-focusing in the air-core of the fibers leading to air-breakdown. Both SPM and self-focusing can be mitigated by replacing the air in the fiber core with gases having smaller nonlinear refractive indices [58]. The air-breakdown threshold of $\sim 10^{14}$ W/cm² [228] corresponds to more than 50 μ J pulse energy for all of the focusing conditions used in our experiments. In our setup, air breakdown is unlikely to be experienced because the maximum pulse energies that can ideally be delivered through the 7- μ m, air-core PBF is at least an order of magnitude smaller than this threshold. Therefore, we only considered the effect of SPM in our experiments.

To understand the maximum energy levels that could be delivered through the air-core PBF used in our miniaturized device, we therefore performed an in-depth study of the limiting parameters. Having eliminated the possibility of air breakdown in our experimental conditions, we focused on parameters effecting cladding damage and SPM. The cladding damage occurs when the fluence at the tail of the coupled beam right at the location of the cladding reaches the silica damage threshold. The laser fluence at the input facet cladding depends on the input pulse energy and the spot size and thus on the NA of the coupling lens, the diameter of the fiber core, as well as the profile of the focused beam. Moreover, system imperfections such as the pointing beam fluctuations and possible radial and axial misalignments during coupling can shift the focused beam and increase the laser fluence on the cladding at the fiber input face.

To study the NA effect on the maximum deliverable pulse energies, we tested three different coupling NA's of 0.18, 0.20, and 0.25 by over and under filling the back aperture of a 0.25 NA coupling lens (Fig. 7.2(a)). Different beam sizes at the back aperture was achieved by moving the coupling lens along the laser beam path. The measured spot sizes at the focal plane of the coupling lens were $6.2 \pm 0.4 \mu\text{m}$, $5.5 \pm 0.2 \mu\text{m}$, and $4.4 \pm 0.4 \mu\text{m}$, respectively (Fig. 7.2(b)). For each NA, we measured the maximum energy that could be delivered before a damage occurred at fiber input (Figs. 7.2(d) and 7.2(e)), as we did not observe any damage at the fiber output. During experiments, we defined fiber damage when the coupling efficiency dropped down by 20% of its maximum value. We successfully coupled maximum energies of 600 nJ, 765 nJ, and 850 nJ into the fiber with the corresponding output energies of 505 nJ, 705 nJ, and 660 nJ for NA's of 0.18, 0.20, and 0.25, respectively. These data points represent the average of three measurements performed at each NA with error bars representing the corresponding standard deviation. The highest coupling efficiency of more than 92% was observed for NA = 0.20, where the focused spot size of $5.5 \mu\text{m}$ best matched the fiber MFD of $6 \mu\text{m}$, as expected, delivering $> 700 \text{ nJ}$ laser energy at the fiber output. Coupling the laser at a higher NA enabled a higher input energy as the smaller laser spot size decreased the laser fluence interacting with the cladding. However, increasing the NA beyond the fiber's NA resulted in a mismatch of not only NA but also MFD that reduced coupling efficiency and thus reduced delivered energies at the output as evident in Fig. 7.2(e).

To better analyze the measured fiber delivery parameters, we estimated the maximum achievable energy at the input facet assuming various imperfections during coupling did not exist. We specifically considered three possible system imperfections, the radial and axial misalignments of the coupled beam and pointing beam fluctuations

inherent to the fiber laser. Radial misalignment and beam fluctuations would shift the focused beam location radially with respect to the optical axis of the fiber and axial misalignment will result in a larger beam size on the fiber input (Fig. 7.2(c)). As a result the laser fluence on the cladding will be increased for the same input energy. We therefore calculated the maximum pulse energies that could be delivered in the absence of each of these misalignments (Figs. 7.2(d) and 7.2(e)).

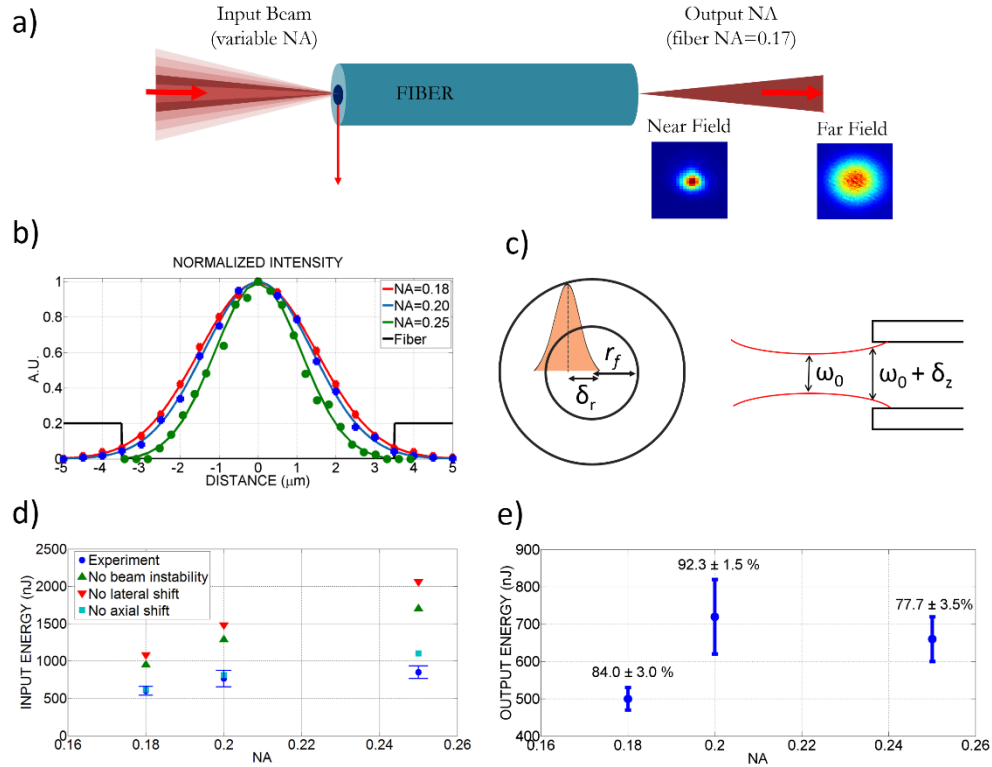


Figure 7.2. Effect of coupling NA, coupling misalignments, and beam pointing instabilities on delivered energy through the 7-μm, air-core PBF. a) Simplified schematic of ultrashort pulse delivery through the PBF with various focusing conditions and measured near-field and far- field profiles at fiber output. b) Beam profiles at the focal point of the coupling lens as measured using the knife-edge test for different NA's. c) Schematics illustrating the parameters for radial and axial coupling misalignments introduced in Eq. (1). d) Measured maximum input energies successfully coupled into the fiber for different coupling NA's and estimated maximum values assuming various misalignments during coupling. Error bars represent the standard deviation of three measurements performed at each NA. e) Measured output energies for each coupling NA

with the coupling efficiencies above each data point as calculated based on the ratio of observed output energy to the input energy after coupling lens.

First, we measured pointing beam fluctuations of the laser by focusing it with a long focal length lens ($f = 1 \text{ m}$) onto a high speed camera (VisionTech Phantom V series). By analyzing the beam profiles of 300,000 pulses (1 sec duration) that were collected every 10 minutes, we could measure how the centroid of each individual pulse moved over time. We found the centroid of each spot by first locating the maximum intensity in each image and then fitting a Gaussian curve for both x and y axis. We found that the centroid of the laser beam drifted in one direction continuously for the first 3 hours of operation. Once the drift ended, the centroid fluctuated in an elliptical shape, shifting $\pm 24 \text{ }\mu\text{m}$ along the long axis. The corresponding lateral shift of the beam at the focus of the 0.25 NA coupling lens with a 16.5 mm focal length was $\pm 0.4 \text{ }\mu\text{m}$.

We then calculated the threshold fluence at the tail of the beam on the cladding region (at $r = r_f$) for each coupling NA in the presence of estimated system imperfections. Assuming an ideal Gaussian beam distribution, the radial distribution of laser fluence is:

$$F(r) = \frac{2E}{\pi(w_0 + \delta z)^2} \exp\left(-2\left(\frac{r - \delta r}{w_0 + \delta z}\right)^2\right) \text{ thus; } F_{th} = F(r = r_f), \quad (7.1)$$

where F_{th} is the damage threshold of the silica fiber cladding, E is the observed maximum input energy at the fiber input face, w_0 is the measured radius of the beam waist for each NA (Fig. 7.2(b)), r is the radial distance, r_f is the fiber core radius as measured to be $3.5 \text{ }\mu\text{m}$ from SEM images in accordance with fiber specifications, δr is the total radial shift due to radial misalignments and beam fluctuations, and δz is the increase in spot size due to axial misalignments (Fig. 7.2(c)). In our system, the lateral misalignment was assumed to be due to the sensitivity of the fine adjustment knobs of the

fiber alignment stage ($0.5\ \mu\text{m}$) and the measured beam pointing fluctuations ($0.4\ \mu\text{m}$). The resulting δr became $0.9\ \mu\text{m}$. As for the axial misalignment of the beam, we assumed $\pm 10\ \mu\text{m}$ axial misalignment corresponding to half of the Rayleigh range of the coupling lens at 0.25 NA. The axial misalignment resulted in an increased beam size away from the beam waist in accordance with Gaussian beam formulation [229].

Taking these three imperfections into account, the damage thresholds were calculated to be similar for each NA as expected: 0.99 ± 0.03 , 1.15 ± 0.05 , and $0.97 \pm 0.1\ \text{J/cm}^2$ for NAs of 0.18, 0.20, and 0.25, respectively. These calculated damage thresholds are indeed close to that of silica, which happens to be in the range of $1.5 - 2\ \text{J/cm}^2$ [230]. We attributed the difference in our observed damage threshold as opposed to the bulk silica damage threshold to a combination of various effects, such as the incubation effect [231], possibly larger radial and axial misalignments during coupling than the presumed values, surface roughness [232] of the input facet of the fiber that may result in hot spots, as well as deviations of our beam profile from an ideal Gaussian beam.

With the calculated damage thresholds, we then projected the laser energy that could be coupled into the fiber by excluding one system imperfection at a time based on Eq. (1). Radial misalignments during coupling and the pointing beam instabilities were identified as the most crucial factors potentially reducing the amount of the maximum deliverable pulse energies significantly, before a damage in the fiber could occur. As illustrated in Fig. 7.2(d), in the absence of radial misalignment (lateral shift) alone, for example, we would have been able to couple about $2\ \mu\text{J}$ energy into the fiber.

To test the severity of SPM in our setup, we performed a set of experiments where we measured pulse width and spectral range for various input energies throughout a 20 cm fiber. For pulse energies in the 500 nJ range, the pulse duration decreased from 1.5 ps to 1.41 ps. Based on our measurements at various energy levels, we deduced the

nonlinear index of refraction of air (n_2) to be $2.7 \times 10^{23} \text{ m}^2/\text{W}$ using the formulation of change in spectral bandwidth with respect to pulse energy due to SPM [233]. Our findings were in close agreement with the measurements by Ouzounov et al., where they found $n_2 = 3 \times 10^{23} \text{ m}^2/\text{W}$ [234]. Using the measured nonlinear refractive index, a pulse width of 0.93 ps is estimated for the 1-m long fiber used in the scalpel. Although such shortening of pulse width would result in slight decrease of damage threshold, the beam instability and misalignment effects, highlighted earlier, were highly critical and dominant over the SPM in limiting the amount of delivered pulse energies through the 7- μm , air-core PBF. Therefore, we expected the damage of the fiber cladding to occur at the input facet, as opposed to a damage along the fiber due to shortening of pulse width.

The theoretical upper bound for the coupled energy was calculated to be 3.3 μJ by neglecting all three imperfections simultaneously at the optimal NA. According to the coupling efficiency of 92.5%, a maximum energy of 3.05 μJ could be delivered at fiber output. Although the input facet can withstand higher energies with a higher NA due to reduced spot size and thus lowered fluence at the cladding, the tightly focused spot will quickly match the fiber MFD as it couples, which will actually limit the coupled energy. We may therefore argue that the maximum energy calculated for optimal NA that matches MFD under perfect conditions serves as an upper bound for input energy, namely, slightly above 3 μJ deliverable energy given that the pulse duration of 1.5 ps is preserved. However, the theoretical maximum input energy of 3.3 μJ would create significant SPM, reducing the pulse width to 300 fs at the end of 1-m fiber. In this case, SPM would become dominant in damaging the fiber cladding over the damage caused due to the beam instability and misalignment effects. Considering 1.5 times lowered damage threshold at 300 fs as compared to 1.5 ps, the fiber will actually get damaged at

near 2.2 μJ as opposed to 3.3 μJ input energy. SPM would therefore set the ultimate limit on the deliverable energy through the fiber to approximately 2 μJ .

7.2.3: High Speed Ablation by Resonant Scanning

The ablation speed of our scalpel depends on fiber actuation dynamics and the repetition rate of the laser. To characterize the fiber actuation dynamics, we measured the resonance frequency of each axis and the resultant FOV for different applied peak voltages. The resonance frequency of the fiber depends on material properties of the fiber (Young's modulus and density) and its geometry (radius and extended length) [227]. By sweeping the frequency of the sinusoidal driving voltage while imaging the fiber tip deflection using a CCD camera, we measured the resonance frequencies to be 895 Hz and 904 Hz for the x and y axes, respectively. These frequencies were in close agreement with the theoretical value of 900 Hz that would be expected for the measured extended fiber length of 11 mm. Minor cross coupling between the axes were observed due to the close values of x and y resonance frequencies and also due to the off-centered position of the fiber with respect to the central axis of the piezo tube. Driving one axis at resonance resulted in the actuation of the orthogonal axis by an amount that was roughly seven times smaller in amplitude.

To characterize the size of the FOV, we imaged the scanned area at the focal volume onto a CCD camera for various peak voltages applied to both axes simultaneously at their resonance frequencies. A peak voltage of 20 volts, for example, created a scan area of $150\text{ }\mu\text{m} \times 150\text{ }\mu\text{m}$. This low voltage not only provides safe use of such laser scalpel within human body, but also enables the use of simple operational amplifiers that can reduce cost and complexity of the driving electronics. Through

driving all four electrodes, where $-x$ and $-y$ electrodes are phase reversed as opposed to $+x$ and $+y$ electrodes, the FOV can further be enlarged [235].

The successful implementation of ultrashort laser microsurgery in a clinic setting requires two essential parameters to be realized: 1) fast ablation speeds, so that the surgeon can move the FOV at clinically convenient speeds while achieving a continuous ablation and 2) a uniform ablation pattern that requires an equal number of overlapping pulses per spot over the entire FOV. To measure the speed and observe the pattern of ablation, we deposited a thin layer of gold on a cover glass and placed it at the focal plane of the device. Since the ablation threshold of gold is lower than that of the glass, we could tune the pulse energy to ablate only the gold film. This method enabled us to observe the direct signature of the ablation pattern and the size of the FOV for different laser exposure times.

Figure 7.3(a) presents optical images of the ablation pattern created on a 30 nm thick gold film on a glass sample for 100, 50, and 25 ms exposure times. We used pulse energies of 10 nJ, corresponding to an average fluence of 0.16 J/cm². This fluence level was expected to be sufficient to remove the thin gold layer with a single pulse. To estimate the ablation pattern, we simulated the expected Lissajous pattern within a 150 $\mu\text{m} \times 150 \mu\text{m}$ FOV, by taking into account fiber actuation resonance frequencies and pulse repetition rate. We considered the measured 1/e² spot size of 2.8 μm as the pixel size. Figure 7.3(b) shows the simulated binary ablation patterns, where each pixel that is sampled (ablated) at least once is indicated in green. Figure 7.3(c) reveals how many times each pixel is sampled within the FOV.

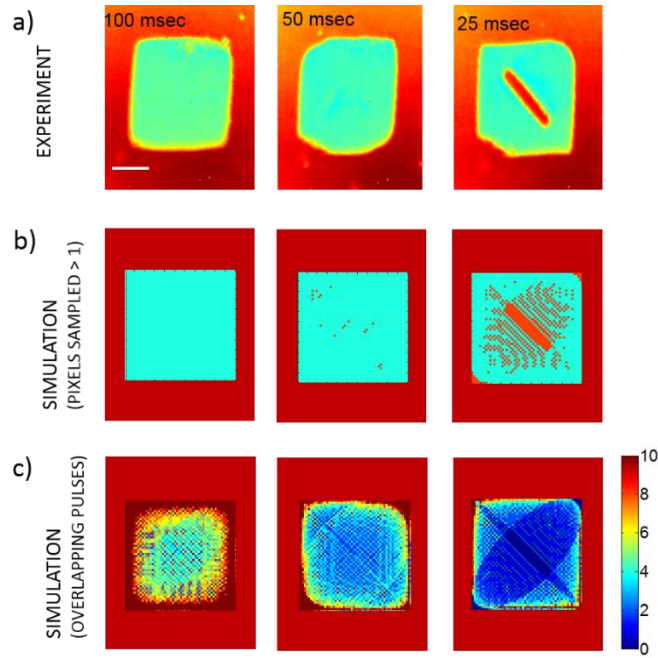


Figure 7.3. Ablation patterns at various laser exposure durations. a) Optical microscopy images of ablated gold film on glass slide for durations of 100 ms, 50 ms, and 25 ms. b) Simulated Lissajous patterns for all three durations within the experimental FOV of $150\ \mu\text{m} \times 150\ \mu\text{m}$, where pixels sampled at least once were marked in green and unsampled pixels were marked in orange. c) Simulation results indicating the number of overlapping pulses at each pixel. Scale bar is $50\ \mu\text{m}$.

The results indicated that 100%, 99%, and 79% of the pixels could be sampled for 100, 50, and 25 ms ablation durations, respectively. The pattern created over 50 ms demonstrated the most uniform number of overlapping pulses per spot over the FOV except at the corners. The sinusoidal nature of the Lissajous scan increased dwell times at the corners. All three simulated patterns qualitatively matched well the experimental observations. The period of the stable Lissajous pattern, which is the largest common divisor of both frequencies, was 1 Hz. Despite slow frame rate for obtaining a repeating Lissajous pattern, nearly 100% of the ablation spots could be sampled at least once within only 50 ms when operating with a 300 kHz repetition rate laser. The corresponding frame rate of 20 Hz indicates the potential for high-speed ablation with a fast updating and non-

repeating Lissajous pattern scanning opportunity [236]. Even with 25 ms ablation duration, only a small non-ablated area in the middle remained, showing a significant speed advantage for microsurgery. In this case also, the number of overlapping pulses were nearly uniform over the FOV with one or more pulses overlapping in more than 80% of the FOV.

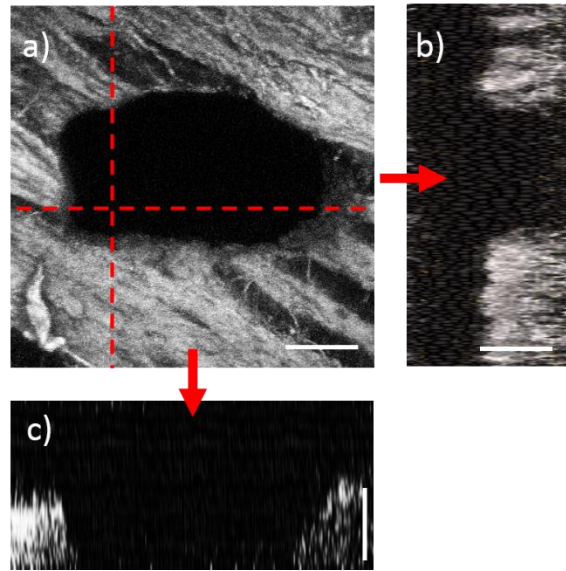


Figure 7.4. Ablation of tissue surface using the 5-mm laser scalpel. (a) Nonlinear image of the laser drill through a 70 μm thick cheek pouch sample as revealed by the absence of the SHG signal from the collagen fibers. (b) The x-z cross section of the vertical dashed line shown in (a). (c) The y-z cross section of the horizontal line shown in (a). The cross sections illustrate through ablation across the tissue thickness. The laser pulse energies were 200 nJ, corresponding to average fluences of 3.2 J/cm². Scale bars are 50 μm .

To test the capability of our scalpel to ablate tissue, we performed microsurgery on the surface of fixed tissue slices of a scarred hamster cheek pouch sample. The cheek pouch tissues were prepared at Massachusetts General Hospital Voice Laboratory in Boston by Dr. James Kobler and shipped on dry ice to our laboratory. After delivery, the cheek pouches were stored at $-80\text{ }^{\circ}\text{C}$. The details of this sample preparation are given in our previous publication [54]. The tissue was fixed by embedding into optimal cutting

temperature compound, which provides a convenient specimen matrix for cryostat sectioning at temperatures below -10°C . Fixation of the tissue allowed sectioning of the frozen tissue on a cryotome, which provided $70\text{ }\mu\text{m}$ thick tissue slices. For ablation experiments we have selected the slices below the epithelium where tissue collagen structure can be imaged using nonlinear imaging. Using 200 nJ pulse energies (average fluence of 3.2 J/cm^2), we were able to drill through a $70\text{ }\mu\text{m}$ thick slice within 10 seconds by moving the stage in the axial direction. Although fixed tissue was at room temperature during the experiment as opposed to body temperature that would be observed in a clinical setting, the difference in ablation thresholds between the two temperatures is negligible based on previous studies [237]. Prior to ablation, the surface was located by imaging the focused spot using a CCD camera. Once the surface was determined, we initiated the piezo-scanning with a targeted FOV of $150\text{ }\mu\text{m} \times 150\text{ }\mu\text{m}$ and manually translated the device towards the tissue to accomplish the drill. The ablation was performed with the energy level (350 nJ at fiber input) that is less than half the energy that would damage the fiber at the coupling NA of 0.2. The coupling efficiency values measured before and after the ablation matched, indicating that there was no damage on the cladding.

Figure 7.4 illustrates second harmonic generation (SHG) images of the ablated tissue. We acquired these images using a benchtop nonlinear microscope following the ablation with the scalpel. The SHG signal originated at the collagen fibers and the loss of this signal indicated the ablated areas. The images clearly showed that we have successfully drilled through the thin slice of tissue by moving the scalpel's axial stage back and forth. The backlash of the manual stage and the slight oblique angle between the tissue and the optical axis, caused the ablated area to come out to be slightly different than what was targeted.

7.3: DISCUSSION

In a surgical procedure, cutting speed varies greatly depending on the type of procedure, tissue, and the tool that is used for cutting. In general, applications that demand fast removal of non-fragile tissue such as bulk tumors, bones etc., benefit from high power lasers and mechanical removal tools. For instance, a high power CO₂ laser can ablate at great removal rates (>40 mm/s) [238] at the expense of significant collateral damage and a risk for carbonization. Mechanical cutting of tissue may also be performed at high speeds (~ 25 mm/s) [239], yet producing shear forces that results in a large border damage [240].

We estimated the tissue removal speed of our device through simulating a 2-D Lissajous pattern, with an additional linear translation term on one of the orthogonal directions in the lateral plane to model a tissue cut while translating the device at a constant speed (Fig. 7.5). We swept a number of velocity values till we achieved 100%, 90%, and 80% coverage within the ablated area. A translational speed of 2 mm/s allows the entire area to be ablated, where 100% of the pixels are sampled at least once. As we increased the translational speed to 3 mm/s and 3.7 mm/s, the percentage of pixels that are sampled at least once dropped down, as expected, to 90% and 80%, respectively. Such cutting speeds could still be adequate to tear the tissue. The ablation width of 150 μm matches the cut sizes achievable with mechanical scalpels and conventional CO₂ medical lasers having > 400 μm damage zone but with superior precisions in terms of the extent of the unwanted damage in the surrounding tissue [240].

Challenges in bringing an ultrafast laser ablation device to clinic lie in the ability to improve the laser energy that can be delivered to the tissue while conserving the alignment of the laser to the fiber during the operation. Throughout this study, we used an off-the shelf, low-cost PBF fiber with relatively high NA, which could be converted into

a large focusing NA at the tissue using a simple 2-lens optical design. Recent studies demonstrate transmission of high laser energies through novel large air-core Kagome fibers having low NA [59]. With further development, we aim to incorporate large air-core Kagome fibers to increase the amount of delivered energy for sub-epithelial ablation while utilizing smart optical designs to relay the low fiber NA to a high NA for focusing. However, when delivering higher pulse energies, one needs to be careful with SPM of the laser pulses that could potentially shift the damage along the fiber. We observed a slight narrowing of the pulse widths due to SPM in our experiments. However, the pointing beam instability and misalignment effects were more prominent than SPM and we observed damage at the input facet of our fiber.

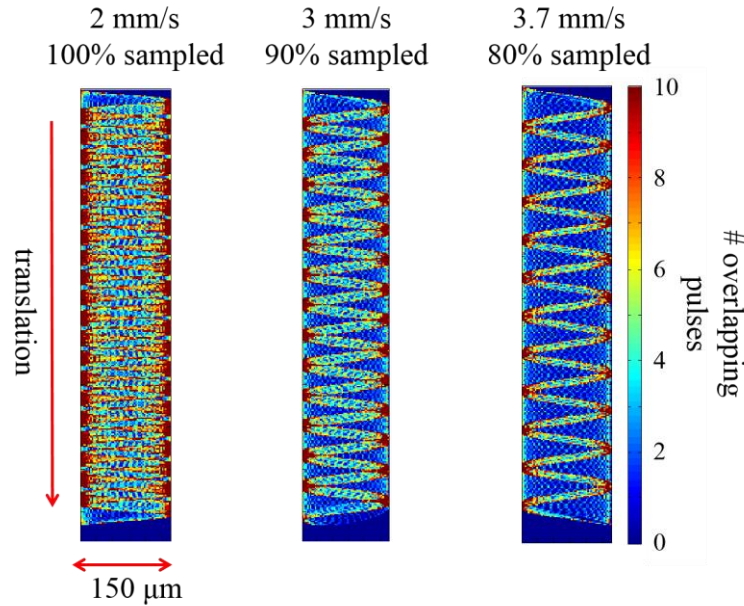


Figure 7.5. Effect of translation speed on ablation coverage. Translational speed of 2 mm/s results in complete ablation while 3 mm/s and 3.7 m/s provide 90% and 80% coverage, respectively.

Alignment of the laser in a clinical setting could be handled by a close-loop auto-alignment system. These systems are ideal for optimizing and maintaining free space

coupling of a laser into a single mode fiber. Though such systems cannot compensate for rapid changes in pointing vector, it can overcome laser drift on the fiber due to other factors such as environmentally induced vibrations and temperature fluctuations. Additionally, misalignment in fiber coupling will be significantly mitigated, owing to the very fine adjustment sensitivity of the auto-alignment system in 3D.

The current device was designed as a surgery tool only, to remove tissues that can be located with visual inspection. Nevertheless, the device will eventually adopt various linear and nonlinear imaging modalities. With imaging capability, the device will be able to image in real-time, likewise our previous endoscope using a computer controlled data acquisition routine. The imaging capability will enable the clinician to rapidly locate the surface, epithelial, and sub-epithelial tissue layers via a manipulator on which the device is attached. Such a manipulator could either be controlled by the clinician or interfaced with haptic technology that converts the motion of the clinicians hand into micrometric movements of the device.

7.4: CONCLUSIONS

In this study, we developed a piezo-scanned fiber device for high speed ultrafast laser microsurgery, with an overall diameter of 5 mm. While the diameter of the scalpel is now half of our latest probe, its resolution has been also improved by 10% in both lateral and axial directions. The use of a high repetition rate fiber laser, delivering 300,000 pulses per second, and utilizing a sub-frame rate Lissajous scanning approach provided high ablation speeds suitable for clinical use. As shown by the uniform ablation of gold samples, an ablation FOV of $150\text{ }\mu\text{m} \times 150\text{ }\mu\text{m}$ could be achieved within only 50 ms. With such ablation speeds, drilling into a cheek pouch tissue was possible using pulse energies of 200 nJ (3.2 J/cm^2). With these speeds the surgeon could potentially move the

surgery probe at speeds near 4 mm/s laterally in one direction while continuously removing a 150 μm wide tissue layer.

With its improved resolution, smaller size, and surgical speed, our scalpel can be particularly useful for scarred vocal fold treatment, where we aim to create ablation voids to improve localization of injected biomaterials to restore vocal fold viscoelasticity [13, 54]. Our laser scalpel can provide up to 450 nJ pulse energy, corresponding to 7.4 J/cm² fluence at the tissue. Having around 100 μm epithelial thickness [241], the complete ablation of sub-epithelial void in scarred human vocal folds will require fluences of more than 16 J/cm², higher than what this scalpel can deliver [54]. With its current ablative capability, the device would be useful in precisely dissecting around epithelial carcinoma sections. We were able to ablate a 70 μm deep trench, indicating that we could conveniently ablate greater depths by moving the device axially.

The major limitation in delivering higher pulse energies is identified to be the cladding damage at the input facet of the fiber. This limitation can potentially be mitigated by reducing the radial and axial misalignments, laser pointing beam fluctuations, and deviations of our beam profile from an ideal Gaussian beam. With the addition of imaging capability, our device can also serve as a useful tool for image-guided surgery in the oral cavity, larynx, colon, prostate, and open surgical sites.

Chapter 8: Conclusion

As illustrated in the preceding chapters, femtosecond laser pulses achieve unrivaled microsurgical precision by developing extremely high peak intensity with relatively low total pulse energy. Despite a wide range of clinical advantages and applications that have been identified in bench-top studies, clinical development of femtosecond laser microsurgery outside of ophthalmology has remained in its infancy. The lack of a means to flexibly deliver the high-intensity laser light to areas of interest and guide it with suitable precision has constituted a serious hurdle to further clinical development. In response, this dissertation has detailed my research and development of table-top systems and the fiber-coupled femtosecond laser microsurgery scalpel to treat vocal fold scarring which does not have any reliable treatment in the clinic.

First, we studied laser ablation parameters for creation of sub-epithelial voids in vocal folds and how these parameters varied in scar tissue using animal models. We specifically investigated the differences in tissue architecture and scattering properties, and their relation to ablation thresholds and bubble lifetime. By using nonlinear imaging, we analyzed tissue architecture and bubble dynamics. By developing a new method, we measured the ablation threshold below tissue surface while simultaneously extracting the extinction properties of different tissue layers. Also, we studied how the mechanical properties as interpreted from the nonlinear images could be related to the observed differences in the ablation characteristics and bubble lifetime.

Second, we performed in-depth analysis using numerical, analytical, and experimental techniques to understand the limitation of maximum imaging depths with third-harmonic generation microscopy in turbid tissues such as vocal folds compared to two-photon autofluorescence microscopies. Our experimental results revealed that

maximum imaging depth improved significantly from 140 μm to 420 μm using THG microscopy at 1552 nm excitation wavelength as compared to TPM at 776 nm. This maximum imaging depth improvement was a direct result of the increased total extinction length and reduced out-of-focus signal resulting from three-photon processes. Another important contribution of this in-depth analysis was to understand how to avoid thermal heating during THG imaging at 1552 nm excitation wavelength. By performing surface temperature measurements, optimizing the repetition rate of the laser, and modeling tissue temperature as a function of depth, we avoided tissue heating. We characterized the thermal relaxation time of tissue with different imaging powers and utilized this relaxation time to estimate the depth resolved temperature distribution. The experimental and theoretical thermal relaxation times (~ 15 s) correlated well with each other, implying that the optical and thermal tissue properties used were accurate. Then, we developed a numerical algorithm where the intensity distribution inside the tissue was determined by the Radiative Transport Equation (RTE) and the temperature distribution estimated by coupling the Pennes Bioheat equation with a non-Fourier damped heat conduction equation. By shuttering the laser beam for 30 s between consecutive imaging planes we avoided heating and kept a maximum temperature increase of less than 2°C inside the tissue. Such temperature control avoided thermal damage to the tissue, which made THG imaging at 1552 nm wavelength safe to use. Overall, with effective thermal management, the threefold improvement in maximum imaging depth presented here will guide development of turn-key femtosecond fiber laser-assisted treatment methods for sub-epithelial image guided surgeries, similar to the proposed scarred vocal folds treatments currently under development in our lab.

Third, we assessed the potential of an automated SHG image analysis method to differentiate normal and scarred hamster cheek pouch samples by quantifying collagen

fiber direction and density. With this method, one could track the development of vocal fold scar in vivo or follow the effects of scarring-related treatments due to the analogous anatomical organization of the tissue layers between the hamster cheek pouch and vocal folds. We utilized Fourier-based methods and intensity thresholding to determine collagen fiber directional variance and density, respectively. The resultant depth-resolved average fiber direction variance was 0.732 ± 0.041 for control and 0.606 ± 0.025 for scarred hamster cheek pouches, respectively. This analysis showed that the fiber direction in scarred samples was less random than in control samples. Depth-resolved collagen fiber density was 0.178 ± 0.025 for control and 0.721 ± 0.090 for scarred tissues, respectively. This four-fold difference in collagen fiber density demonstrated, as expected, that the average fiber densities in scarred tissues were remarkably higher than that in control tissues. The method we presented here will guide development of testing scar treatments such as biomaterials, and turn-key ultrafast fiber laser-assisted treatment methods for sub-epithelial image guided surgeries, similar to proposed scarred vocal folds treatments currently under development in our lab.

Fourth, we developed a novel drug-delivery method to inject and localize PEG 30 biomaterial inside sub-epithelial voids created by ultra-short laser pulses within scarred cheek pouch samples. To demonstrate the feasibility of this technique, we developed a semi-automated system to control and monitor the diffusion of the biomaterial inside scarred hamster cheek pouch samples. In addition to this semi-automated system, we utilized our home-built upright laser-scanning microscope to perform nonlinear imaging guided ultrafast laser ablation. We optimized the biomaterial flow rate parameters such as air pressure and exposure time to have required biomaterial volume in a reasonable time. Our results reveal that the optimized experimental conditions become 20-psi air pressure and 10-25 ms exposure time. After this characterization, we first performed biomaterial

injection to the scarred tissue samples without any sub-epithelial void to examine the clinical challenge. We observed a back-flow of the injected biomaterial along the point of injection and this condition prevented localization of the biomaterial at the desired locations. In contrast to the biomaterial injection outcomes without any voids, the presence of sub-epithelial voids greatly reduced back-flow at the injection site and resulted in a lasting localization of the injected biomaterial at different locations of the tissue. We also performed a follow-up H&E histology and realized that the location and appearance of the biomaterial correlated well with TPAF and SHG in-situ nonlinear images. Since the direct injection of the biomaterials into the scarred vocal folds is challenging due to presence of highly stiffened scar tissue, we believe that creation of thin sub-epithelial voids assisted with nonlinear imaging guidance by ultrafast lasers can ease the injection and localization of the biomaterials to restore the mechanical functionality of the vocal folds. This novel method we presented here will guide development of turn-key ultrafast fiber laser-assisted treatment methods for sub-epithelial image guided surgeries, similar to the proposed scarred vocal folds treatments currently under development in our lab.

Finally, we developed a piezo-scanned fiber device for high speed ultrafast laser microsurgery, with an overall diameter of 5 mm. While the diameter of the scalpel is now half of our latest probe, its resolution has been also improved by 10% in both lateral and axial directions. The use of a high repetition rate fiber laser, delivering 300,000 pulses per second, and utilizing a sub-frame rate Lissajous scanning approach provided high ablation speeds suitable for clinical use. As shown by the uniform ablation of gold samples, an ablation FOV of $150\text{ }\mu\text{m} \times 150\text{ }\mu\text{m}$ could be achieved within only 50 ms. With such ablation speeds, drilling into a cheek pouch tissue was possible using pulse energies of 200 nJ (3.2 J/cm^2). With these speeds the surgeon could potentially move the

surgery probe at speeds near 4 mm/s laterally in one direction while continuously removing a 150 μm wide tissue layer.

With its improved resolution, smaller size, and surgical speed, our scalpel can be particularly useful for scarred vocal fold treatment, where we aim to create ablation voids to improve localization of injected biomaterials to restore vocal fold viscoelasticity. Our laser scalpel can provide up to 450 nJ pulse energy, corresponding to 7.4 J/cm² fluence at the tissue. Having around 100 μm epithelial thickness, the complete ablation of sub-epithelial void in scarred human vocal folds will require fluences of more than 16 J/cm², higher than what this scalpel can deliver. With its current ablative capability, the device would be useful in precisely dissecting around epithelial carcinoma sections. We were able to ablate a 70 μm deep trench, indicating that we could conveniently ablate greater depths by moving the device axially.

The major limitation in delivering higher pulse energies is identified to be the cladding damage at the input facet of the fiber. Reducing the radial and axial misalignments, laser pointing beam fluctuations, and deviations of our beam profile from an ideal Gaussian beam can potentially mitigate this limitation. With the addition of imaging capability, our device can also serve as a useful tool for image-guided surgery in the oral cavity, larynx, colon, prostate, and open surgical sites.

The potential for combined surgical guidance using the same laser system for nonlinear optical imaging may also drive new applications, such as in neurosurgery with myelin-specific THG imaging. We have highlighted one such application, the creation of sub-epithelial voids for treatment of scarred vocal folds, which fits both of these criteria. Using ultrafast lasers for both surgery and image guidance, we have shown here that the ultrafast lasers can be used to greatly enhance the localization and retention of injected biomaterials used for treating vocal fold scars.

As new clinical applications are developed, ultrafast laser technology will need to develop alongside them. The size, cost, robustness, and speed of ultrafast laser systems have all improved significantly since their invention, particularly in the case of fiber lasers. Current ultrafast laser systems typically provide repetition rates in the many hundreds of kilohertz to single megahertz range, enabling faster surgical cutting and reasonable imaging times. Meanwhile, such systems deliver pulse durations frequently in the many hundreds of femtoseconds to few picoseconds, which is a desirable range for limiting the effects of self-focusing and thus ablating deeper in tissue. In addition to the lasers themselves, many applications require small and flexible delivery of the ultrafast laser light. Such delivery is possible without sacrificing the quality of the nonlinear ablation or the potential of inline image guidance through the use of photonic crystal fibers and miniaturized optical probes.

As these applications and technologies develop in the coming years, ultrafast lasers have the potential to provide many new clinical solutions and enable creative medical treatments as yet unimagined.

References

1. Hirano, S., *Current treatment of vocal fold scarring*. Curr Opin Otolaryngol Head Neck Surg, 2005. **13**(3): p. 143-7.
2. Ramig, L.O. and K. Verdolini, *Treatment efficacy: voice disorders*. J Speech Lang Hear Res, 1998. **41**(1): p. S101-16.
3. Bartlett, R.S., S.L. Thibeault, and G.D. Prestwich, *Therapeutic potential of gel-based injectables for vocal fold regeneration*. Biomed Mater, 2012. **7**(2): p. 024103.
4. Hahn, M.S., et al., *Collagen composite hydrogels for vocal fold lamina propria restoration*. Biomaterials, 2006. **27**(7): p. 1104-9.
5. Jia, X., et al., *Hyaluronic acid-based microgels and microgel networks for vocal fold regeneration*. Biomacromolecules, 2006. **7**(12): p. 3336-44.
6. Zeitels, S.M., et al., *Foresight in laryngology and laryngeal surgery: a 2020 vision*. Ann Otol Rhinol Laryngol Suppl, 2007. **198**: p. 2-16.
7. Zeitels, S.M. and G.B. Healy, *Laryngology and phonosurgery*. N Engl J Med, 2003. **349**(9): p. 882-92.
8. Hirano, M., *Morphological structure of the vocal cord as a vibrator and its variations*. Folia Phoniatrica et Logopaedica, 1974. **26**(2): p. 89-94.
9. Prades, J.M., et al., *Lamina propria of the human vocal fold: histomorphometric study of collagen fibers*. Surg Radiol Anat, 2010. **32**(4): p. 377-82.
10. Hammond, T.H., et al., *The intermediate layer: a morphologic study of the elastin and hyaluronic acid constituents of normal human vocal folds*. J Voice, 1997. **11**(1): p. 59-66.
11. Burns, J.A., et al., *Real-time tracking of vocal fold injections with optical coherence tomography*. Laryngoscope, 2009. **119**(11): p. 2182-6.
12. Karajanagi, S.S., et al., *Assessment of canine vocal fold function after injection of a new biomaterial designed to treat phonatory mucosal scarring*. Ann Otol Rhinol Laryngol, 2011. **120**(3): p. 175-84.
13. Hoy, C.L., et al., *Towards endoscopic ultrafast laser microsurgery of vocal folds*. J Biomed Opt, 2012. **17**(3): p. 038002.
14. Maiman, T.H., *Stimulated Optical Radiation in Ruby*. Nature, 1960. **187**(4736): p. 493-494.
15. Townes, C.H., *Optical masers and their possible applications in biology*. Biophysics Journal, 1962. **2**(2): p. 325.
16. Amy, R.L. and R. Storb, *Selective Mitochondrial Damage by a Ruby Laser Microbeam - an Electron Microscopic Study*. Science, 1965. **150**(3697): p. 756-&.
17. Bessis, M. and G. Nomarski, *Irradiation Ultra-Violette Des Organites Cellulaires Avec Observation Continue En Contraste De Phase*. J Biophys Biochem Cytol, 1960. **8**(3): p. 777-91.

18. Saks, N.M. and C.A. Roth, *Ruby Laser as a Microsurgical Instrument*. Science, 1963. **141**(357): p. 46-&.
19. Berns, M.W., R.S. Olson, and D.E. Rounds, *In Vitro Production of Chromosomal Lesions with an Argon Laser Microbeam*. Nature, 1969. **221**(5175): p. 74-&.
20. Zaret, M.M., et al., *Ocular Lesions Produced by an Optical Maser (Laser)*. Science, 1961. **134**(348): p. 1525-&.
21. Goldman, L., et al., *Pathology of the effect of the laser beam on the skin*. Nature, 1963. **197**: p. 912-4.
22. Goldman, L., et al., *Impact of the Laser on Dental Caries*. Nature, 1964. **203**: p. 417.
23. Magidson, V., et al., *Laser microsurgery in the GFP era: a cell biologist's perspective*. Methods Cell Biol, 2007. **82**: p. 239-66.
24. Munnerlyn, C.R., *Lasers in ophthalmology: past, present and future*. Journal of Modern Optics, 2003. **50**(15-17): p. 2351-2360.
25. Tanzi, E.L., J.R. Lupton, and T.S. Alster, *Lasers in dermatology: Four decades of progress*. Journal of the American Academy of Dermatology, 2003. **49**(1): p. 1-31.
26. Ossoff, R.H., et al., *Clinical-Applications of Lasers in Otolaryngology - Head and Neck-Surgery*. Lasers in Surgery and Medicine, 1994. **15**(3): p. 217-248.
27. Vogel, A. and V. Venugopalan, *Mechanisms of pulsed laser ablation of biological tissues (vol 103, pg 577, 2003)*. Chemical Reviews, 2003. **103**(5): p. 2079-2079.
28. Bass, L.S. and M.R. Treat, *Laser tissue welding: A comprehensive review of current and future clinical applications*. Lasers in Surgery and Medicine, 1995. **17**(4): p. 315-349.
29. Joglekar, A.P., et al., *Optics at critical intensity: Applications to nanomorphing*. Proceedings of the National Academy of Sciences of the United States of America, 2004. **101**(16): p. 5856-5861.
30. Vogel, A., et al., *Mechanisms of femtosecond laser nanosurgery of cells and tissues*. Applied Physics B-Lasers and Optics, 2005. **81**(8): p. 1015-1047.
31. Ben-Yakar, A. and F. Bourgeois, *Ultrafast laser nanosurgery in microfluidics for genome-wide screenings*. Current Opinion in Biotechnology, 2009. **20**(1): p. 100-105.
32. Bourgeois, F. and A. Ben-Yakar, *Femtosecond laser nanoaxotomy properties and their effect on axonal recovery in C-elegans*. Optics Express, 2007. **15**(14): p. 8521-8531.
33. Vogel, A., et al., *Energy balance of optical breakdown in water at nanosecond to femtosecond time scales*. Applied Physics B-Lasers and Optics, 1999. **68**(2): p. 271-280.
34. Vogel, A., et al., *Plasma formation in water by picosecond and nanosecond Nd:YAG laser pulses. I. Optical breakdown at threshold and superthreshold irradiance*. Selected Topics in Quantum Electronics, IEEE Journal of, 1996. **2**(4): p. 847-860.

35. Noack, J. and A. Vogel, *Laser-induced plasma formation in water at nanosecond to femtosecond time scales: Calculation of thresholds, absorption coefficients, and energy density*. Ieee Journal of Quantum Electronics, 1999. **35**(8): p. 1156-1167.
36. Oraevsky, A.A., et al., *Plasma mediated ablation of biological tissues with nanosecond-to-femtosecond laser pulses: Relative role of linear and nonlinear absorption*. Ieee Journal of Selected Topics in Quantum Electronics, 1996. **2**(4): p. 801-809.
37. Peng, C., R.E. Palazzo, and I. Wilke, *Laser intensity dependence of femtosecond near-infrared optoinjection*. Physical Review E, 2007. **75**(4).
38. Tirlapur, U.K. and K. Konig, *Cell biology - Targeted transfection by femtosecond laser*. Nature, 2002. **418**(6895): p. 290-291.
39. Konig, K., et al., *Femtosecond laser nanoprocessing using near-infrared nanojoule pulses at MHz repetition frequency*. Optics/Photonics in Security and Defence. International Society for Optics and Photonics,, 2006.
40. Shen, N., et al., *Ablation of cytoskeletal filaments and mitochondria in live cells using a femtosecond laser nanoscissor*. Mech. Chem. Biosyst., 2005. **2**(1): p. 17-25.
41. Chung, S.H., et al., *The role of the AFD neuron in C-elegans thermotaxis analyzed using femtosecond laser ablation*. BMC Neuroscience, 2006. **7**.
42. Yanik, M.F., et al., *Neurosurgery: functional regeneration after laser axotomy*. Nature, 2004. **432**(7019): p. 822.
43. Nishimura, N., et al., *Tissue ablation with 100-fs and 200-ps laser pulses*. Proceedings of the 20th Annual International Conference of the Ieee Engineering in Medicine and Biology Society, Vol 20, Pts 1-6, 1998. **20**: p. 1703-1706.
44. Loesel, F.H., et al., *Non-thermal ablation of neural tissue with femtosecond laser pulses*. Applied Physics B-Lasers and Optics, 1998. **66**(1): p. 121-128.
45. Neev, J., et al., *Ultrashort pulse lasers for hard tissue ablation*. Ieee Journal of Selected Topics in Quantum Electronics, 1996. **2**(4): p. 790-800.
46. Ratkay-Traub, I., et al., *First clinical results with the femtosecond neodymium-glass laser in refractive surgery*. Journal of Refractive Surgery, 2003. **19**(2): p. 94-103.
47. Denk, W., J.H. Strickler, and W.W. Webb, *Two-photon laser scanning fluorescence microscopy*. Science, 1990. **248**(4951): p. 73-6.
48. Moreaux, L., et al., *Membrane imaging by simultaneous second-harmonic generation and two-photon microscopy: errata*. Opt Lett, 2000. **25**(9): p. 678.
49. So, P.T., et al., *Two-photon excitation fluorescence microscopy*. Annu Rev Biomed Eng, 2000. **2**: p. 399-429.
50. Zipfel, W.R., R.M. Williams, and W.W. Webb, *Nonlinear magic: multiphoton microscopy in the biosciences*. Nat Biotechnol, 2003. **21**(11): p. 1369-77.
51. Konig, K., et al., *First in vivo animal studies on intraocular nanosurgery and multiphoton tomography with low-energy 80-MHz near-infrared femtosecond laser pulses*. International Society for Optics and Photonics, 2004: p. 262-269.

52. Sacconi, L., et al., *Combined intracellular three-dimensional imaging and selective nanosurgery by a nonlinear microscope*. J Biomed Opt, 2005. **10**(1): p. 14002.
53. Wang, B.G., et al., *Multiphoton microscopy for monitoring intratissue femtosecond laser surgery effects*. Lasers Surg Med, 2007. **39**(6): p. 527-33.
54. Yildirim, M., et al., *Parameters affecting ultrafast laser microsurgery of subepithelial voids for scar treatment in vocal folds*. J Biomed Opt, 2013. **18**(11): p. 118001.
55. Clark, S.W., F.O. Ilday, and F.W. Wise, *Fiber delivery of femtosecond pulses from a Ti:sapphire laser*. Opt Lett, 2001. **26**(17): p. 1320-2.
56. Helmchen, F., D.W. Tank, and W. Denk, *Enhanced two-photon excitation through optical fiber by single-mode propagation in a large core*. Applied Optics, 2002. **41**(15): p. 2930-2934.
57. Gobel, W., A. Nimmerjahn, and F. Helmchen, *Distortion-free delivery of nanojoule femtosecond pulses from a Ti : sapphire laser through a hollow-core photonic crystal fiber*. Optics Letters, 2004. **29**(11): p. 1285-1287.
58. Peng, X., M. Mielke, and T. Booth, *High average power, high energy 1.55 μ m ultra-short pulse laser beam delivery using large mode area hollow core photonic band-gap fiber*. Optics Express, 2011. **19**(2): p. 923-932.
59. Wang, Y.Y., et al., *Design and fabrication of hollow-core photonic crystal fibers for high-power ultrashort pulse transportation and pulse compression*. Optics Letters, 2012. **37**(15): p. 3111-3113.
60. Hoy, C.L., et al., *Miniaturized probe for femtosecond laser microsurgery and two-photon imaging*. Opt Express, 2008. **16**(13): p. 9996-10005.
61. Hoy, C.L., et al., *Optical design and imaging performance testing of a 9.6-mm diameter femtosecond laser microsurgery probe*. Opt Express, 2011. **19**(11): p. 10536-52.
62. Theer, P. and W. Denk, *On the fundamental imaging-depth limit in two-photon microscopy*. Journal of the Optical Society of America a-Optics Image Science and Vision, 2006. **23**(12): p. 3139-3149.
63. Theer, P., M.T. Hasan, and W. Denk, *Two-photon imaging to a depth of 1000 μ m in living brains by use of a Ti : Al₂O₃ regenerative amplifier*. Optics Letters, 2003. **28**(12): p. 1022-1024.
64. Freund, I. and M. Deutsch, *Second-harmonic microscopy of biological tissue*. Opt Lett, 1986. **11**(2): p. 94.
65. Skala, M.C., et al., *In vivo multiphoton microscopy of NADH and FAD redox states, fluorescence lifetimes, and cellular morphology in precancerous epithelia*. Proc Natl Acad Sci U S A, 2007. **104**(49): p. 19494-9.
66. Leppert, J., et al., *Multiphoton excitation of autofluorescence for microscopy of glioma tissue*. Neurosurgery, 2006. **58**(4): p. 759-67; discussion 759-67.
67. Lin, S.J., et al., *Discrimination of basal cell carcinoma from normal dermal stroma by quantitative multiphoton imaging*. Opt Lett, 2006. **31**(18): p. 2756-8.

68. Skala, M.C., et al., *Multiphoton microscopy of endogenous fluorescence differentiates normal, precancerous, and cancerous squamous epithelial tissues*. Cancer Res, 2005. **65**(4): p. 1180-6.
69. Wilder-Smith, P., et al., *In vivo multiphoton fluorescence imaging: a novel approach to oral malignancy*. Lasers Surg Med, 2004. **35**(2): p. 96-103.
70. Durr, N.J., et al., *Two-photon luminescence imaging of cancer cells using molecularly targeted gold nanorods*. Nano Letters, 2007. **7**(4): p. 941-945.
71. Wang, H., et al., *In vitro and in vivo two-photon luminescence imaging of single gold nanorods*. Proc Natl Acad Sci U S A, 2005. **102**(44): p. 15752-6.
72. Stosiek, C., et al., *In vivo two-photon calcium imaging of neuronal networks*. Proceedings of the National Academy of Sciences of the United States of America, 2003. **100**(12): p. 7319-7324.
73. Denk, W., et al., *Anatomical and Functional Imaging of Neurons Using 2-Photon Laser-Scanning Microscopy*. Journal of Neuroscience Methods, 1994. **54**(2): p. 151-162.
74. Ameer-Beg, S.M., et al., *Application Of Multiphoton steady state and lifetime imaging to mapping of tumour vascular architecture in vivo*. Multiphoton Microscopy in the Biomedical Sciences II, 2002. **4620**: p. 85-95.
75. Brown, E.B., et al., *In vivo measurement of gene expression, angiogenesis and physiological function in tumors using multiphoton laser scanning microscopy (vol 7, pg 864, 2001)*. Nature Medicine, 2001. **7**(9): p. 1069-1069.
76. Levene, M.J., et al., *In vivo multiphoton microscopy of deep brain tissue*. Journal of Neurophysiology, 2004. **91**(4): p. 1908-1912.
77. Helmchen, F., et al., *A miniature head-mounted two-photon microscope: High-resolution brain imaging in freely moving animals*. Neuron, 2001. **31**(6): p. 903-912.
78. Engelbrecht, C.J., et al., *Ultra-compact fiber-optic two-photon microscope for functional fluorescence imaging in vivo*. Optics Express, 2008. **16**(8): p. 5556-5564.
79. Flusberg, B.A., et al., *In vivo brain imaging using a portable 3.9 gram two-photon fluorescence microendoscope*. Optics Letters, 2005. **30**(17): p. 2272-2274.
80. Gobel, W., et al., *Miniaturized two-photon microscope based on a flexible coherent fiber bundle and a gradient-index lens objective*. Optics Letters, 2004. **29**(21): p. 2521-2523.
81. Jung, J.C. and M.J. Schnitzer, *Multiphoton endoscopy*. Optics Letters, 2003. **28**(11): p. 902-904.
82. Piyawattanametha, W., et al., *In vivo brain imaging using a portable 2.9 g two-photon microscope based on a microelectromechanical systems scanning mirror*. Optics Letters, 2009. **34**(15): p. 2309-2311.
83. Fu, L., et al., *Three-dimensional nonlinear optical endoscopy*. Journal of Biomedical Optics, 2007. **12**(4).
84. Kyrish, M. and T.S. Tkaczyk, *Achromatized endomicroscope objective for optical biopsy*. Biomedical Optics Express, 2013. **4**(2): p. 287-297.

85. Kyrish, M., et al., *Ultra-slim plastic endomicroscope objective for non-linear microscopy*. Optics Express, 2011. **19**(8): p. 7603-7615.
86. Myaing, M.T., D.J. MacDonald, and X.D. Li, *Fiber-optic scanning two-photon fluorescence endoscope*. Optics Letters, 2006. **31**(8): p. 1076-1078.
87. Ouzounov, D.G., et al., *Dual modality endomicroscope with optical zoom capability*. Biomedical Optics Express, 2013. **4**(9): p. 1494-1503.
88. Zhang, Y.Y., et al., *A compact fiber-optic SHG scanning endomicroscope and its application to visualize cervical remodeling during pregnancy*. Proceedings of the National Academy of Sciences of the United States of America, 2012. **109**(32): p. 12878-12883.
89. Ferhanoglu, O., et al., *A 5-mm piezo-scanning fiber device for high speed ultrafast laser microsurgery*. Biomedical Optics Express, 2014. **5**(7): p. 2023-2036.
90. *Cancer Facts and Figures* American Cancer Society, 2012.
91. Elder, J.B., C.Y. Liu, and M.L.J. Apuzzo, *Neurosurgery in the realm of 10-9, Part 2: Applications of Nanotechnology to neurosurgery-present and future*. Neurosurgery, 2008. **62**(2): p. 269-285.
92. Leary, S.P., C.Y. Liu, and M.L.J. Apuzzo, *Toward the emergence of nanoneurosurgery: Part III---Nanomedicine: Targeted nanotherapy, nanosurgery, and progress toward the realization of nanoneurosurgery*. Neurosurgery, 2006. **58**(6): p. 1009-1026.
93. Amini, A. and R.H. Schmidt, *Endoscopic third ventriculostomy in a series of 36 adult patients*. Neurosurg Focus, 2005. **19**(6): p. E9.
94. Williams, E.M., J.G. Galbraith, and C.C. Duncan, *Neuroendoscopic laser-assisted ventriculostomy of the third ventricle*. AORN Journal, 1995. **61**(2): p. 345-359.
95. Benninger, M.S., et al., *Vocal fold scarring: current concepts and management*. Otolaryngol Head Neck Surg, 1996. **115**(5): p. 474-82.
96. Woo, P., et al., *Diagnosis and treatment of persistent dysphonia after laryngeal surgery: a retrospective analysis of 62 patients*. Laryngoscope, 1994. **104**(9): p. 1084-91.
97. Wisweh, H., et al., *Optical coherence tomography monitoring of vocal fold femtosecond laser microsurgery - art. no. 663207*. Therapeutic Laser Applications and Laser-Tissue Interaction III, 2007. **6632**: p. 63207-63207.
98. Campagnola, P.J., et al., *Three-dimensional high-resolution second-harmonic generation imaging of endogenous structural proteins in biological tissues*. Biophys J, 2002. **82**(1 Pt 1): p. 493-508.
99. Zipfel, W.R., et al., *Live tissue intrinsic emission microscopy using multiphoton-excited native fluorescence and second harmonic generation*. Proceedings of the National Academy of Sciences of the United States of America, 2003. **100**(12): p. 7075-7080.
100. Dong, C.Y., K. Koenig, and P. So, *Characterizing point spread functions of two-photon fluorescence microscopy in turbid medium*. Journal of Biomedical Optics, 2003. **8**(3): p. 450-459.

101. Dunn, A.K., et al., *Influence of optical properties on two-photon fluorescence imaging in turbid samples*. Applied Optics, 2000. **39**(7): p. 1194-1201.
102. Durr, N.J., et al., *Maximum imaging depth of two-photon autofluorescence microscopy in epithelial tissues*. Journal of Biomedical Optics, 2011. **16**(2).
103. Hahn, M.S., et al., *Quantitative and comparative studies of the vocal fold extracellular matrix. I: Elastic fibers and hyaluronic acid*. Ann Otol Rhinol Laryngol, 2006. **115**(2): p. 156-64.
104. Hahn, M.S., et al., *Midmembranous vocal fold lamina propria proteoglycans across selected species*. Ann Otol Rhinol Laryngol, 2005. **114**(6): p. 451-62.
105. Hahn, M.S., et al., *Quantitative and comparative studies of the vocal fold extracellular matrix II: collagen*. Ann Otol Rhinol Laryngol, 2006. **115**(3): p. 225-32.
106. Adams, J., et al., *Acid/pepsin promotion of carcinogenesis in the hamster cheek pouch*. Arch Otolaryngol Head Neck Surg, 2000. **126**(3): p. 405-9.
107. Vairaktaris, E., et al., *The hamster model of sequential oral oncogenesis*. Oral Oncol, 2008. **44**(4): p. 315-24.
108. White, F.H., K. Gohari, and C.J. Smith, *Histological and ultrastructural morphology of 7,12 dimethylbenz(alpha)-anthracene carcinogenesis in hamster cheek pouch epithelium*. Diagn Histopathol, 1981. **4**(4): p. 307-33.
109. Driver, M., et al., *Laser-assisted low-dose retinoic acid in oral cancer chemoprevention*. Laryngoscope, 2005. **115**(2): p. 283-6.
110. Kingsbury, J.S., et al., *Photodynamic therapy for premalignant lesions in DMBA-treated hamsters: a preliminary study*. J Oral Maxillofac Surg, 1997. **55**(4): p. 376-81; discussion 381-2.
111. Meier, J.D., et al., *Treatment with 1-alpha,25-dihydroxyvitamin D3 (vitamin D3) to inhibit carcinogenesis in the hamster buccal pouch model*. Arch Otolaryngol Head Neck Surg, 2007. **133**(11): p. 1149-52.
112. Alipour, F. and S. Jaiswal, *Phonatory characteristics of excised pig, sheep, and cow larynges*. J Acoust Soc Am, 2008. **123**(6): p. 4572-81.
113. Garvey, W., *Modified elastic tissue-Masson trichrome stain*. Stain Technol, 1984. **59**(4): p. 213-6.
114. Chen, J.X., et al., *Spectroscopic characterization and microscopic imaging of extracted and in situ cutaneous collagen and elastic tissue components under two-photon excitation*. Skin Research and Technology, 2009. **15**(4): p. 418-426.
115. Koehler, M.J., et al., *In vivo assessment of human skin aging by multiphoton laser scanning tomography*. Optics Letters, 2006. **31**(19): p. 2879-2881.
116. Zoumi, A., A. Yeh, and B.J. Tromberg, *Imaging cells and extracellular matrix in vivo by using second-harmonic generation and two-photon excited fluorescence*. Proceedings of the National Academy of Sciences of the United States of America, 2002. **99**(17): p. 11014-11019.
117. Rousseau, B., et al., *Characterization of chronic vocal fold scarring in a rabbit model*. J Voice, 2004. **18**(1): p. 116-24.

118. Bashkatov, A.N., et al., *Optical properties of human skin, subcutaneous and mucous tissues in the wavelength range from 400 to 2000 nm*. Journal of Physics D-Applied Physics, 2005. **38**(15): p. 2543-2555.
119. Doornbos, R.M.P., et al., *The determination of in vivo human tissue optical properties and absolute chromophore concentrations using spatially resolved steady-state diffuse reflectance spectroscopy*. Physics in Medicine and Biology, 1999. **44**(4): p. 967-981.
120. Shen, N., *Photodisruption in biological tissues using femtosecond laser pulses*. In The Department of Physics, Harvard, Cambridge, Massachusetts, 2003: p. 125.
121. Tal, E., D. Oron, and Y. Silberberg, *Improved depth resolution in video-rate line-scanning multiphoton microscopy using temporal focusing*. Optics Letters, 2005. **30**(13): p. 1686-1688.
122. Zhu, G., et al., *Simultaneous spatial and temporal focusing of femtosecond pulses*. Opt Express, 2005. **13**(6): p. 2153-9.
123. Vitek, D.N., et al., *Temporally focused femtosecond laser pulses for low numerical aperture micromachining through optically transparent materials*. Optics Express, 2010. **18**(17): p. 18086-18094.
124. Wolinsky, H. and S. Glagov, *Structural Basis for the Static Mechanical Properties of the Aortic Media*. Circ Res, 1964. **14**: p. 400-13.
125. Thibeault, S.L., et al., *Histologic and rheologic characterization of vocal fold scarring*. J Voice, 2002. **16**(1): p. 96-104.
126. Roeder, B.A., et al., *Tensile mechanical properties of three-dimensional type I collagen extracellular matrices with varied microstructure*. J Biomech Eng, 2002. **124**(2): p. 214-22.
127. Doillon, C.J., et al., *Collagen fiber formation in repair tissue: development of strength and toughness*. Coll Relat Res, 1985. **5**(6): p. 481-92.
128. Martin, P., *Wound healing--aiming for perfect skin regeneration*. Science, 1997. **276**(5309): p. 75-81.
129. Walsh, J.T., Jr. and T.F. Deutsch, *Pulsed CO₂ laser ablation of tissue: effect of mechanical properties*. IEEE Trans Biomed Eng, 1989. **36**(12): p. 1195-201.
130. Woodson, G., *Developing a porcine model for study of vocal fold scar*. J Voice, 2012. **26**(6): p. 706-10.
131. Hoy, C.L., et al., *Clinical Ultrafast Laser Surgery: Recent Advances and Future Directions*. Ieee Journal of Selected Topics in Quantum Electronics, 2014. **20**(2).
132. He, G.S., et al., *Observation of stimulated emission by direct three-photon excitation*. Nature, 2002. **415**(6873): p. 767-70.
133. Hell, S.W., et al., *Three-photon excitation in fluorescence microscopy*. J Biomed Opt, 1996. **1**(1): p. 71-4.
134. Beaurepaire, E., M. Oheim, and J. Mertz, *Ultra-deep two-photon fluorescence excitation in turbid media*. Optics Communications, 2001. **188**(1): p. 25-29.
135. Koester, H.J., et al., *Ca²⁺ fluorescence imaging with pico- and femtosecond two-photon excitation: signal and photodamage*. Biophys J, 1999. **77**(4): p. 2226-36.

136. Konig, K., et al., *Cell damage by near-IR microbeams*. Nature, 1995. **377**(6544): p. 20-1.
137. Leray, A., et al., *Spatially distributed two-photon excitation fluorescence in scattering media: Experiments and time-resolved Monte Carlo simulations*. Optics Communications, 2007. **272**(1): p. 269-278.
138. Chen, Z., et al., *Extending the fundamental imaging-depth limit of multi-photon microscopy by imaging with photo-activatable fluorophores*. Opt Express, 2012. **20**(17): p. 18525-36.
139. Wei, L., Z. Chen, and W. Min, *Stimulated emission reduced fluorescence microscopy: a concept for extending the fundamental depth limit of two-photon fluorescence imaging*. Biomed Opt Express, 2012. **3**(6): p. 1465-75.
140. Kobat, D., et al., *Deep tissue multiphoton microscopy using longer wavelength excitation*. Optics Express, 2009. **17**(16): p. 13354-13364.
141. Horton, N.G., et al., *In vivo three-photon microscopy of subcortical structures within an intact mouse brain*. Nature Photonics, 2013. **7**(3): p. 205-209.
142. Campagnola, P.J. and L.M. Loew, *Second-harmonic imaging microscopy for visualizing biomolecular arrays in cells, tissues and organisms*. Nat Biotechnol, 2003. **21**(11): p. 1356-60.
143. Yelin, D. and Y. Silberberg, *Laser scanning third-harmonic-generation microscopy in biology*. Opt Express, 1999. **5**(8): p. 169-75.
144. Barad, Y., et al., *Nonlinear scanning laser microscopy by third harmonic generation*. Applied Physics Letters, 1997. **70**(8): p. 922-924.
145. Muller, M., et al., *3D microscopy of transparent objects using third-harmonic generation*. Journal of microscopy, 1998. **191**(3): p. 266-274.
146. Gualda, E.J., et al., *In vivo imaging of neurodegeneration in Caenorhabditis elegans by third harmonic generation microscopy*. J Microsc, 2008. **232**(2): p. 270-5.
147. Debarre, D., et al., *Imaging lipid bodies in cells and tissues using third-harmonic generation microscopy*. Nature Methods, 2006. **3**(1): p. 47-53.
148. Chu, S.W., et al., *In vivo developmental biology study using noninvasive multi-harmonic generation microscopy*. Opt Express, 2003. **11**(23): p. 3093-3099.
149. Sun, C.K., et al., *Higher harmonic generation microscopy for developmental biology*. J Struct Biol, 2004. **147**(1): p. 19-30.
150. Barzda, V., et al., *Visualization of mitochondria in cardiomyocytes by simultaneous harmonic generation and fluorescence microscopy*. Opt Express, 2005. **13**(20): p. 8263-76.
151. Sun, C.K., et al., *Multiharmonic-generation biopsy of skin*. Opt Lett, 2003. **28**(24): p. 2488-90.
152. Sun, C.K., et al., *In vivo and ex vivo imaging of intra-tissue elastic fibers using third-harmonic-generation microscopy*. Opt Express, 2007. **15**(18): p. 11167-11177.
153. Belisle, J.M., et al., *Sensitive detection of malaria infection by third harmonic generation imaging*. Biophys J, 2008. **94**(4): p. L26-8.

154. Farrar, M.J., et al., *In vivo imaging of myelin in the vertebrate central nervous system using third harmonic generation microscopy*. Biophys J, 2011. **100**(5): p. 1362-1371.
155. Olivier, N., et al., *Harmonic microscopy of isotropic and anisotropic microstructure of the human cornea*. Opt Express, 2010. **18**(5): p. 5028-40.
156. Tai, S.P., et al., *In vivo optical biopsy of hamster oral cavity with epi-third-harmonic-generation microscopy*. Opt Express, 2006. **14**(13): p. 6178-87.
157. Tai, S.P., et al., *Optical biopsy of fixed human skin with backward-collected optical harmonics signals*. Opt Express, 2005. **13**(20): p. 8231-42.
158. Rehberg, M., et al., *Label-free 3D visualization of cellular and tissue structures in intact muscle with second and third harmonic generation microscopy*. PLoS One, 2011. **6**(11): p. e28237.
159. Fermann, M.E. and I. Hartl, *Ultrafast fibre lasers*. Nature Photonics, 2013. **7**(11): p. 868-874.
160. Jauregui, C., J. Limpert, and A. Tunnermann, *High-power fibre lasers*. Nature Photonics, 2013. **7**(11): p. 861-867.
161. Nguyen, Q.T., P.S. Tsai, and D. Kleinfeld, *MPScope: a versatile software suite for multiphoton microscopy*. J Neurosci Methods, 2006. **156**(1-2): p. 351-9.
162. Jacques, S.L., *Optical properties of biological tissues: a review*. Phys Med Biol, 2013. **58**(11): p. R37-61.
163. Segelstein, D.J., *The complex refractive index of water*. Doctoral Dissertation, University of Missouri-Kansas City, 1981.
164. Warren, S.G., *Optical constants of ice from the ultraviolet to the microwave*. Applied Optics, 1984. **23**(8): p. 1206-1225.
165. Jaunich, M., et al., *Bio-heat transfer analysis during short pulse laser irradiation of tissues*. International Journal of Heat and Mass Transfer, 2008. **51**(23): p. 5511-5521.
166. Debarre, D., N. Olivier, and E. Beaufepaire, *Signal epidetection in third-harmonic generation microscopy of turbid media*. Opt Express, 2007. **15**(14): p. 8913-24.
167. Prahl, S.A., et al., *A Monte Carlo model of light propagation in tissue*. Dosimetry of laser radiation in medicine and biology, 1989. **5**: p. 102-111.
168. Rabiner, L.R., R.W. Schafer, and C.M. Rader, *The chirp z-transform algorithm*. Audio and Electroacoustics, 1969. **17**(2): p. 86-92.
169. Sandkuijl, D., et al., *Numerical second-and third-harmonic generation microscopy*. JOSA B, 2013. **30**(2): p. 382-395.
170. Mitra, K., et al., *Experimental-Evidence of Hyperbolic Heat-Conduction in Processed Meat*. Journal of Heat Transfer, 1995. **117**(3): p. 568-573.
171. Kim, K. and Z. Guo, *Ultrafast radiation heat transfer in laser tissue welding and soldering*. Numerical Heat Transfer, Part A: Applications, 2004. **46**(1): p. 23-40.
172. Kim, K. and Z. Guo, *Multi-time-scale heat transfer modeling of turbid tissues exposed to short-pulsed irradiations*. Comput Methods Programs Biomed, 2007. **86**(2): p. 112-23.

173. Dewey, W.C., et al., *Cellular responses to combinations of hyperthermia and radiation*. Radiology, 1977. **123**(2): p. 463-74.
174. Roti, J.L., *Cellular responses to hyperthermia (40-46 degrees C): cell killing and molecular events*. Int J Hyperthermia, 2008. **24**(1): p. 3-15.
175. Best, S.R. and C. Fakhry, *The prevalence, diagnosis, and management of voice disorders in a National Ambulatory Medical Care Survey (NAMCS) cohort*. Laryngoscope, 2011. **121**(1): p. 150-7.
176. Bhattacharyya, N., *The prevalence of voice problems among adults in the United States*. The Laryngoscope, 2014. **124**(10): p. 2359-2362.
177. Cohen, S.M., et al., *Prevalence and causes of dysphonia in a large treatment-seeking population*. Laryngoscope, 2012. **122**(2): p. 343-8.
178. Roy, N., et al., *Voice disorders in the general population: prevalence, risk factors, and occupational impact*. Laryngoscope, 2005. **115**(11): p. 1988-95.
179. Roy, N., et al., *Prevalence of voice disorders in teachers and the general population*. J Speech Lang Hear Res, 2004. **47**(2): p. 281-93.
180. Hirano, S., et al., *Histologic characterization of human scarred vocal folds*. J Voice, 2009. **23**(4): p. 399-407.
181. Tateya, T., et al., *Histologic characterization of rat vocal fold scarring*. Ann Otol Rhinol Laryngol, 2005. **114**(3): p. 183-91.
182. Tateya, T., et al., *Histological study of acute vocal fold injury in a rat model*. Ann Otol Rhinol Laryngol, 2006. **115**(4): p. 285-92.
183. Hansen, J.K. and S.L. Thibault, *Current understanding and review of the literature: vocal fold scarring*. J Voice, 2006. **20**(1): p. 110-20.
184. Kriesel, K.J., et al., *Treatment of vocal fold scarring: rheological and histological measures of homologous collagen matrix*. Ann Otol Rhinol Laryngol, 2002. **111**(10): p. 884-9.
185. Rousseau, B., et al., *Characterization of vocal fold scarring in a canine model*. Laryngoscope, 2003. **113**(4): p. 620-7.
186. Provenzano, P.P., et al., *Collagen reorganization at the tumor-stromal interface facilitates local invasion*. BMC Medicine, 2006. **4**(1): p. 38.
187. Robinson, P.S. and R.T. Tranquillo, *Planar Biaxial behaviour of fibrin-based tissue-engineered heart valve leaflets*. Tissue Engineering Part A, 2009. **15**(10): p. 2763-2772.
188. Miri, A.K., et al., *Nonlinear laser scanning microscopy of human vocal folds*. Laryngoscope, 2012. **122**(2): p. 356-63.
189. Ayres, C.E., et al., *Measuring fiber alignment in electrospun scaffolds: a user's guide to the 2D fast Fourier transform approach*. J Biomater Sci Polym Ed, 2008. **19**(5): p. 603-21.
190. Levitt, J.M., et al., *Diagnostic cellular organization features extracted from autofluorescence images*. Opt Lett, 2007. **32**(22): p. 3305-7.
191. Sander, E.A. and V.H. Barocas, *Comparison of 2D fiber network orientation measurement methods*. J Biomed Mater Res A, 2009. **88**(2): p. 322-31.

192. Sivaguru, M., et al., *Quantitative analysis of collagen fiber organization in injured tendons using Fourier transform-second harmonic generation imaging*. Opt Express, 2010. **18**(24): p. 23983-23993.
193. Bayan, C., et al., *Fully automated, quantitative, noninvasive assessment of collagen fiber content and organization in thick collagen gels*. J Appl Phys, 2009. **105**(10): p. 102042.
194. Bas, E. and D. Erdogmus, *Piecewise linear cylinder models for 3-dimensional axon segmentation in brainbow imagery*. In Biomedical Imaging: From Nano to Macro, 2010 IEEE International Symposium on., 2010: p. 1297-1300.
195. Mori, S. and P.C. van Zijl, *Fiber tracking: principles and strategies - a technical review*. NMR Biomed, 2002. **15**(7-8): p. 468-80.
196. Rodriguez, A., et al., *Three-dimensional neuron tracing by voxel scooping*. J Neurosci Methods, 2009. **184**(1): p. 169-75.
197. Quinn, K.P., et al., *An automated image processing method to quantify collagen fibre organization within cutaneous scar tissue*. Experimental dermatology, 2015. **24**(1): p. 78-80.
198. D'Amore, A., et al., *Characterization of the complete fiber network topology of planar fibrous tissues and scaffolds*. Biomaterials, 2010. **31**(20): p. 5345-54.
199. Otsu, N., *A threshold selection method from gray-level histograms*. Automatica, 1975. **11**(285-296): p. 23-27.
200. Quinn, K.P. and I. Georgakoudi, *Rapid quantification of pixel-wise fiber orientation data in micrographs*. J Biomed Opt, 2013. **18**(4): p. 046003.
201. Ehrlich, H.P., *Collagen considerations in scarring and regenerative repair*. Basic and Clinical Dermatology, 2000. **19**: p. 99-114.
202. Durr, N.J., et al., *Maximum imaging depth of two-photon autofluorescence microscopy in epithelial tissues*. J Biomed Opt, 2011. **16**(2): p. 026008.
203. Theer, P. and W. Denk, *On the fundamental imaging-depth limit in two-photon microscopy*. J Opt Soc Am A Opt Image Sci Vis, 2006. **23**(12): p. 3139-49.
204. Hirano, S., et al., *Fibronectin and adhesion molecules on canine scarred vocal folds*. Laryngoscope, 2003. **113**(6): p. 966-72.
205. Thibeault, S.L., D.M. Bless, and S.D. Gray, *Interstitial protein alterations in rabbit vocal fold with scar*. J Voice, 2003. **17**(3): p. 377-83.
206. Hirano, S., *Regeneration of the vocal fold*. In: Juichi Ito eds. Regenerative Medicine in Otolaryngology. Kyoto, Japan:Springer, 2015: p. 171-195.
207. Bless, D.M. and N.V. Welham, *Characterization of vocal fold scar formation, prophylaxis, and treatment using animal models*. Curr Opin Otolaryngol Head Neck Surg, 2010. **18**(6): p. 481.
208. Chhetri, D.K. and A.H. Mendelsohn, *Hyaluronic acid for the treatment of vocal fold scars*. Curr Opin Otolaryngol Head Neck Surg, 2010. **18**(6): p. 498-502.
209. Hansen, J.K., et al., *In vivo engineering of the vocal fold extracellular matrix with injectable hyaluronic acid hydrogels: early effects on tissue repair and biomechanics in a rabbit model*. Ann Otol Rhinol Laryngol, 2005. **114**(9): p. 662-70.

210. Jahan-Parwar, B., et al., *Hylan B gel restores structure and function to laser-ablated canine vocal folds*. Ann Otol Rhinol Laryngol, 2008. **117**(9): p. 703-7.
211. Kim, Y.M., et al., *Adipose-derived stem cell-containing hyaluronic acid/alginate hydrogel improves vocal fold wound healing*. Laryngoscope, 2014. **124**(3): p. E64-72.
212. Kishimoto, Y., et al., *Chronic vocal fold scar restoration with hepatocyte growth factor hydrogel*. Laryngoscope, 2010. **120**(1): p. 108-13.
213. Maytag, A.L., et al., *Use of the rabbit larynx in an excised larynx setup*. Journal of Voice, 2013. **27**(1): p. 24-28.
214. Peng, H., et al., *The use of laryngeal mucosa mesenchymal stem cells for the repair the vocal fold injury*. Biomaterials, 2013. **34**(36): p. 9026-9035.
215. Suehiro, A., et al., *Treatment of acute vocal fold scar with local injection of basic fibroblast growth factor: a canine study*. Acta Otolaryngol, 2010. **130**(7): p. 844-50.
216. Thibeault, S.L., et al., *In Vivo engineering of the vocal fold ECM with injectable HA hydrogels-late effects on tissue repair and biomechanics in a rabbit model*. J Voice, 2011. **25**(2): p. 249-53.
217. Chan, K.M., et al., *Functionalizable hydrogel microparticles of tunable size and stiffness for soft-tissue filler applications*. Acta Biomater, 2014. **10**(6): p. 2563-73.
218. Ohno, T., et al., *Drug delivery system of hepatocyte growth factor for the treatment of vocal fold scarring in a canine model*. Ann Otol Rhinol Laryngol, 2007. **116**(10): p. 762-9.
219. Finck, C.L., et al., *Implantation of esterified hyaluronic acid in microdissected Reinke's space after vocal fold microsurgery: short- and long-term results*. J Voice, 2010. **24**(5): p. 626-35.
220. Heris, H.K., M. Rahmat, and L. Mongeau, *Characterization of a hierarchical network of hyaluronic acid/gelatin composite for use as a smart injectable biomaterial*. Macromolecular bioscience, 2012. **12**(2): p. 202-210.
221. Hirano, S., et al., *Regenerative phonosurgical treatments for vocal fold scar and sulcus with basic fibroblast growth factor*. Laryngoscope, 2013. **123**(11): p. 2749-55.
222. Molteni, G., et al., *Auto-crosslinked hyaluronan gel injections in phonosurgery*. Otolaryngol Head Neck Surg, 2010. **142**(4): p. 547-53.
223. Kezirian, G.M. and K.G. Stonecipher, *Comparison of the IntraLase femtosecond laser and mechanical keratomes for laser in situ keratomileusis*. J Cataract Refract Surg, 2004. **30**(4): p. 804-11.
224. Palanker, D.V., et al., *Femtosecond laser-assisted cataract surgery with integrated optical coherence tomography*. Sci Transl Med, 2010. **2**(58): p. 58ra85.
225. Lee, C.M., et al., *Scanning fiber endoscopy with highly flexible, 1 mm catheterscopes for wide-field, full-color imaging*. Journal of biophotonics, 2010. **3**(5-6): p. 385-407.

226. Xi, J., et al., *Integrated multimodal endomicroscopy platform for simultaneous en face optical coherence and two-photon fluorescence imaging*. Opt Lett, 2012. **37**(3): p. 362-4.
227. Senturia, S.D., *Microsystem design* Springer Science and Business Media, 2007.
228. Cramers, D.A., et al., *Laser-Induced Breakdown Spectroscopy, Elemental Analysis*. John Wiley and Sons, Ltd., 2006.
229. Teich, M.C. and B. Saleh, *Fundamentals of photonics*. Wiley Interscience, 1991.
230. Stuart, B.C., et al., *Nanosecond-to-femtosecond laser-induced breakdown in dielectrics*. Phys Rev B Condens Matter, 1996. **53**(4): p. 1749-1761.
231. Ashkenasi, D., et al., *Surface damage threshold and structuring of dielectrics using femtosecond laser pulses: the role of incubation*. Applied Surface Science, 1999. **150**(1): p. 101-106.
232. House, R., J.R. Bettis, and A.H. Guenther, *Surface roughness and laser damage threshold*. Quantum Electronics, IEEE Journal of, 1977. **13**(5): p. 361-363.
233. Kean, P.N., K. Smith, and W. Sibbett, *Spectral and temporal investigation of self-phase modulation and stimulated Raman scattering in a single-mode optical fibre*. IEEE Proceedings J (Optoelectronics), 1987. **134**(3): p. 163-170.
234. Ouzounov, D.G., et al., *Generation of megawatt optical solitons in hollow-core photonic band-gap fibers*. Science, 2003. **301**(5640): p. 1702-4.
235. Seibel, E.J. and Q.Y. Smithwick, *Unique features of optical scanning, single fiber endoscopy*. Lasers Surg Med, 2002. **30**(3): p. 177-83.
236. Hoy, C.L., N.J. Durr, and A. Ben-Yakar, *Fast-updating and nonrepeating Lissajous image reconstruction method for capturing increased dynamic information*. Appl Opt, 2011. **50**(16): p. 2376-82.
237. Zhigilei, L.V. and B.J. Garrison, *Mechanisms of laser ablation from molecular dynamics simulations: dependence on the initial temperature and pulse duration*. Applied Physics A, 1999. **69**(1): p. S75-S80.
238. Frentzen, M., et al., *Osteotomy with 80- μ s CO₂ laser pulses—histological results*. Lasers in medical science, 2003. **18**(2): p. 119-124.
239. Chanthasopeephan, T., J.P. Desai, and A.C. Lau, *Measuring forces in liver cutting: new equipment and experimental results*. Ann Biomed Eng, 2003. **31**(11): p. 1372-82.
240. Amini-Nik, S., et al., *Ultrafast mid-IR laser scalpel: protein signals of the fundamental limits to minimally invasive surgery*. PLoS One, 2010. **5**(9).
241. Kaiser, M.L., et al., *Laryngeal epithelial thickness: a comparison between optical coherence tomography and histology*. Clinical Otolaryngology, 2009. **34**(5): p. 460-466.

Vita

Murat Yildirim received the B.Sc. and M.Sc. degrees in Mechanical Engineering from Middle East Technical University, Turkey, in 2006 and 2009, respectively. In 2010, he joined the FemtoLab under the supervision of Dr. Adela Ben-Yakar as a Graduate Researcher. He was the runner-up for the JenLab Young Investigator Award in SPIE Photonics West Conference for the best paper in 2013. He represented UT Austin in OSA Congressional Visit in 2014 and he was also a finalist in OSA Congressional Fellowship in 2015. Recently, he received Best Student Poster Award at OSI-11 International Conference on Optics of Surfaces and Interfaces held in Austin, Texas on June 28-July 3, 2015. His current research interests include nonlinear microscopy and developing miniaturized probes for tissue imaging and surgery with ultrafast lasers. He is a member of ASLMS, SPIE and OSA.

Permanent address: Ozsoy Sok. Nesem Apt. 3/10 Iccebeci Ankara 06590 Turkey

This dissertation was typed by the author.